



HAL
open science

Search for GRB neutrino emission according to the photospheric model with the ANTARES telescope

Matteo Sanguineti

► **To cite this version:**

Matteo Sanguineti. Search for GRB neutrino emission according to the photospheric model with the ANTARES telescope. High Energy Astrophysical Phenomena [astro-ph.HE]. Université Paris 7 Denis Diderot; Università degli studi di Genova - Italie, 2016. English. NNT: . tel-01478725

HAL Id: tel-01478725

<https://theses.hal.science/tel-01478725>

Submitted on 28 Feb 2017

HAL is a multi-disciplinary open access archive for the deposit and dissemination of scientific research documents, whether they are published or not. The documents may come from teaching and research institutions in France or abroad, or from public or private research centers.

L'archive ouverte pluridisciplinaire **HAL**, est destinée au dépôt et à la diffusion de documents scientifiques de niveau recherche, publiés ou non, émanant des établissements d'enseignement et de recherche français ou étrangers, des laboratoires publics ou privés.



Distributed under a Creative Commons Attribution 4.0 International License

Università degli Studi di Genova

Université Paris Diderot (Paris 7) - Sorbonne Paris Cité



Tesi di Dottorato in Fisica

Thèse de Doctorat en Physique de l'Univers

Search for GRB neutrino emission according to the photospheric model with the ANTARES telescope

Matteo Sanguineti

Supervisor:

Dott. Marco Anghinolfi

Prof. Antoine Kouchner

Jury members:

President: Prof. Giovanni Ridolfi

Rapporteur: Prof. Corinne Augier

Rapporteur: Prof. Pascal Gay

Prof. Marco Pallavicini

Contents

Introduction	4
1 The gamma ray bursts	7
1.1 Introduction	7
1.2 The fireball shock model	9
1.2.1 The internal shock	10
1.2.2 The external shock	11
1.3 The photospheric model	12
1.4 The expected neutrino flux	13
1.5 Summary	14
2 The ANTARES detector	17
2.1 The ANTARES Collaboration	17
2.2 Detector principle	18
2.3 Detector layout	20
2.3.1 The storeys	21
2.3.2 The optical module	25
2.3.3 The photomultiplier tube	26
2.4 ANTARES effective area	27
2.4.1 Muon effective area	27
2.4.2 Neutrino effective area	27
2.5 The ANTARES sea water properties	29
2.5.1 Light transmission, absorption and scattering	30
2.5.2 The scattering	31
2.5.3 The absorption	33
2.6 Background sources	33
2.6.1 The optical background	33
2.6.2 The atmospheric backgrounds	36
3 The data acquisition system	40
3.1 Introduction	40

3.2	The digitalization of the signals	40
3.3	The data filtering and storage	42
3.4	The standard data taking	43
3.5	The standard triggers	43
3.6	The GRBs alert network	44
3.7	The special data taking	46
3.8	The special directional trigger MX	48
4	The detector Monte Carlo simulation and the reconstruction algorithms	54
4.1	Introduction	54
4.2	The neutrino simulation	54
4.3	The atmospheric muon simulation	56
4.4	Cherenkov light simulation	57
4.5	Optical background simulation	58
4.6	ANTARES reconstruction algorithm	58
4.6.1	AaFit reconstruction algorithm	58
4.6.2	GridFit reconstruction algorithm	62
4.6.3	AaFit and GridFit performance comparison	66
5	The calibration of the detector	70
5.1	Introduction	70
5.2	The charge calibration	70
5.3	The time calibration	73
5.4	Study of the optical module performances with ^{40}K data	74
5.5	The position calibration	79
5.6	The Moon shadow measurement	81
5.6.1	Monte Carlo simulation of the Moon shadow	81
5.6.2	Detection of the Moon shadow	82
5.6.3	Angular resolution and absolute pointing	83
6	GRB 130427A analysis	89
6.1	Introduction	89
6.2	The signal estimation	90
6.3	The background estimation	92
6.3.1	The random background	92
6.3.2	The atmospheric muon background	93
6.4	Optimization of the quality parameter cut	97

<i>CONTENTS</i>	3
6.5 The average upper limit	101
6.6 Results of the analysis	105
6.7 GRB130505A analysis	108
Conclusions	110
Acknowledgments	112

Introduction

The measurement of cosmic neutrinos is a new and unique method to observe the Universe. Neutrinos are chargeless, weakly interacting particles that can cross dense matter or radiation fields without being absorbed for cosmological distance. Indeed, they are a complementary probe with respect to other messengers such as multi-wavelength light and charged cosmic rays allowing thus the observation of far Universe and the interior of the astrophysical sources.

The idea of neutrino detectors goes back to the 1950s, when Clyde Cowan and Frederick Reines first detected neutrinos from a nuclear reactor [1]. In the following years scientists detected neutrino from natural sources like the Sun and the Earth atmosphere. Neutrinos are really weakly interactive and a large amount of transparent matter is needed in order to detect them, so neutrino telescopes were built deep underwater or embedded in ice.

The first neutrino telescope was proposed in the seventies by the DUMAND project [3] (Deep Underwater Muon And Neutrino Detector). DUMAND was a proposed cubic-kilometre underwater neutrino telescope in the Pacific Ocean near the island of Hawaii. The project was cancelled in 1995, anyway DUMAND paved the way for successor projects. The first neutrino telescope was completed in 1997 in the ice of the South Pole, the Antarctic Muon And Neutrino Detector Array (AMANDA). Later it became a part of the actual IceCube observatory [4], completed in 2010, which consists of a cubic kilometre grid of sensors embedded below 1500 m of ice.

The ANTARES detector (Astronomy with a Neutrino Telescope and Abyss environmental RESearch), although much smaller than IceCube in size, is the largest neutrino telescope currently in operation in the Northern Hemisphere and the first operating in sea water. The main goal of the ANTARES telescope is the detection of high energy cosmic neutrinos and in particular the identification of point-like sources. Supernova remnants, starburst galaxies, gamma ray bursts (GRBs) and active galactic nuclei are promising candidate sources of cosmic neutrinos.

In particular GRBs are one of the most interesting celestial objects, they represent the

most powerful outburst of energy in the Universe since the Big Bang itself. Gamma ray bursts are intense flashes of gamma rays, their duration can vary from a fraction of a second up to a few minutes.

A flux of neutrino is also expected in correspondence of GRBs. The goal of this thesis is the detection of neutrino events associable with gamma ray bursts using the data collected by the ANTARES telescope.

In Ch. 1 the different gamma ray burst models are presented focusing in particular on the neutrino flux predicted by the diverse emission mechanisms. In this thesis I will focus on the photospheric GRB model. This scenario has been strongly supported in the last years because it explains some features of the GRB spectrum that are not expected by the other models. The photospheric model predicts a neutrino flux in a completely different energetic range with respect to the other models, the flux is shifted towards lower energies by some orders of magnitude. The overall expected neutrino flux is also larger, this increase is especially relevant for very bright GRBs.

In this thesis the research of a neutrino flux from the most promising gamma ray burst (GRB 130427A) is performed on a special data sample recorded by the ANTARES detector in correspondence of the burst. The ANTARES telescope is described in Ch. 2 and its data acquisition system is presented in Ch. 3 focusing on the characteristics of the special data sample used in this analysis (Sec. 3.7) and on a dedicated directional trigger algorithm (Sec. 3.8). The use of the special data sample and the directional trigger enhance the ANTARES sensibility in the energetic range where most of the neutrino flux is expected according to photospheric model.

In Ch. 4 the detector Monte Carlo simulation and the reconstruction algorithms are presented. In this thesis a special reconstruction algorithm (Sec. 4.6.2) optimized at low energies is used in order to further improve the ANTARES sensibility between 50 GeV and 10 TeV, the energetic range of the photospheric model.

The calibration of the detector is described in Ch. 5 focusing on two calibration measurements I have performed for the ANTARES collaboration: a study of the detector performances in 2013 (Sec. 5.4) and the measurement of the cosmic ray Moon shadow (Sec. 5.6). The latter is a unique method to test the pointing performance of the telescope with a calibration celestial object.

The research of a neutrino flux in correspondence of GRB130427A is presented in Ch. 6. The estimation of the signal and the background of the measurement is described in Sec. 6.2 and Sec. 6.3, whereas the analysis optimization is presented in Sec. 6.4. The final results of the thesis are discussed in Sec. 6.5 and Sec. 6.6 where the upper limit on the neutrino flux according to the photospheric model is presented and it is compared with the results

from other analysis where different GRB model were assumed.

Chapter 1

The gamma ray bursts

1.1 Introduction

Gamma ray burst (GRB) are one of the most energetic phenomena of the Universe: one of the most energetic GRB, detected in 2013, showed a global energy of 10^{54} erg. During the Cold War military satellites developed for the identification of nuclear tests detected the first Gamma Ray Bursts. These phenomena became public only several years later with the publication of Vela satellites [5], later confirmed by the Soviet Konus satellite [6]. The GRBs remained a mystery for many years because the flashes were extremely short in time and the emission mostly at gamma-ray energies.

A milestone in the GRB detection is the launch of the Compton Gamma-Ray Observatory, in particular the Burst and Transient Experiment (BATSE) which detected over 2700 bursts. BATSE showed that GRBs are distributed isotropically in the sky without any dipole or quadrupole moments, supporting the cosmological origin of these phenomena [7]. The experiment measured also the energy spectrum of GRBs [8]

$$N(\varepsilon) \propto \varepsilon^{-\alpha} \tag{1.1}$$

where

- $\alpha \sim 1$ at low energies
- $\alpha \sim 2 - 3$ above 0.1 MeV

This relationship is observed up to energies of several GeV. The duration of Gamma ray burst is variable, the time range being 10^{-3} to 10^3 s. Also the time dependence presents different features in GRBs, some bursts show a fast rise with quasi-exponential relaxing

time, other present peaks or substructures sometimes down to milliseconds [9]. An example of a light curve is shown in Fig 1.1 [10]. There is also an anti-correlation between spectral

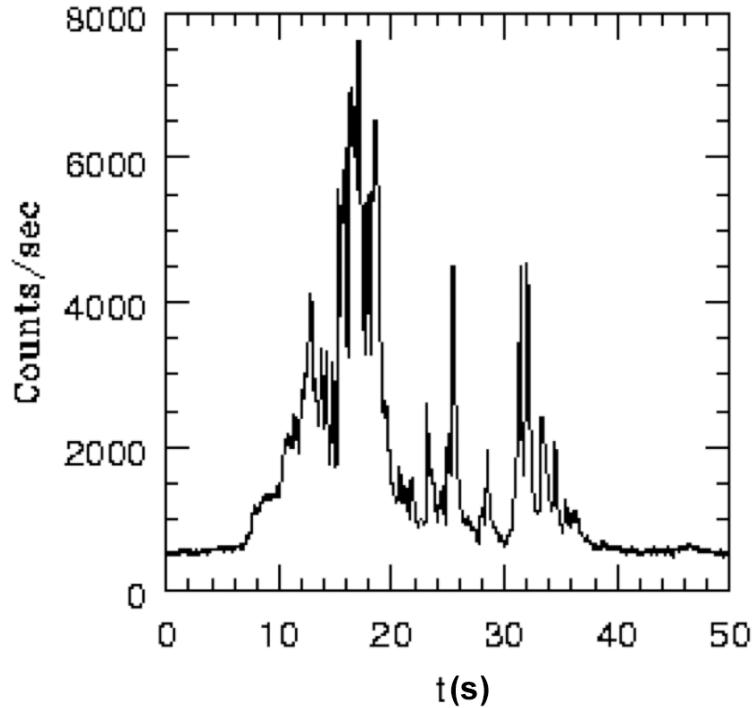


Figure 1.1: Typical GRB light curve observed with BATSE, showing photon count rate (0.05-0.5 MeV) versus time (s). No γ -rays are detected either before or after the burst trigger.

hardness and duration: the shorter the duration, the harder the spectrum. The space distribution of the GRBs is isotropic, this is a hint of the extra-galactic origin of these phenomena. In 1997 the satellite Beppo-SAX measured for the first time the X-ray emission of a GRB, the so-called "afterglow" as expected on theoretical grounds [11]. Later the afterglow of GRBs has been detected up to wavelengths of the visible light, but also the redshift distances has been measured with the identifications of the host galaxies confirming the extra-galactic origin of gamma ray bursts [12].

In the next chapters the main GRB emission models will be described. In particular I will focus on two competitive models: the fireball model and the photospheric model. Both models assume that the gamma ray emission is due to a relativistic jet of particle ejected by an inner engine, but the location of the interaction is different. In the case of the fireball

model the gamma rays are produced by the interaction of different shock waves inside the jet (internal shock) and by the interaction of jet with the interstellar medium (external shock). On the other hand in the photospheric scenario the interaction takes place in the initial part of the expansion of the jet, when it is still opaque to photons. In the next two sections more details about the two models are provided.

1.2 The fireball shock model

It is important to stress that the GRB fireball shock scenario, either internal or external, is quite generic: it is largely independent from the nature of the inner engine. Anyway we can make some assumption about the progenitor of the gamma ray bursts.

The inner engine needs to be able to push material out very near to the speed of light. It is a highly compact source, and it is the highly compact nature of this object that leads to the idea that the core of the inner engine of a GRB is either a neutron star or a black hole (as they're the two most compact sources that we're currently aware of). The workings of this inner engine will alter depending on whether it is a long or short GRB being observed. A short GRB could be associated with a merger of neutron stars or a merger of a neutron star with a black hole. On the other hand it has been suggested that a long GRB could be associated with a hypernova [13].

The expected energy of a GRB is around 10^{54} erg, so a such localized and brief phenomena implies the formation of an e^\pm, γ fireball that expands relativistically [14]. The spectral energy is mostly observed above 0.5 MeV, this would be impossible with a non-relativistic jet. In fact the photon energy would be rapidly lowered by the interaction $\gamma\gamma \rightarrow e^\pm$ before the photon can escape from the fireball. The relativistic expansion explains the observed photons at really high energies ($\epsilon_\gamma \gg 0.5$ MeV) [15], avoiding the degradation of the photon energy just below to 0.511 MeV.

Photons with ϵ_γ above 10 GeV can escape the annihilation against target photons with $\epsilon_{t\gamma}$ around 1 MeV, if the bulk Lorentz factor, defined as [16]

$$\Gamma = \frac{1}{\sqrt{1 - \beta^2}}, \quad (1.2)$$

where β is v/c , satisfies

$$\Gamma \geq 10^2 \sqrt{\frac{\epsilon_\gamma}{10 \text{ GeV}}} \sqrt{\frac{\epsilon_{t\gamma}}{1 \text{ MeV}}} \quad (1.3)$$

A relativistic outflow, associated with an initial energy E_0 imparted to a mass $M_0 \ll E_0/c^2$ starting out from a radius r_0 , leads to an expansion because it converts its internal energy into bulk kinetic energy [17]. At the beginning of the expansion the Lorentz factor is approximately

$$\Gamma \approx 10^2 \frac{r}{r_0} \propto r \quad (1.4)$$

The bulk Lorentz factor increases during the expansion, but it can not exceed the initial value of random internal energy per particle E_0/M_0c^2 . The bulk Lorentz factor only grows up to this value, which is achieved at a radius $r/r_0 \sim E_0/M_0c^2$.

- $\Gamma \sim \frac{r}{r_0}$ for $r < r_s$
- $\Gamma \sim \frac{E_0}{M_0c^2}$ for $r > r_s$

where r_s is the saturation radius beyond which the Lorentz factor remains constant [18]. However this process of fireball expansion leads to a conversion of internal energy into kinetic energy of baryons, rather than into photon luminosity. In fact the expected spectrum would be a black-body, but this prediction is clearly in contrast with the experimental measure of a broken power law spectrum.

A natural way to achieve a non-thermal spectrum in an energetically efficient manner is by having the kinetic energy of the flow re-converted into random energy via shocks, after the flow has become optically thin. This is based on the fact that shocks are likely to occur in such jets and if these occur after the fireball has become optically thin, these shocks would reconvert the kinetic energy of the baryons into nonthermal particle and photon energy [19][20]. These shocks can be expected to accelerate particles via the Fermi process to ultra-relativistic energies and the relativistic electron component can produce non-thermal radiation via the synchrotron and inverse Compton (IC) processes. A shock is essentially unavoidable as the fireball runs into the external medium, producing a blast wave. The external medium may be the interstellar medium (ISM), or the pre-ejected stellar wind from the progenitor before the collapse.

The fireball shock model predicts two different processes: the internal shocks and the external shocks.

1.2.1 The internal shock

The internal shocks are the mechanism for the production of the observed highly energetic gamma-rays. Moments after the initial GRB event, shock waves emanate from the inner

engine at relativistic speeds (99.995% of the speed of light, at a Lorentz factor of 100). Different shock waves will be traveling at different relativistic speeds, and it is the interaction between these different shock fronts that causes the energetic gamma-ray emissions. Initially, the fireball is optically thick but as it expands and cools it becomes optically thin, allowing the gamma-ray photons to escape. The central engine outflow can be modelled as a wind of duration t_w with an average lab-frame luminosity $L_0 = E_0/t_w$, average mass outflow \dot{M}_0 and a mean saturation Lorentz factor L_0/\dot{M}_0c^2 . Variations of the Lorentz factor occurring over a time scale $t_{var} \ll t_w$ lead to internal shocks at radii r_{is} above the photosphere r_{phot} .

This model assumes that the saturation radius r_s is smaller than the radius of the photosphere r_{phot} , so the most of the energy comes out in the shock, as opposed to the photosphere as expected in the photospheric model that will be described later.

The internal shock models can predict an arbitrarily complicated light curve, in fact it can reproduce some of the most complicated light curves [21]. The gamma-ray emission of GRB from internal shocks radiating via a synchrotron and/or inverse Compton mechanism reproduces the general features of the gamma-ray observation, but there are still some features that cannot be explained with these models. When internal shocks occur, these are generally expected to be followed by an external shock [22] (see Sec. 1.2.2) The GRB external shocks, similarly to what is observed in supernova remnants, consist of a forward shock or blast wave moving into the external medium ahead of the ejecta, and a reverse shock moving back into the ejecta. In the next subsection the external shock phenomena is described.

1.2.2 The external shock

The external shock waves are used to explain the afterglow detected by BeppoSAX in 1997, as the internal shock waves are not able to explain the duration of the afterglow nor the wavelengths that are detected (which range from soft x-ray through to radio).

The name "external shock" is a bit misleading, actually it is the same wave of the "internal shock", but at a later stage of propagation. As the shock waves continue out they will eventually interact with the Interstellar Medium (ISM) or the pre-ejected stellar wind from the progenitor before the collapse, the thermal interaction is responsible of the afterglow emission. The shock wave has cooled down, but it has still a lot of energy that can be deposited into the ISM, this is why the afterglow emission covers all parts of the energy spectrum and the emissions lasts in a longer time with respect to the prompt emission.

The external shock occurs at a larger distance from the central engine than the internal shocks radii r_{is} , at these point the initial bulk Lorentz factor has decreased to approxi-

mately half its original value, as the fireball ejecta is decelerated by external matter. GRBs typically occur in high mass system with very few stellar lives and may still be inside of a molecular cloud. Molecular clouds are very optically thick environments so the reason we are not able to detect the afterglow in about 50% of the time could just be reddening, absorption, or scattering of the light.

1.3 The photospheric model

Like in the fireball model the presence of jet-like relativistic outflow is assumed. The jet initially accelerates with a bulk Lorentz factor Γ , averaged over the jet cross section, that increases according to the power law

$$\Gamma \sim \left(\frac{r}{r_0}\right)^\mu \quad (1.5)$$

This law is true up to the saturation radius r_s , in other word the distance at which the bulk Lorentz factor Γ is equal to the initial value of random internal energy per particle E_0/M_0c^2 . The μ exponent is assumed to be $1/3 \leq \mu \leq 1$, where $\mu=1/3$ corresponds to a magnetically dominated outflow and $\mu=1$ corresponds to a baryonically dominated outflow [23].

The saturation radius dependence can be calculated in the two extreme hypotheses

- $r_s \sim \Gamma^3 r_0$ for $\mu = \frac{1}{3}$
- $r_s \sim \Gamma r_0$ for $\mu = 1$

The photospheric model predicts the conversion of a fraction of the bulk kinetic energy into radiation energy through dissipation mechanism in the neighbourhood of the photosphere. The photosphere occurs in the acceleration phase ($r < r_s$) if the outflow is magnetically dominated, on the other hand in the baryonic case the photosphere occurs in the coasting phase ($r > r_s$).

In the baryonic case, two different mechanisms can lead to dissipation: the dissipation of magnetohydrodynamics (MHD) turbulence [24] or semi-relativistic shocks [24] with Lorentz factor $\Gamma \sim 1$. These shock waves have different kinematic origins but similar physical properties as in the internal shock model, with a mechanical dissipation efficiency ϵ_d .

In the dissipation region a fraction ϵ_d of E_0 is assumed to be dispersed. This energy is converted into proton internal energy and random magnetic fields, which leads to relativistic protons and relativistic electrons. Calculations and simulations of such baryonic

and magnetic dissipative photospheres, as well as internal shocks, generally result in an escaping photon spectrum similar to the observed characteristic “Band” spectrum [25], parameterized as

$$\frac{dN_\gamma}{dE} \propto \left(\frac{E}{E_{br}}\right)^{x_{ph}} \quad (1.6)$$

where a burst with $z=2$ redshift shows E_{br} around 300 keV and

- $x_{ph} = -1$ for $E > E_{br}$
- $x_{ph} = -2$ for $E < E_{br}$

The spectral shape is the product of the modification of a thermal spectrum by the dissipation in the photosphere. In the next section the expected neutrino flux in the case of photospheric scenario is presented.

1.4 The expected neutrino flux

In the baryonic photosphere scenario protons and electrons are assumed to be accelerated through a Fermi-first order acceleration mechanism in the surrounding magnetic fields. A similar process is also expected in the magnetic photosphere scenario. The particles can reach the energies typical of the Fermi mechanism bouncing back and forth in the converging flow between the layers [26].

Neutrinos are mainly produced through charged pion and kaon decays; these charged mesons come from $p\gamma$ and pp interactions. For energies below 1 GeV the cross section is dominated by resonances while at higher energies multi-pion production prevails. In the single-pion resonance channel, π^+ and π^0 are created at approximately the same rate, while in the multi-pion channel π^+ , π^- and π^0 are produced almost equally. In the case of pp interactions, the target protons are the fraction of protons that are not accelerated [26].

The number of produced kaons is small, they corresponds to 1 - 10% of the pions from $p\gamma$ or pp interactions. Neutrinos from kaon decay are relevant at high energies; in fact kaons are less affected by radiative cooling than pions. The pion decay is fully understood and neutrinos are produced mainly from this channel:

$$\pi^- \rightarrow \mu^- + \bar{\nu}_\mu \rightarrow e^- + \bar{\nu}_e + \nu_\mu + \bar{\nu}_\mu$$

and the charge conjugate particles for the π^+ .

High-energy pions lose a significant fraction of their energy through synchrotron radiation. For muons with their longer mean lifetime and smaller mass, synchrotron cooling is more severe than that of charged pions.

As previously mentioned the photospheric model can predict two different scenarios: the baryonic dominated jets or magnetic field dominated jets. These two possibilities lead to different macroscopic acceleration rates, different proper densities in the jet rest-frame, and imply a different role for magnetic dissipation in the process of particle acceleration. In Fig. 1.2 and Fig. 1.3 two different estimations of the neutrino flux from a GRB according to photospheric model are shown.

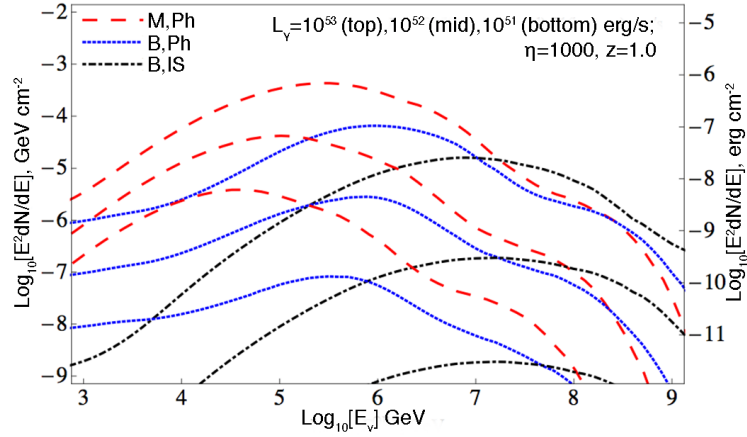


Figure 1.2: Neutrino fluence from a single GRB assuming different dissipation models. Red, dashed: magnetic photosphere; blue, dotted: baryonic photosphere; Dot-dash: baryonic internal shock [26]. Model parameters: luminosity $L_\gamma=10^{53}$ erg/s (top curve), 10^{52} erg/s (mid curve), 10^{51} erg/s (bottom curve), redshift $z=1$.

The photospheric model (both baryonic dominated and magnetic dominated) predicts a neutrino flux at lower energies with respect to the internal shock model. The overall flux expectation is also higher with respect to the internal shock scenario. These features are promising for the ANTARES detector and a dedicated analysis is proposed in order to investigate this neutrino emission model.

1.5 Summary

The photospheric model which will be considered in this work has been strongly supported in the last years because it explains some features of the GRB spectrum that are not

expected in the fireball scenario (see Sec. 1.2).

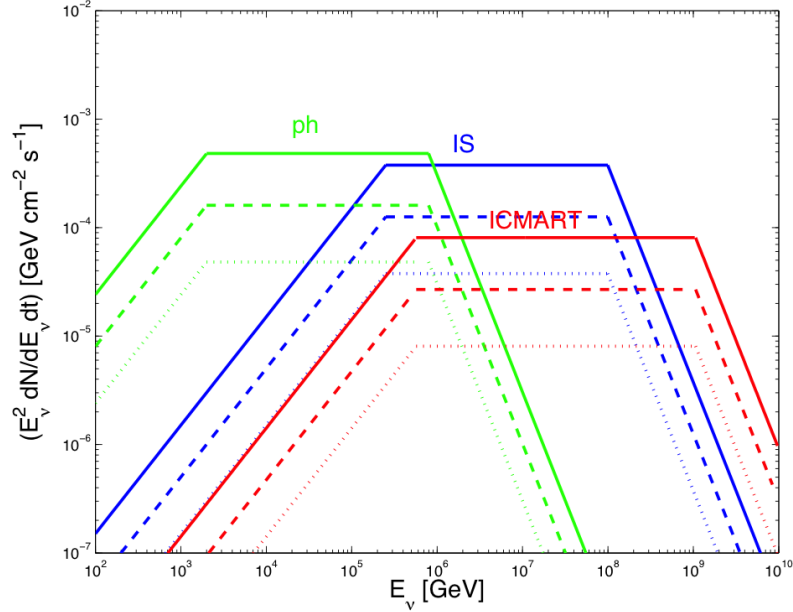


Figure 1.3: Neutrino flux from a single GRB assuming different dissipation models: "ph" (green): dissipative photosphere model; "IS" (blue): internal shock model; "ICMART" (red): internal-collision-induced magnetic reconnection and turbulence model. Model parameters: normalized luminosity $L_{\gamma,52} = 10^{52}$ erg, variability time scale observed in the GRB light curve $\delta t=0.1$ s, redshift $z=1$, Lorentz factor $\gamma = 250$ [27]. Three values of the ratio between photon luminosity and non-thermal proton luminosity are adopted: 0.1 (solid), 0.3 (dashed), and 1 (dotted).

The Amati correlation is the observed relation between the average peak energy and the overall radiated energy. Numerical simulations showed that the Amati correlation can be naturally reproduced by photospheric emission [28]. The photospheric model predicts also the observed correlations between the overall radiated energy and the jet Lorentz factor. These predictions that are verified experimentally are a strong support on the photospheric scenario.

The photospheric model also predicts a neutrino flux in an interesting energetic region for the ANTARES detector. The energetic range is completely different with respect to the fireball scenario, it is shifted towards lower energies by some orders of magnitude. The expected neutrino flux is also larger with respect to the fireball scenario, this increase is especially relevant for very bright GRBs, as shown in Sec. 6.2. For these reasons a special analysis is proposed in order to improve the ANTARES sensitivity in the region between

50 GeV and 10 TeV where most of the neutrino flux is expected according to photospheric scenario (see Chapter 3).

Chapter 2

The ANTARES detector

2.1 The ANTARES Collaboration

ANTARES (Astronomy with a Neutrino Telescope and Abyss environmental RESearch) is the largest water-Cherenkov neutrino detector of the Northern Hemisphere, the first that operates in the sea water. It is installed 40 km offshore from Toulon, France ($42^{\circ}48'$ N, $6^{\circ}10'$ E) at a depth of 2475 m. The ANTARES collaboration includes 37 institutes in 8 countries (France, Germany, Italy, the Netherlands, Romania, Russia, Spain and Morocco) (Fig 2.1).



Figure 2.1: Location of institute members of the ANTARES collaboration.

It consists of a 3D array of 885 detection units, called optical module (OM), arranged in

12 detection lines to instrument a 0.1 km^3 volume (Fig 2.5). The telescope is designed for the detection of the Cherenkov light. The radiation is induced by relativistic leptons produced in the interaction of high-energy neutrinos with the detector surroundings. Neutrinos are not deflected by magnetic fields in their travel towards the Earth, so it is possible to trace the muon back to the neutrino origin. This justifies the name telescope applied to this kind of detector. Neutrinos are a unique probe to investigate the inner of the astrophysical objects. Photons and protons can not cross dense medium and moreover protons are deflected by magnetic fields, so it is not possible to trace back their origin. The first line of ANTARES was deployed in February 2006 and measurements of the atmospheric muon flux were performed shortly after [29]. The detector was completed between March 2006 and May 2008.

2.2 Detector principle

The idea of a Cherenkov neutrino telescope based on the detection of the secondary particles produced in neutrino interactions was proposed in the 1960s by Markov [30]. He suggested a matrix of light detectors inside a transparent medium, like deep water or ice, because:

- a large volume of water or ice can be found easily and it provides a large target volume for neutrino interaction.
- the deepness provides a good shielding against the secondary particles produced by CRs.
- water and ice allow the transmission of Cherenkov light.

The Cherenkov light is emitted after the passage of relativistic particles produced by the neutrino interaction. The interaction with matter is dominated by the inelastic scattering nucleons for neutrinos with energy above the GeV scale. The interaction can be due to the exchange of the bosons W^\pm via the so-called charged current (CC) weak interaction:

$$\nu_l + N \rightarrow l + X$$

or to the exchange of the neutral boson Z^0 via the so-called neutral current (NC) weak interaction:

$$\nu_l + N \rightarrow \nu_l + X$$

where l is a lepton and X represents all the particles produced by the neutrino interaction. Neutrinos can be detected when the particles released by neutrino interactions with

nucleons induce Cherenkov radiation when crossing a suitable optical medium with speed greater than the speed of light in that medium. Charged relativistic particles induce a polarization to the molecules along their trajectory. When the disruption has passed, the medium electrons restore themselves to equilibrium emitting a coherent radiation. The photons are seen in the rest frame as a cone (see Fig 2.2) with a characteristic angle θ_C given by

$$\cos\theta_C = \frac{c}{\beta n} = \frac{1}{\beta n} \quad (2.1)$$

where β is defined as $\frac{v}{c}$ and n is the refractive index of the medium.

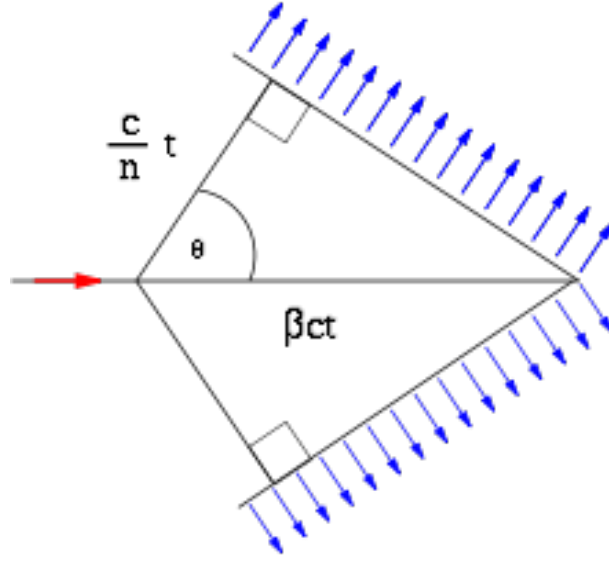


Figure 2.2: Schematic view of the production of Cherenkov radiation by a relativistic charged particle.

In the case of ultrarelativistic particles ($\beta \sim 1$) in sea water ($n=1.364$) the Cherenkov angle is around 43° . The number of Cherenkov photons N_γ emitted per unit of wavelength interval $d\lambda$ and unit of travelled distance dx can be estimated according to

$$\frac{d^2N}{dx d\lambda} = 2\pi\alpha \frac{1}{\lambda^2} \left(1 - \frac{1}{\beta^2 n^2}\right) \quad (2.2)$$

where λ is the wavelength of the Cherenkov light. In the typical wavelength range in which the PhotoMultiplier Tubes (PMTs) have their maximum efficiency (300-600 nm) the number of emitted Cherenkov photons is around $3.5 \cdot 10^4$ per meter.

The experimental signal consists in measuring the intensity and the arrival time of the Cherenkov photons on a three-dimensional array of PMTs as described in the next section. From that some information about the properties of the neutrino, like its direction and energy can be derived. The Cherenkov light emission is different for each neutrino flavour. In the case of neutrino detection due to the CC ν_μ interactions, the produced muon is the charged lepton with the longest range and it can be detected also if it is created outside the instrumented volume and the detected event will be "track-like". The remaining CC interactions and the NC ν_μ interaction are more difficult to detect due to the shorter range of the consequent leptons. Electron produces an electromagnetic shower which propagates for few meters while τ -lepton travels some distance (depending on its energy) before it decays and produces a second shower, so those events are called "shower-like". The Cherenkov light emitted by the charged particles in the shower can be detected only if the interaction occurs inside or close to the instrumented volume of the detector.

In the case of "shower-like" events, the muon created in a muon neutrino interaction retains almost the same direction of the neutrino. The angle between the incident neutrino and the outgoing muon $\Phi_{\nu-\mu}$ has an approximated upper limit of

$$\Phi_{\nu-\mu} \leq \frac{1.5^\circ}{\sqrt{E_\nu(\text{TeV})}} \quad (2.3)$$

where E_ν is the neutrino energy.

Fig 2.3 shows the error on angle determination obtained after several quality criteria (see Sec. 4.6) from muon neutrino interactions as a function of the simulated neutrino energy. The bottom curve shows the angle difference between the reconstructed muon and the simulated one. The mismatch is always below 0.5 degrees. The top curve shows the angular error between the reconstructed muon and the simulated neutrino. Below 1 TeV the error is dominated by the kinematics, above 1 TeV the muon is emitted closer to the direction of the parent neutrino.

The deviation due to the multiple scattering, to which a muon traveling through water or ice is subjected, at the energies and distances considered is smaller than the one determined by the kinematics.

2.3 Detector layout

The detector consists of an array of 12 independent and flexible lines made of mechanically resistant electro-optical cables separated by a distance of 74 m. Each line is equipped with

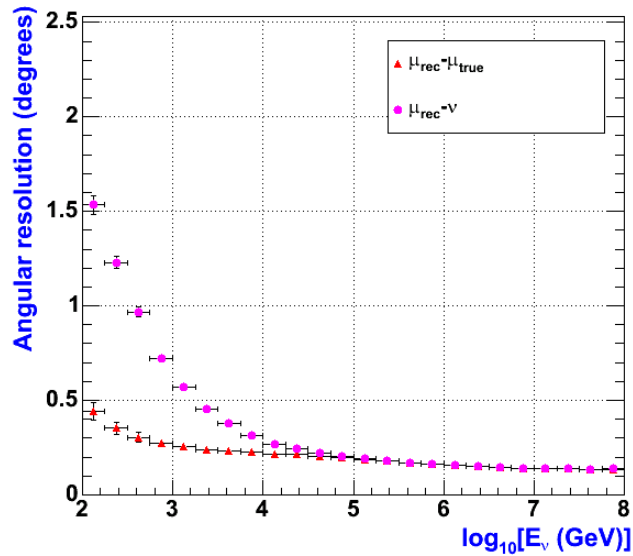


Figure 2.3: Median error on angle determination obtained after several quality criteria from muon neutrino interactions as a function of the simulated neutrino energy: angle difference between the reconstructed muon and the simulated one (bottom), angular error between the reconstructed muon and the simulated neutrino (top).

25 storeys (Sec. 2.3.1) and the 3 PMTs housed in each storey detect the light produced by muons traversing the instrumented volume. The position of the anchor of the 12 ANTARES lines is shown in Fig 2.4 and a schematic view of the detector is shown in Fig 2.5.

The detector is connected to shore by the means of the Main Electro Optical Cable (MEOC), which feeds and transfers data from the Junction Box (JB). The JB is a pressure resistant box where the 12 cables of the lines are interlinked with the MEOC. It contains also a transformer to decrease the 4kV AC voltage from shore down to 375 V AC and the power system of slow control electronics. At the bottom of each line the String Control Module (SCM) collects the data stream from the detection units of the line and transfer the data to the Junction Box.

The main detection components of the telescope will be described in the next paragraphs.

2.3.1 The storeys

In each line the optical modules are arranged in triplets called storeys (Fig 2.6).

The arrangement of the OMs in space was optimised according to Monte Carlo simulations in order to have the best neutrino detection efficiency. The optical modules are oriented downwards with an angle of 45° below the equator. This orientation provides high efficiency

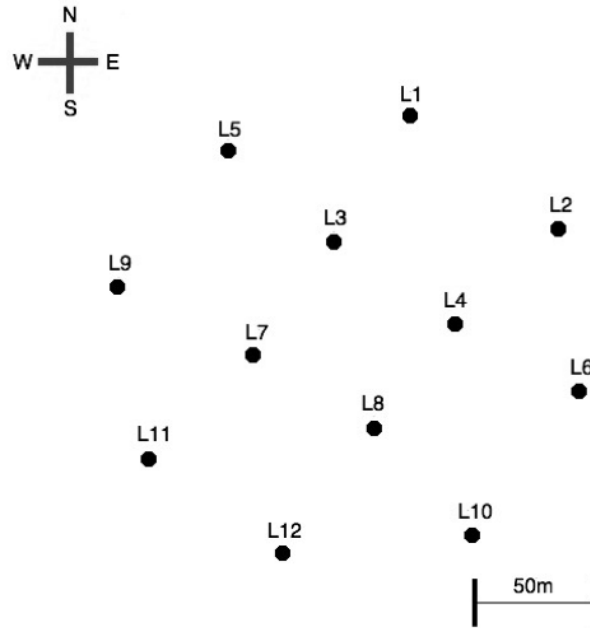


Figure 2.4: Positions of the anchors of the ANTARES lines on the seabed.

for tracks between upward vertical and horizontal directions, and minimizes the effects due to the biofouling. When a structure is immersed in seawater, it is covered by an unavoidable thin layer of micro-organism, this process, called biofouling, reduce the detection efficiency of the optical modules.

The distance between storeys on the same line is 14.5 m, whereas the distance between the lines is around 60 m. The storey includes also an electronic container called Local Control Module (LCM).

The standard components of a LCM comprise:

- The Local Power Box (LPB), which provides the 48 V voltage for the optical modules and some low voltage for electronics. The voltage can be set from shore and it is monitored together with the temperature and the current consumption. It is fed by a 400 DC voltage.
- The ARS (Analog Ring Sampling) board, which houses the front-end electronics of the optical module and digitizes the time and the charge of the PMT signals. This front-end electronics consists of a custom-built Analogue Ring Sampler chip.
- The DAQ/SC (Data Acquisition/Slow Control), which manages the signals from the

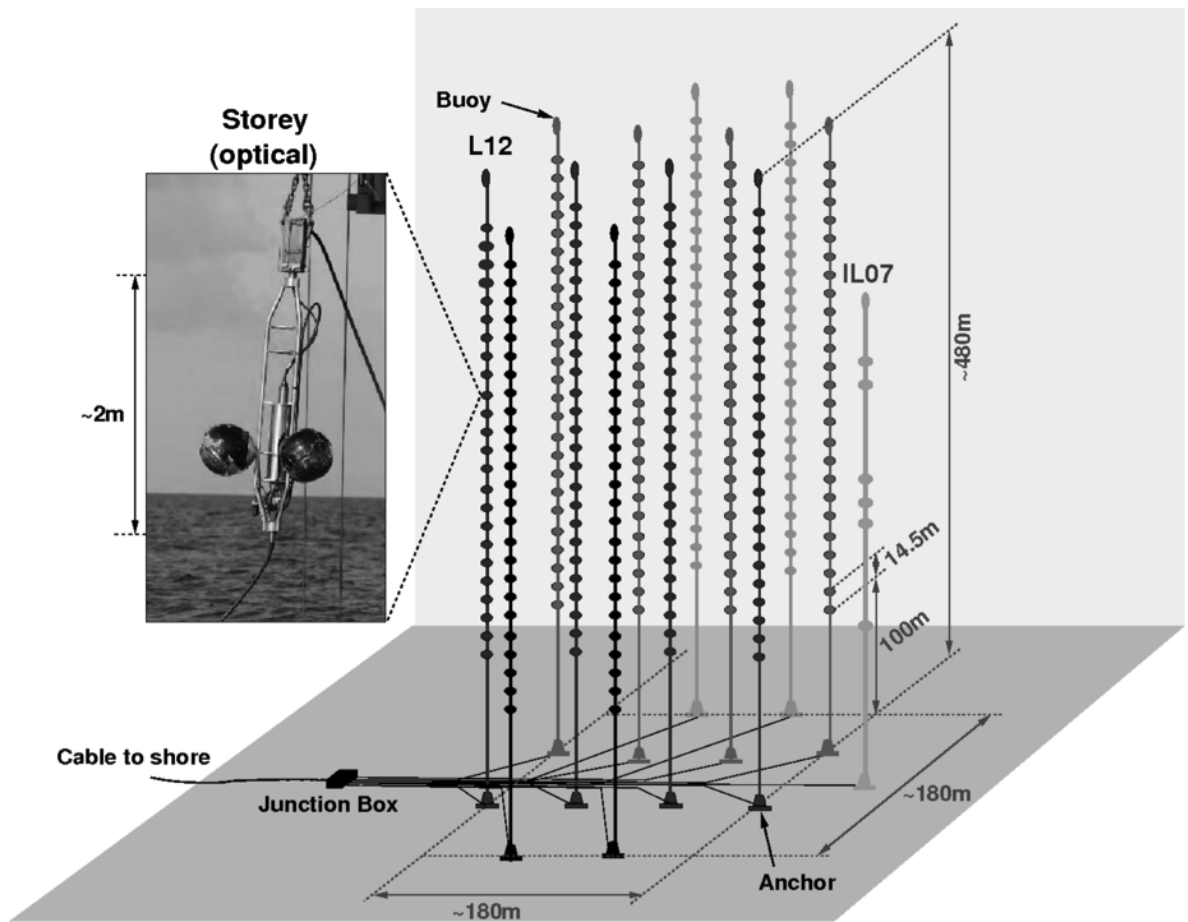


Figure 2.5: Schematic view of the ANTARES 12-line detector

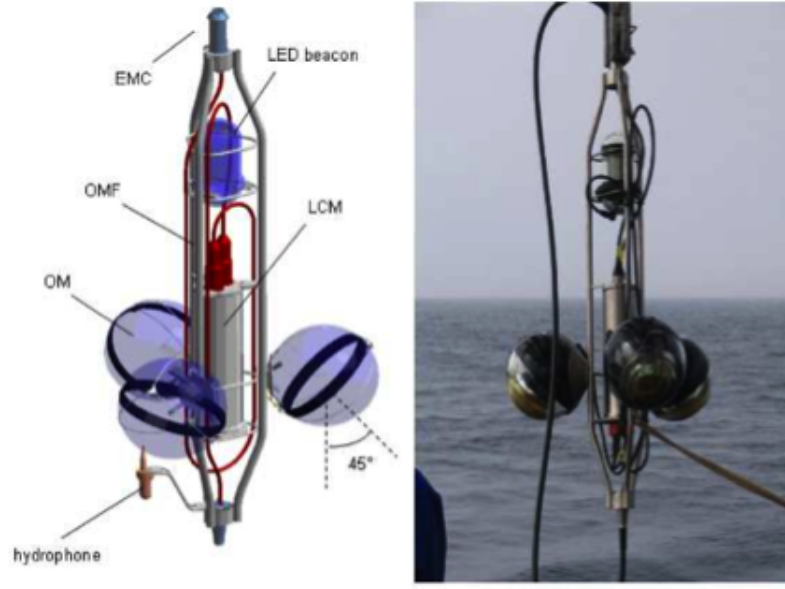


Figure 2.6: Schematic view and picture of an ANTARES storey

ARS board. The processor has a fast Ethernet controller (100 Mb/s) that is optically connected to an Ethernet switch in the Master LCM (MLCM) of the corresponding sector (five storeys form a sector, which is an independent unit concerning the power distribution and the data acquisition system). The specific hardware for the readout of the ARS chips and data formatting is implemented in a high density field programmable gate array (FPGA). The data are temporarily stored in a high capacity memory (64 MB SDRAM).

- The Clock card, which receives the reference time signal from the lower LCM and distributes it within the storey. It also pass the clock signal, generated on shore, to the next LCM of the line.
- The Compass board, which measures the heading, pitch and roll of the LCM. This measure is important for the reconstruction of the line inclination and PMT position.

Some storeys include a set of devices for calibrations.

Laser and LED beacons are used to evaluate the relative time delays, whereas the alignment is monitored with acoustic emitters and transceivers, tiltmetres (sensitive inclinometer designed to measure very small changes from the vertical level) and compasses. Also the absolute orientation is monitored with the triangulation of acoustic signals, emitted by the hydrophones, between lines and the deployment vessel at the sea surface using GPS.

In the next paragraph the main device of the storeys is described: the optical module.

2.3.2 The optical module

The optical module (OM) consists of a pressure resistant glass sphere, 45 cm in diameter and 15 mm thick containing a PMT to detect Cherenkov photons. Commercially available VITROVEX 17" glass spheres were used. These sphere are tested for usage till 7000 m depth.

A schematic view and a picture of the optical module is shown in Fig 2.7.

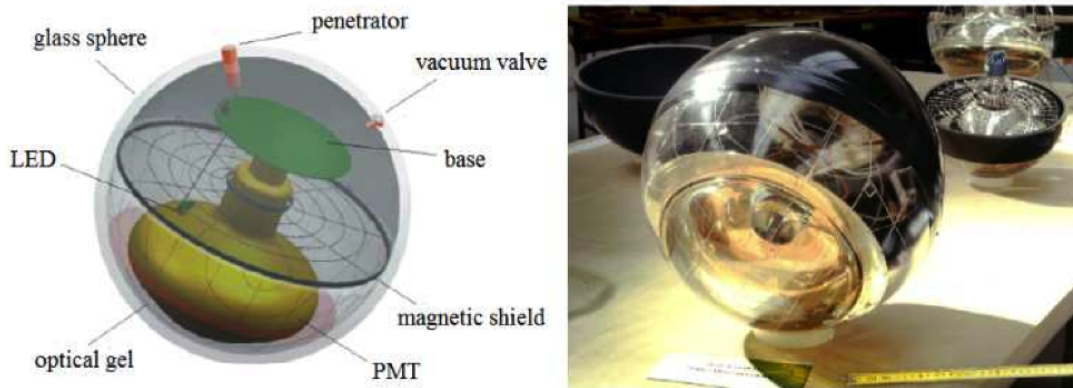


Figure 2.7: Schematic view and picture of an ANTARES optical module

The sphere houses a large area hemispherical PMT shielded from the Earth magnetic field with a μ -metal cage. In fact the geo-magnetic field can deflect the electrons inside the tube, this phenomenon reduces the PMT efficiency and timing performance.

The cage is a μ -metal hemispherical grid that is flat on the rear of the bulb. However this grid shadows part of the photocathode area, so the ANTARES collaboration found a compromise between this effect and the attenuation of the magnetic field. The cage wire diameter is 1,08 mm and the mesh area is 68 mm², in this way the magnetic shield shadow less than 4% of the photocathode area, but the electron deflection driven by the magnetic field is reduced by a factor 3.

A transparent silicon rubber gel is used to glue the tube to the glass sphere and also as optical link between the sphere and the tube.

The optical modules include also the high-voltage power supply of the PMT, a LED system for internal monitoring and the data transmission system to the outside.

The PMT base is a modified version of the commercial ISEG PHQ5912 base, our optimization reduced the anode signal reflection. This base generates by itself the high voltage for the PMT using the 48V input from the LPB and this high voltage is consequently distributed to the dynodes.

A detailed description of the PMT tube is given in the next paragraph.

2.3.3 The photomultiplier tube

A photomultiplier tube converts a light signal in an electrical signal. The signal is amplified through the emission of secondary electrons.

Fig 2.8 shows the main components of a PMT:

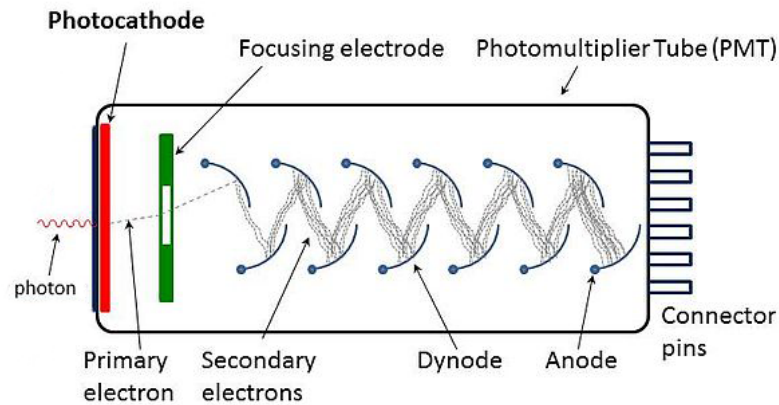


Figure 2.8: Schematic view of the main components of a photomultiplier tube (PMT).

The photocathode converts the photons flux in an electron flux. The incident photons can impart enough energy to some bonded electrons of the photocathode to let them escape, this phenomenon is called photoemission. The photo-electrons are then focused and accelerated by electrodes to reach the first dynode of the tube. When an electron strikes the first dynode there is a secondary emission of electrons. This process continues through all the dynodes of the tube increasing exponentially the electron flux. Finally the electron flux is collected by the anode that provides the output signal.

The PMTs chosen for the ANTARES detector are large photocatode area Hamamatsu R7081-20 tubes (10" diameter). The large photocatode is really important for the detection of muons in water, but these PMTs present other important interesting performances.

The Quantum Efficiency (QE), which is the percentage of photons hitting the device's photoreactive surface that produce charge carriers, is really high (above 20%). Also the collection efficiency is higher than 80% and the Transit Time Spread (TTS), that is the fluctuation of the photo-electron pulse transit time, is below 3 ns.

The Hamamatsu R7081-20 tubes are designed for the detection of light in the wavelength

range between 300 and 600 nm, so they can efficiently detect the Cherenkov photons (400-450 nm).

The typical signal due to a single photo-electron is a 45 mV peak with 20 ns width. The time of the signal is digitised if it exceeds the threshold (typically 1/3 of the peak) and the signal charge is integrated. The dark noise rate is expected to be below 10 kHz for a threshold of 0.3 photo-electrons.

In the next sections the environmental condition of the detector are described, in particular the main optical and physical backgrounds are presented in Sec. 2.4.

2.4 ANTARES effective area

The effective area is defined as the surface the detector would have perpendicular to the incident particle beam if its detection efficiency was 100%. It can be calculated from the ratio of the rate of detected muons (s^{-1}) over the incident flux ($cm^{-2}s^{-1}$). Consequently for an incident muon flux at the detector, this gives the muon effective area, for an incident flux of neutrinos at the Earth surface, this gives the neutrino effective area.

2.4.1 Muon effective area

The muon effective area gives the detection rate of the detector to an incident muon flux, whatever the process that gave rise to this flux. The muon effective area is shown in Fig 2.9 obtained through a simulation of neutrino charged current interactions.

The two first curves are respectively for reconstructed muons matching the neutrino angle at less than 1 degree and less than 0.3 degrees. The last curve is the result of the selection criteria that lead to the angular resolution curve shown in Sec. 2.2, namely better than 0.3 degrees above 10 TeV.

The green line represents the ground surface covered by the instrumented volume. At high energies the effective area reaches or even exceeds the geometrical surface. It is a common feature of neutrino telescopes: the neutrino cross-section increases with energy and the muon traveling range can reach several kilometers at the highest energies.

2.4.2 Neutrino effective area

The muon-neutrino effective area is much smaller than that of the muon effective area since it takes into account the probability for a muon neutrino to interact and to give a muon that can be seen by the detector (Fig 2.10).

It is below a few tens of square meters in all the ANTARES energy range. Around the

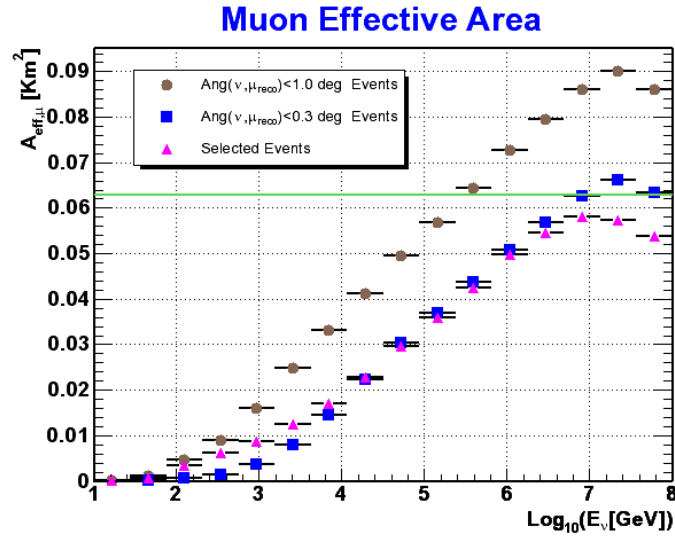


Figure 2.9: Muon effective area (obtained from simulated charged current neutrino interactions). Brown/blue points represents angular distance between reconstructed upgoing muon and MC-true neutrino direction below $1^\circ/0.3^\circ$. Magenta points show angular distance between reconstructed upgoing muon and MC-true neutrino direction after quality track selection of point source analysis [31].

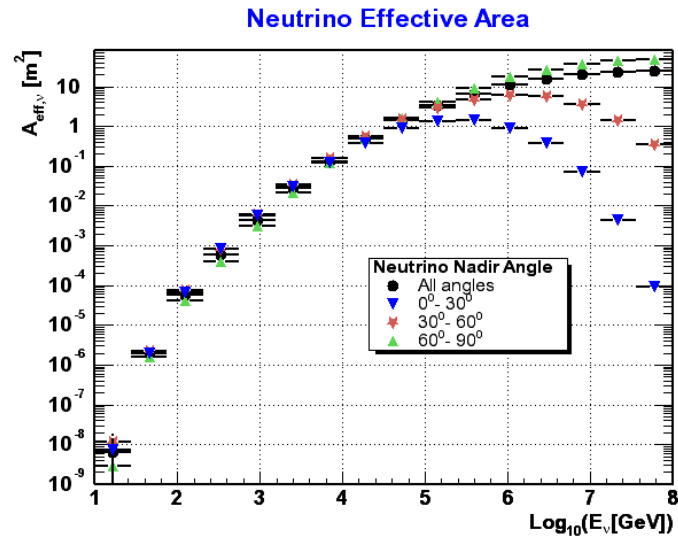


Figure 2.10: Neutrino effective area for several angle ranges.

vertical (0-30°) and above 100 TeV, the Earth starts to become opaque to neutrinos, in this two cases they interact early and the produced muon can not reach the detector before decaying. At larger angles the effect of the dense core of the Earth is smaller and this effect occurs later in energy. As a consequence the detector remains very efficient at very high energy for nearly horizontal neutrinos.

2.5 The ANTARES sea water properties

Absorption and scattering of light in the water affect the performance of the detector. In fact the absorption reduces the number of photons that reach the PMTs, whereas the scattering changes the path and the arrival time of Cherenkov photons. With high density of absorption centres in the medium, a large fraction of photons will be lost before reaching the OMs. The shorter is the scattering length, the larger will be the number of delayed photons that will reach the OMs.

The absorption and scattering lengths are function of the light wavelength, their dependence is shown in Fig 2.11 and Fig 2.12.

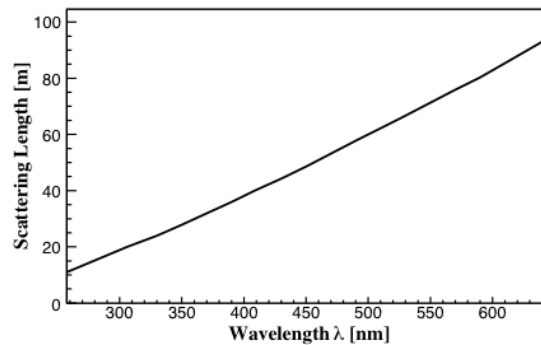


Figure 2.11: Scattering length in water as a function of the wavelength [32].

More details on the estimations of Fig 2.11 and Fig 2.12 are provided in the next sections. The measure of this quantity is important since an uncertainty of the 25% in the scattering can change the event rate by at least 10% [33].

The angular resolution worsening due to the scattering is most relevant for high energy events (> 100 TeV), because at that energies the quality of the reconstruction algorithm dominates, whereas at lower energies the angular resolution is affected mainly by the neutrino-muon angle at the interaction vertex. Also the absorption length uncertainty can change the expected baseline rate of the detector. The baseline rate is defined as the

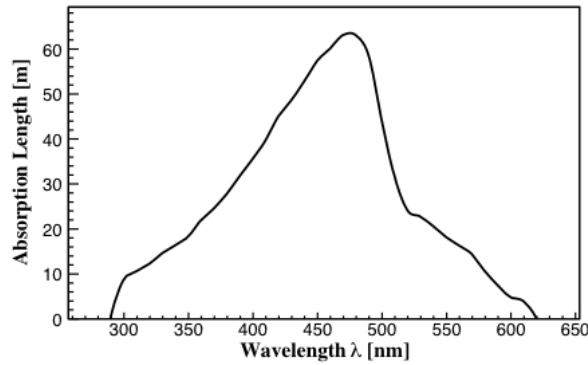


Figure 2.12: Absorption length in water as a function of the wavelength [32].

continuous component of the PMT count rate. In fact a variation of the absorption length of the 10% can reduce/increase the number of the detected photons between 10%-20%. The main phenomena regarding the propagation of light are described in the next paragraphs.

2.5.1 Light transmission, absorption and scattering

If a collimated beam of light $\Phi_i(\lambda)$ go through a small volume of water of thickness ΔV , some photons will be absorbed $\Phi_a(\lambda)$, other part will be scattered $\Phi_s(\psi, \lambda)$ at an angle ψ ($0 < \psi < \pi$) and the rest will be transmitted without deflections $\Phi_t(\lambda)$ (Fig 2.13).

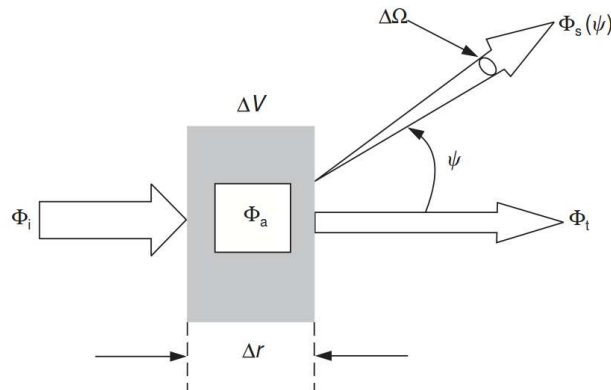


Figure 2.13: All the processes occurring incident beam crosses a section of matter are summarized by the transmission of light plus absorption and scattering response of the medium, as conservation of energy.

The radiant intensity I is defined as the spectral radiant power from a source that is directed into a particular direction along the centre of a cone encompassing a solid angle $\Delta\Omega$. According to the Beer-Lambert law the radiant intensity is altered by the attenuation effect as [34]:

$$I = I_0 \cdot e^{-c(\lambda)x} = I_0 \cdot e^{-[a(\lambda)+b(\lambda)]x} \quad (2.4)$$

where $c(\lambda)$, $a(\lambda)$ and $b(\lambda)$ are respectively the attenuation, absorption and scattering lengths.

The absorption length is the length at which the probability that a particle has not been absorbed into a material has dropped to $1/e$, similarly is defined the scattering length.

2.5.2 The scattering

The volume scattering function $\beta(\lambda, \psi)$ is defined as the probability of a photon of wavelength λ of being scattered by an angle ψ per unit length. This function can be explained using the total scattering probability

$$b(\lambda)[m^{-1}] = \int_0^\pi 2\pi \sin(\psi) \beta(\lambda, \psi) d\psi \quad (2.5)$$

or the angular scattering function

$$\hat{\beta}(\lambda, \psi) = \frac{\beta(\lambda, \psi)}{b(\lambda)} \quad (2.6)$$

According to the previous definition the normalization condition is preserved:

$$2\pi \int_0^\pi \hat{\beta}(\lambda, \psi) \sin(\psi) d\psi = 1 \quad (2.7)$$

These two functions are useful to reproduce the scattering in the Monte Carlo simulations. In presence of many scattering processes the total volume scattering function is defined as

$$\beta(\lambda, \psi) = \sum_{i=1}^{N_p} b_i(\lambda) \hat{\beta}_i(\lambda, \psi) \quad (2.8)$$

In the Smoluchowski-Einstein modelling of the light scattering in pure sea water the angular scattering function [35] is

$$\hat{\beta}_{SE}(\psi) = \left(\frac{3}{8\pi} \frac{1+\delta}{2+\delta}\right) \left(1 + \frac{1-\delta}{1+\delta} \cos^2\psi\right) \quad (2.9)$$

where δ is the depolarisation ratio ($\delta=0.09$) [35], a correction due to the anisotropy of the water molecules. It can be considered independent from salinity, pressure and temperature. It is important to note that this function is also independent of the wavelength and approximately symmetric around 90° .

According to the Smoluchowski-Einstein model the total scattering probability is wavelength dependent:

$$\beta_{SE}(\lambda) = \beta_{SE}^0 \left(\frac{550nm}{\lambda}\right)^{4.32} \quad (2.10)$$

where β_{SE}^0 is a coefficient dependent from salinity, temperature and pressure of the sea water. The power index is different from the Rayleigh scattering because of the wavelength dependence of the refraction index [36].

The measured values of δ (0.1) and β_{SE}^0 ($1.94 \cdot 10^{-3} m^{-1}$) are in good agreement with the values derived from the model used in the ANTARES Monte Carlo simulations ($\delta=0.09$, $\beta_{SE}^0=1.7 \cdot 10^{-3} m^{-1}$) [37].

In sea water the main contributors to the light deflection is due to the scattering of photons on particles contained in the sea water. A model for this kind of interaction is provided by Mie. It is assumed that the photons scatter on spherical particle of known size. However the sea water contains particles of different sizes from $0.1 \mu m$ to $100 \mu m$.

A more refined model is provided by Kopelevich that assumes the presence of two different kind of particles, “large” and “small” [37]. According to the Kopelevich model the volume scattering probability is

$$\beta(\lambda, \psi) = 1.34\nu_s \hat{\beta}_s(\psi) \left(\frac{550nm}{\lambda}\right)^{1.7} + \nu_l \hat{\beta}_l(\psi) \left(\frac{550nm}{\lambda}\right)^{0.3} \quad (2.11)$$

where the particle concentrations ν_s and ν_l are measured experimentally. $\hat{\beta}_s$ and $\hat{\beta}_l$ are the associated angular scattering functions, which are derived from the model and tabulated in [37].

This model is claimed to have a systematic error lower than 30%, however in the ANTARES Monte Carlo the values of $\hat{\beta}_s$ e $\hat{\beta}_l$ measured by Petzold are used [38].

The result of the ANTARES model of light scattering is quite well in agreement with the measurement of Mediterrean sea water [32].

2.5.3 The absorption

The light absorption in sea water is due to the water molecules, the coloured dissolved organic matter and the chlorophyll molecules grown in phytoplankton cells. The scattering associated to water molecules can provide an attenuation of the photons of around 25% at wavelengths between 370 and 450 nm. In this wavelength range the scattering is caused by electronic transitions within the water molecules, whereas at wavelength above 450 nm the photons excite vibration modes of the O-H bound in the water molecule.

A well-known model of the absorption by pure sea water is provided by Smith and Baker [39]. In their study they assume absorption only by water molecule and salt ions scattering, neglecting the inelastic scattering and absorption by other substances. This model allows an estimation of the absorption for blue light with an accuracy around 20%.

The absorption length measurements used by the ANTARES collaboration were performed in the Mediterranean Sea [40]. These measurements are corrected according to the Smith and Baker measurement in pure sea water. An AC9 transmissometer was used to measure the absorption and attenuation length at different wavelength in the ANTARES site [32].

If the absorption length is shifted on the wavelength axis according to this measurement, the absorption length curve is in good agreement with the measurement performed with blue and ultraviolet LEDs at the ANTARES site (Fig 2.14) [41].

2.6 Background sources

2.6.1 The optical background

At the ANTARES site there are two main processes that contribute to the optical background: the bioluminescence and the radioactive decay of the ^{40}K . An example of the detection rate of three ANTARES optical modules is shown in Fig 2.15.

From Fig 2.15 are defined two values that are used to determine the quality of a data sample: the baseline and the burst fraction. The baseline is defined as the flat part of the rate distribution and the burst fraction is defined as the percentage of time (during one data run) where the counting rate is higher than 1.2 times the baseline.

The bioluminescence comes from the light produced by various organisms. It is a form of

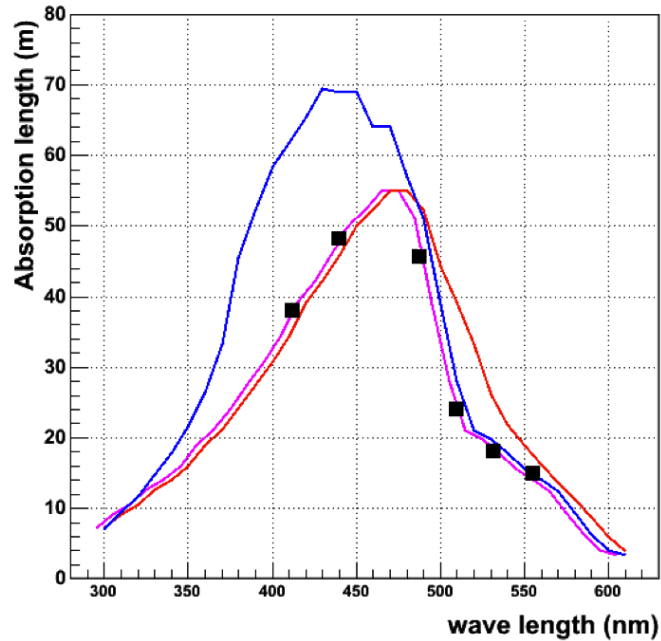


Figure 2.14: Different measurements of the absorption length: Mediterranean sea water (red line), pure sea water in the Sargasso sea (blue line), measurement with the AC9 transmissometer (black squares) performed at the ANTARES site, absorption length fit used in the ANTARES water model (purple line). The fit is based on the predictions of the Smith and Baker model.

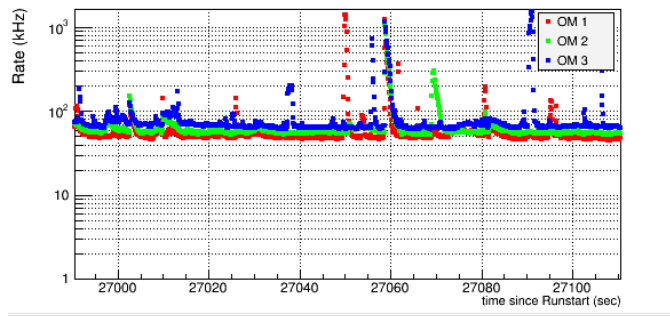


Figure 2.15: Counting rates of three optical modules on 29th July 2015.

chemiluminescence where the light energy is released by a chemical reaction. The bioluminescence has its wavelength spectrum maximum in the range from 450 nm to 490 nm, which is the best wavelength for the transmission of the light. This background can provide a consistent increase of the optical background, several order above the ^{40}K contribution but these bursts end in a few seconds. This background is more consistent during spring when the activity of the bioluminescent organisms is more intense and there is a water exchange from the surface layers that are rich of luminescent plankton [42].

A correlation has been found between the fraction of time during which the instantaneous background exceeds the base line rate by at least 20%, the burst fraction, and the absolute sea current velocity (Fig 2.16).

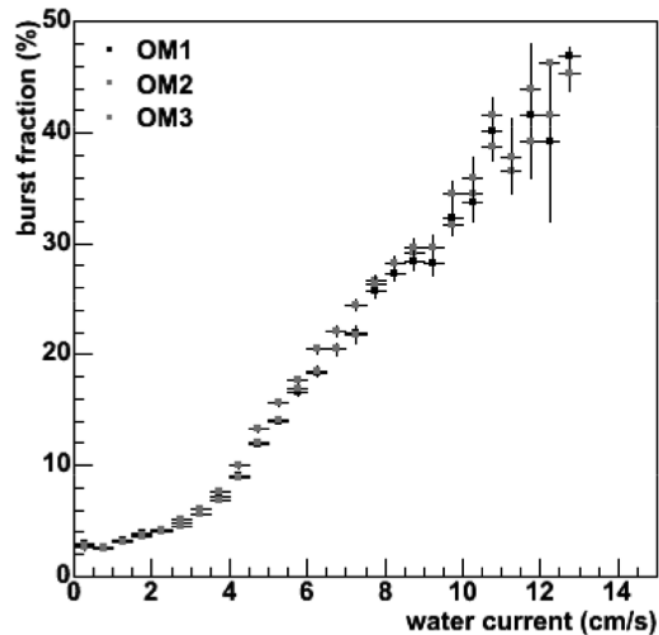


Figure 2.16: Correlation between the burst fraction and the sea current velocity, measured at the ANTARES site. An increased bioluminescence activity is observed for higher current velocities.

The rapidly changing background peaks in Fig 2.15 are produced by non microscopic animals, when they are disturbed by the detector structure or by turbulence in the sea water. No correlation has been found between the sea current velocity and the baseline rate. On the other hand, the sea water contains about $4.5 \cdot 10^{-5}$ g/l of potassium ^{40}K radioactive isotopes with activity above 14 kBq/m³, which emits β and γ particles when decaying through β -decay and e-capture respectively.

The decay of ^{40}K can produce photons that could be detected by the ANTARES OMs. The two main decay channels are

$$^{40}\text{K} \rightarrow ^{40}\text{Ca} + e^- + \bar{\nu}_e \quad (BR = 80.3\%)$$

$$^{40}\text{K} + e \rightarrow ^{40}\text{Ar} + \nu_e + \gamma \quad (BR = 10.7\%)$$

The maximum energy of the emitted electrons is 1.33 MeV, a large fraction of them being above the Cherenkov threshold for light production, whereas the photons emitted in the electron capture process have an energy of 1.46 MeV. These photons can lead to Compton scattering producing more electrons above the Cherenkov threshold. The average decay rate of the ^{40}K is almost stable over time, so it produces a constant rate of hits on the ANTARES PMTs around 40 kHz.

2.6.2 The atmospheric backgrounds

The two physical background sources of the ANTARES telescope, atmospheric muons and neutrinos, are both originated by the cosmic rays.

The atmospheric muon background

The atmospheric muons are produced in the upper atmosphere where the cosmic rays interact. Typically they are sufficiently energetic to travel some thousand of kilometres in the atmosphere and to reach the detector. However an atmospheric muon can not cross the diameter of the Earth and reach the detector from the antipodes, so this background can be reduced selecting only the upgoing tracks. The rate of downgoing reconstructed tracks due to atmospheric muons is several Hz, so the part of the sky above the horizon can not be used for the search of cosmic neutrinos (unless of extremely high energies, above the maximum energy of the atmospheric events). In Fig 2.17 is shown the fraction of simulated and reconstructed muons as a function of the zenith angle θ .

As shown in Fig 2.17, some of the atmospheric muons are reconstructed as up-going events. In fact it is possible that an atmospheric muon track is reconstructed as upgoing because the track is almost horizontal or because of hits of the optical background that seem correlated with an “upgoing” event. This kind of events is one of the main background of the detector in the sky region interesting for astrophysical neutrino source research.

The atmospheric neutrino background

Similarly to atmospheric muons, also neutrinos are produced in the upper part of the atmosphere. However the atmospheric neutrino can cross the Earth, so they can produce

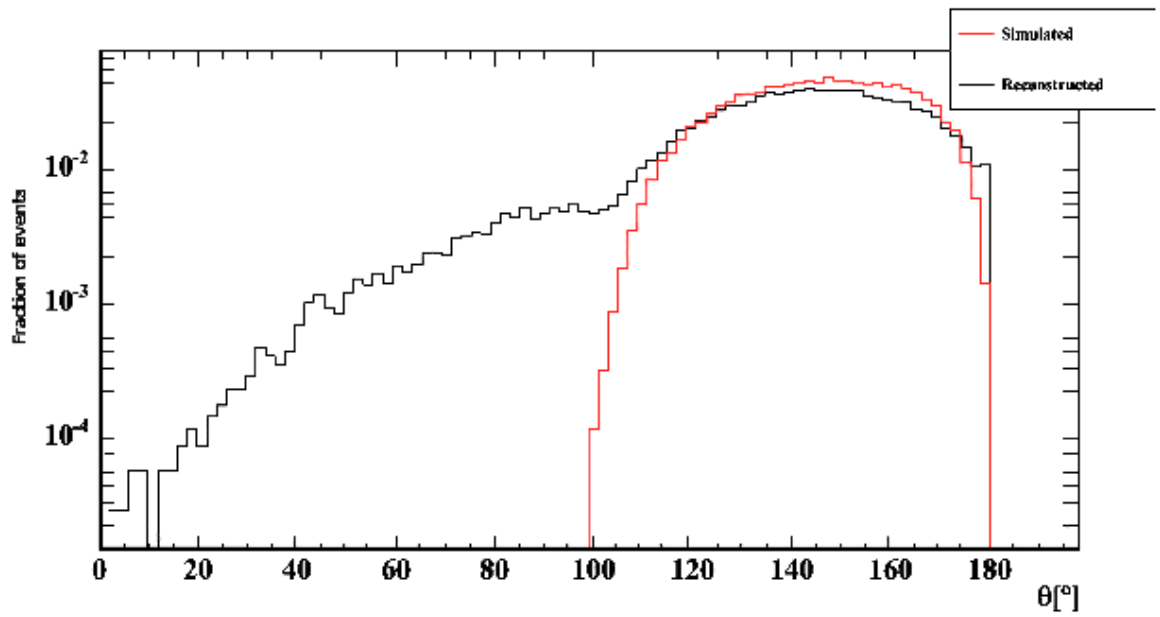


Figure 2.17: Fraction of simulated and reconstructed muons as a function of the zenith angle θ . $\theta=0^\circ$ is the nadir, $\theta=90^\circ$ is the horizontal and $\theta =180^\circ$ is the zenith. This distribution is before any cuts, and reconstructed using the BBFit reconstruction method [43].

upgoing tracks, like cosmic neutrinos. Fig 2.18 shows the comparison of the atmospheric neutrino and muon flux expected at the ANTARES site.

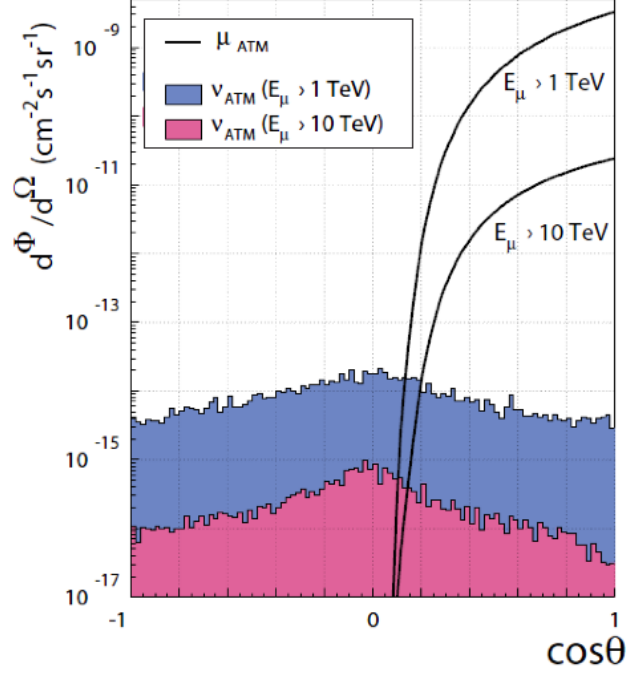


Figure 2.18: Differential flux of atmospheric neutrinos and muons as a function of the $\cos\theta$ angle. The four plots are a result of a Monte Carlo simulation for the ANTARES detector [44].

A muon created by an atmospheric neutrino cannot be distinguished from a muon created by a cosmic neutrino. The atmospheric neutrino background can be reduced measuring the energy of the tracks, typically around some GeV. This energy is lower than the expected energy range of the cosmic neutrino above 100 GeV. The cosmic neutrino diffuse flux may dominates over the atmospheric neutrino background and they can be identified by their harder and softer energy spectrum respectively.

In order to distinguish between atmospheric and cosmic neutrino the characteristic of the source can also be used. For example a cluster of events in space correlation with a point source or an anisotropy in a large scale search can be indicative of the presence of cosmic neutrino. Moreover in the case of the transient source research, like GRBs, we have also the information about the emission time. The detection of a cluster of events in time coincidence with a transient source is an indication of the presence of a cosmic neutrino flux

from the astrophysical object.

Chapter 3

The data acquisition system

3.1 Introduction

The data acquisition system (DAQ) permits to convert the analogical signals of the optical modules into a digital signal that can be stored and subsequently used for physical analysis. The system includes the conversion of the analogical signals, the transportation and filtering of the data and finally the storage. The DAQ system includes a large network of processors both off-shore, integrated in custom electronics, and on-shore (PCs).

The two stages of the data acquisition system are connected with the interlink and MEOC cables described in Sec.3.2. A scheme of the DAQ system is shown in Fig 3.1 and is described hereunder.

3.2 The digitalization of the signals

If a signal in a PMT exceeds a certain threshold, the signal is read-out and digitized by a custom application-specific integrated circuit, the Analogue Ring Sampler (ARS) [45]. It has a local clock for the determination of the time of arrival of the signal. The ARS has time resolution better than 0.4 ns and its dead time is 225 ns.

Each PMT is connected to a pair of ARS readouts, which treats the signals alternatively via a token ring system. It takes about 13 ns to pass the token so during this time the PMT signal is not elaborated. The timeline of this process is shown in Fig 3.2.

The ARS can discriminate single photoelectron pulses (SPE) and other complex waveforms.

Many different characteristics of the signal are measured by the ARS: the amplitude, the time of threshold crossing and the presence of multiple peaks within the time gate, but only charge and amplitude are recorded. The charge of the signal is integrated by the ARS

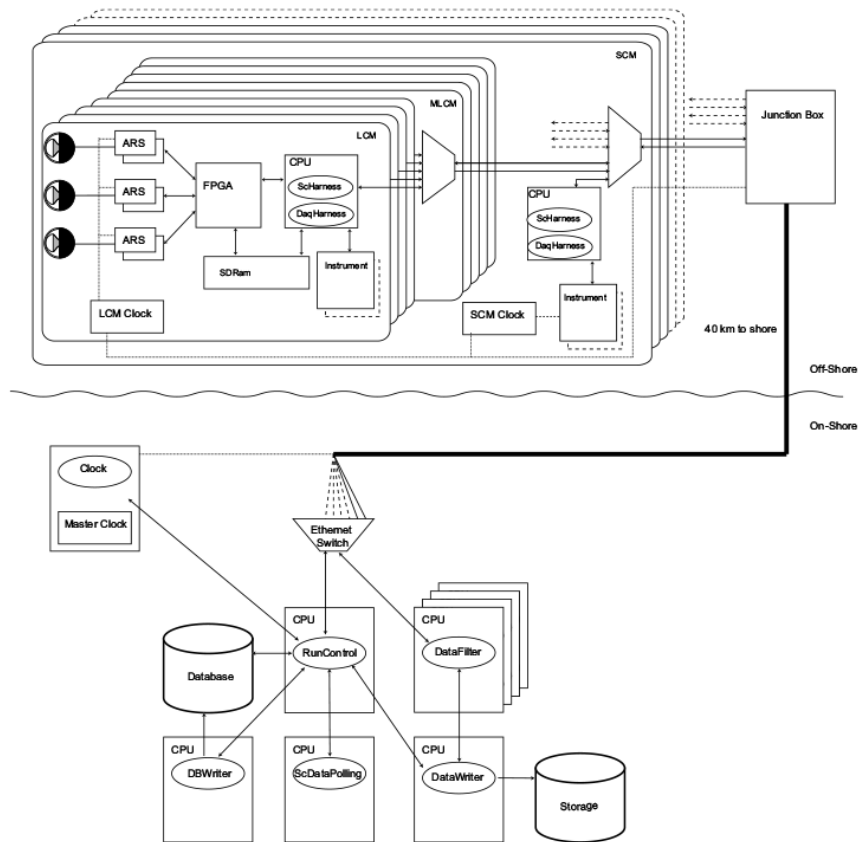


Figure 3.1: A schematic view of the ANTARES data acquisition system.

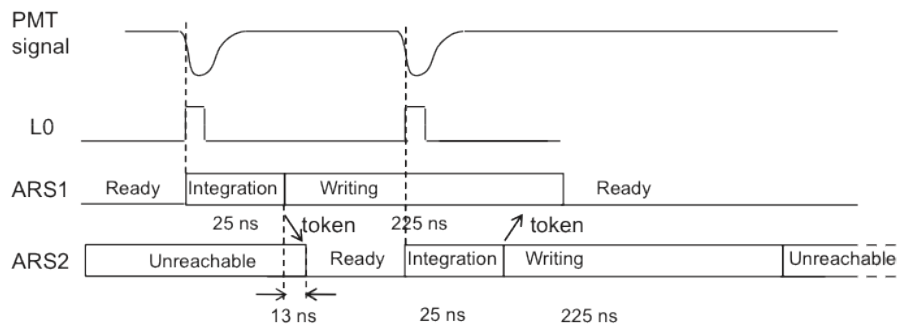


Figure 3.2: Timeline of two consecutive PMT pulses and the corresponding occupancy in the front-end electronics.

using two 8-bit ADCs with an integration gate of 40 ns.

In each storey there are 6 ARS, which are read out by a Field Programmable Gate Array (FPGA). This arranges the hits produced in a time window into a dataframe and stores it in a 64MB Synchronous Dynamic Random Access Memory (SDRAM). All the dataframes recorded in the time windows of $104.8 \mu\text{s}$ form a TimeSlice. A 20 MHz clock generated off shore is used to synchronize the ARS and a master clock connected through an optical fibre provides a time reference for this clock.

The data transmission is controlled by two programs. The DaqHarness manages the transfer of the dataframes to the control room, whereas the SCHarness handles the transfer of the monitoring and calibration data (so-called slow control).

Transmission Control Protocol and Internet Protocol (TCP/IP) are used for communication and data transfer. An optical bidirectional 100 Mb/s link connects the Local Control Modules (LCM) in a sector with their Master LCM. These links are merged using the Ethernet switch of the MLCM into a single Gb/s Ethernet link.

An electro-optical cable connects each string to the junction box (JB) and a 40 km long optical cable connects the JB to the shore station.

Finally data are written on disk and sent to the Lyon CC-In2p3 computing centre through Internet and stored on tape.

3.3 The data filtering and storage

All the signals digitized by the detector are sent to the shore station without any further selection. The data stream during periods with low bioluminescence is around 0.4 GB/s [46]. Because the storage of all this data output is not feasible, trigger algorithms are applied to reject the optical background. The algorithms look for space-time correlations that are coherent with the particle traversing the instrumented volume. These events are selected by the DataFilter program and then written to disk by the DataWriter program.

The DataFilter program looks for correlation in the whole detector in a time window of $2.2 \mu\text{s}$ and if an event is found, DataWriter store all the hits detected in the time window. The time windows is $2.2 \mu\text{s}$ long, because it roughly corresponds to the time needed by a relativistic particle to cross the entire detector. The DataFilter is disabled when a GRB alert is received.

In the next two paragraphs the normal data taking and the special data taking in correspondence of a GRB is described.

3.4 The standard data taking

The global data rate of filtered data in the standard configuration is around 0.15 MB/s [46]. All these data are stored with the start and end time of the run together with the present detector conditions. Most of the hits due to the decay of ^{40}K are reduced by a factor 10^4 by the first filtering algorithm.

The first filtering requires simply a correlation of the hits in the same storey, since the background is expected to be uncorrelated. The so-called L1 hits are events where two hits in the same storey are detected within 20 ns or a single hit with amplitude above 3 photoelectrons. Subsequently the cluster algorithm in the DataFilter uses the following causality relation to search for correlation in the found L1 hits [46]

$$|\Delta t| \leq \frac{n_g}{c} \cdot d \quad (3.1)$$

where Δt is the time difference between two L1 hits, n_g/c is the group velocity in water and d is the distance between the optical modules. An additional safety interval margin of 20 ns is added to the formula in order to take into account the uncertainties on the position and time of the hits and the light scattering. A sample of hits that satisfy this condition is called cluster.

Finally a physics events is stored if the cluster contains at least 5 L1 hits. When a physics event is detected all the hits 2.2 μs before the first L1 hit and 2.2 μs after the last hit are stored without any filtering. In fact 2.2 μs is the time that a relativistic muon takes to traverse the detector.

There is also a set of second level triggers that are applied on L1 data that looks for the correlation between the hits and a track direction. These triggers have different efficiency on the neutrino detection and they are set for each run separately depending on the optical background conditions. Typically the triggers are set in order to have a detector event rate around 50 Hz (mostly downgoing muons), which produces about 1 GB of physics events in 2 hours.

3.5 The standard triggers

The ANTARES DAQ system runs multiple triggers simultaneously. The goal of most of the applied triggers is the detection of relativistic muons, thus only two trigger are designed to trigger on slowly moving particles. The main properties of the ANTARES triggers are:

Trigger T2 and T3: T2 and T3 algorithms trigger on local clusters of hits in the same line and adjacent floors. For T3 the number of floors can be adjusted, while for the T2 the number of floors is always two. The algorithm first makes a list of pairs of cluster, each pair must satisfy the condition on the maximum distance between the floors and the preset time window. A trigger is set when the number of pairs within a predetermined time window exceeds a given minimum.

Trigger 3M: 3M is a simple majority trigger. A trigger is set if the number of consecutive hits within a preset time window exceeds a given minimum.

Trigger 3D: 3D is similar to 3M, but this time the hits are processed through a three-dimensional clustering algorithm. If the sample of hits selected after clustering is large enough, the trigger condition is met.

Trigger 1D: 1D algorithm rotates the positions of all the PMTs such that a hypothetical muon direction is along the z-axis (several directions are taken into account doing a scan over the sky) and one-dimensional clustering algorithm is applied.

Trigger 3N: 3N is a combination of 3D and 1D. First 3D clustering algorithm is applied, then the selected hits are rotated like in 1D and the scan over the sky is performed.

Trigger MX: MX is a special directional trigger. This trigger has a key role in this thesis, so it will be described extensively in Sec.3.8.

Trigger GC: GC is the same algorithm of MX, but the direction is always fixed to the centre of our galaxy.

It is important to highlight that all triggers, except MX and GC, take into account only L1 hits in their algorithm. The two special directional triggers MX and GC combines L0 and L1 data. L0 data are all raw data recorded by ANTARES without any correlation condition applied. More details on L0 data are given in Sec.3.7. Furthermore MX is the only trigger applied offline. The other triggers which are used for the data taking are set for each run separately depending on the optical background conditions.

3.6 The GRBs alert network

The external detection of transient sources such as GRBs can be used to enhance the sensitivity of ANTARES with the notification of one of these events in a short time. In that case the data taking conditions can be optimized for the measurement of the burst. This is true not only for ANTARES but also for other detectors: for this reason a GRB

alert network has been created. The alert is distributed to many telescopes around the world when one of the satellites of the network detects a GRB.

The GRB warning is an efficient method to observe GRBs. All satellites capable of GRB detection that were launched since BATSE (1991) are part of these network. All interested telescopes, like ANTARES, which subscribe to the system, are updated promptly with the most recent GRBs information. The instantaneous distribution of the alert is crucial for the detection of the GRB afterglow. The GRB afterglow fades rapidly, so a fast alert is critical to allow the observation on ground.

The time delay between the detection by a satellite and the delivery of the alert message is shown in Fig 3.3.

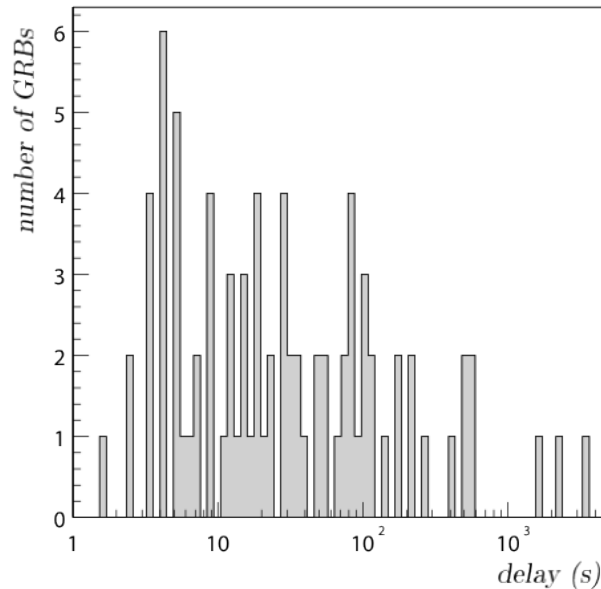


Figure 3.3: Distribution of the delay between the detection of the GRB by the satellite and the time the alert message is distributed.

For 40% of these GRBs the delay is less than 20 seconds and for 75% of these GRBs it is less than 100 seconds. The delay includes the time of GRB detection, the transmission time and the network delay to the central computer of the alarm system.

The position of the GRB is even more important in order to point the telescopes in the right direction (this is not the case of ANTARES). Sometimes the information on the position of a burst is measured more accurately with ground analysis, in this case the refined position is distributed to all the detectors of the network.

The distribution of the time delay of the final confirmation of the GRB and its most accurate information on the direction is shown in Fig 3.4.

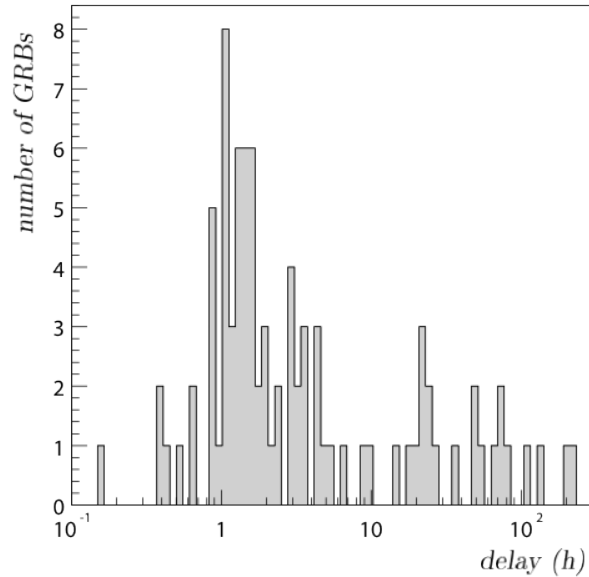


Figure 3.4: Distribution of the delay between the detection of the GRB by the satellite and the time the GRB was confirmed and its position was distributed.

The confirmation arrives within 6 hours after the burst for 70% of the GRBs. The precision of the final information of the burst position is typically of the order of arcminutes, which is perfectly suited for ANTARES.

The time between two alerts is indicated in Fig 3.5. The average time interval between the detection of two gamma ray burst is typically 30 hours. The high frequency alerts messages are typically false alarms that are distributed during short periods of high satellite detection rate. Whereas the long delay between two consecutive alerts correspond to periods when the particle density in the satellite's orbit is high and the satellite alert system is disabled.

3.7 The special data taking

In correspondence to one of these special astrophysical events, the possibility to buffer all data from the detector before filtering can be useful. The idea is that the offline application of a looser trigger to this buffer of data in addition to the information provided by the alert system can improve the detection efficiency. Events like GRBs and supernovae are believed to produce neutrino and are announced at the moment of the detection by other telescopes.

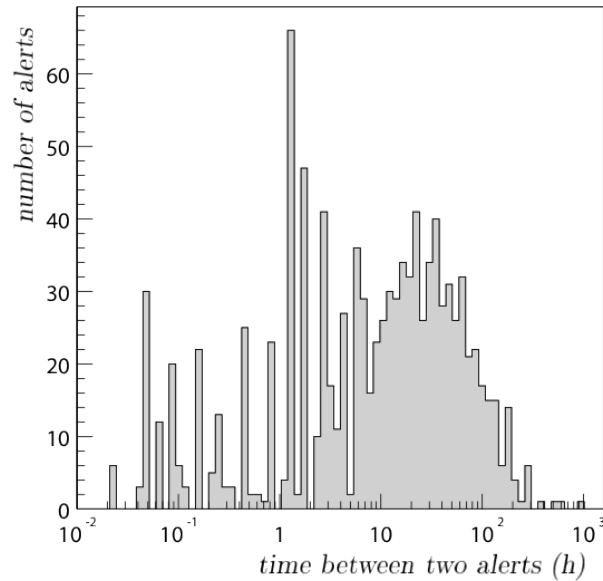


Figure 3.5: Distribution of the time between the arrivals of two alert messages sent by the network.

A special software program `grb_trigger` communicates via the central data distribution package `ControlHost` and is connected with the GRB alert network. When an alert is sent the `grb_trigger` program analyses the content of the message and notifies through `ControlHost` the message to the other DAQ programs. In case of a GRB alert, the `DataFilter` program stops filtering the data and all raw data (L0 data) are saved in the local disks.

Extra raw data taken before the alert message are also saved because they are in the memory of the DAQ programs PC and they have not been filtered yet. This extra data correspond roughly to 250 seconds (100 GB); ANTARES therefore can save the data detected before the alert message is delivered by the satellite up to 4 minutes. In this way the detector records also any possible signal at the beginning of the burst, like prompt neutrinos.

This configuration is maintained for a couple of minutes, in fact a GRB typically last before two minutes, so the typical duration of a GRB data sample is between 4 and 7 minutes (up to 4 minutes of data detected before the alert + 2~3 minutes of GRB duration). Finally the DAQ programs returns in the normal data taking state until another GRB alert is received. If it appears to be a false alarm the data are erased, whereas if the burst is confirmed the most accurate information on the GRB position is stored with the data.

All the filtering for the L0 data is made offline when the data sample is analysed and the position of the GRB is known with the best possible accuracy. The filtering algorithm for

these special data sample (L0 data) is described in the next chapter.

3.8 The special directional trigger MX

In my analysis I have used for the first time in ANTARES the MX trigger to analyse the data in the GRB time window. In the case of the GRB data sample (L0 data) the direction of the neutrino is known, so the algorithm looks for space-time correlation with a looser filter condition because only one direction is considered.

The direction of the muons that originate from GRBs is on average comparable with the direction of the burst, anyway the angular spread depends on the neutrino energy. Fig 3.6 shows the angular difference between the father neutrino and the produced muon as a function of the neutrino energy.

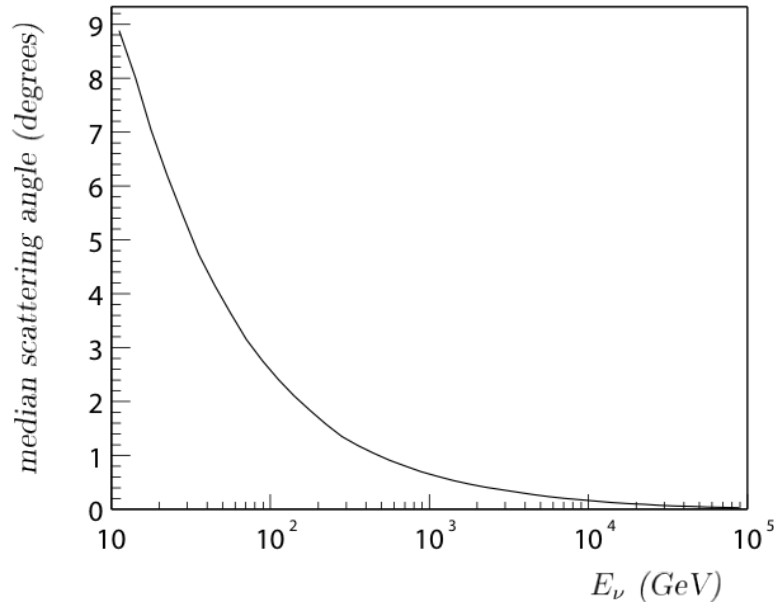


Figure 3.6: The median angle between the primary ν_μ direction and the muon direction as a function of the neutrino energy.

The angular difference is quite small at least above 1 TeV, so the neutrino direction is taken as the direction of the muon.

The GRB direction is provided in equatorial coordinates (declination and right ascension), the algorithm converts it in the local ANTARES coordinate system. Another rotation is then applied in order to choose the z-axis in the direction of the expected muon (the GRB direction), so every component of the detector has now a new set of coordinates. Thanks

to this new coordinate system, the space-time correlation is more stringent than the L1 triggers, because it accepts correlation in only one direction.

The expected arrival time t_j of a Cherenkov photon on PMT_{*j*} is calculated as:

$$t_j = t_0 + \frac{1}{c} \left(z_j - \frac{r_j}{\tan \theta_c} \right) + \frac{1}{v_g} \frac{r_j}{\sin \theta_c} \quad (3.2)$$

where t_0 is a reference time, c is the light velocity in vacuum, v_g is the group velocity of light in water, θ_c is the Cherenkov angle, z_j and r_j are the coordinate of PMT_{*j*} in the new coordinate system (Fig 3.7). In other words r_j is the distance of closest approach from the PMT_{*j*} to the muon track. The second term of expected arrival time formula is the time that a muon takes to travel to the point where the detected photons emitted and the third term is the time that the photon takes to travel to the PMT_{*j*}.

Using the example in Fig 3.7 a correlation condition can be derived.

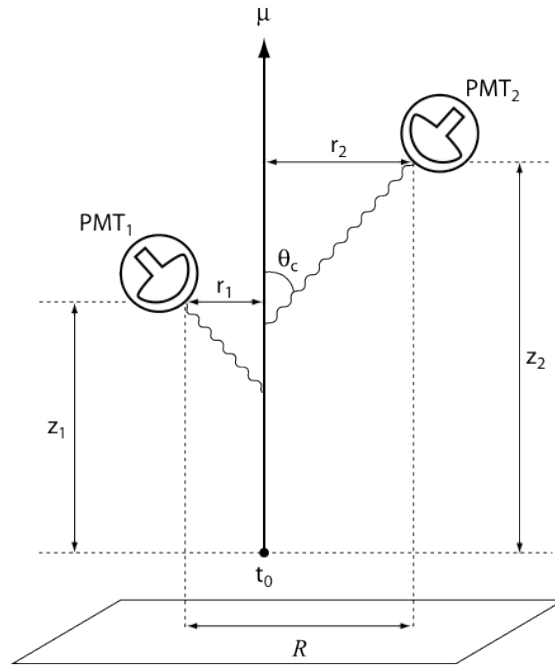


Figure 3.7: Schematic view of a muon traversing the detector. The Cherenkov photons are emitted under an angle θ_c with respect to the muon track.

The expected direction of the track is known, but not its exact location within the detector,

so the r_1 and r_2 values are not known. However the value of r_2-r_1 is maximum when the muon crosses PMT_1 and minimum when it crosses the PMT_2 .

The absolute values of the minimum and maximum are identical and the modulus R is the distance of the two PMTs projected on a plane perpendicular to the muon track. So the correlation condition is

$$\frac{1}{c}(z_2 - z_1) - \frac{\kappa}{c}R \leq t_2 - t_1 \leq \frac{1}{c}(z_2 - z_1) + \frac{\kappa}{c}R \quad (3.3)$$

where κ is

$$\kappa = \frac{c}{v_g} \frac{1}{\sin\theta_c} - \frac{1}{\tan\theta_c} \quad (3.4)$$

An extra 20 ns error margin is accepted to account for the calibration uncertainties and light scattering.

The last constrain on correlated hits is set on the maximum transverse distance between two hits, in this way the number of accidental correlations due to random background is minimized. The Cherenkov light intensity decreases exponentially as

$$I \propto \frac{\sin\theta_c}{r_j} e^{-\frac{r_j}{\sin\theta_c \lambda_{abs}}} \quad (3.5)$$

where $\frac{r_j}{\sin\theta_c \lambda_{abs}}$ is the flight length of the photons and λ_{abs} is the absorption length (around 70m). So a reasonable limit in the maximum transverse distance is twice the absorption length, in other words the transverse distance R can not exceed 140 m. In Fig 3.8 the event rate due to random background is shown as a function of the zenith angle for different cuts on the maximum transverse distance.

Obviously the event rate decreases for smaller transverse distance. The difference between vertical and horizontal direction is due to the different spacing of storeys (14.5 m) and lines (around 60 m). For vertical directions all the storey of a line are within the maximum transverse distance, whereas for horizontal directions only a few OMs of the line will satisfy the condition.

The final selection on the maximum transverse distance depends on the zenith angle (Fig 3.9) and it is chosen in order to have a rate around 2 kHz in each direction.

The MX correlation condition for L0 data is more stringent than the standard filtering. It reduces consistently the number of selected hits, in percentage the reduction is lower when

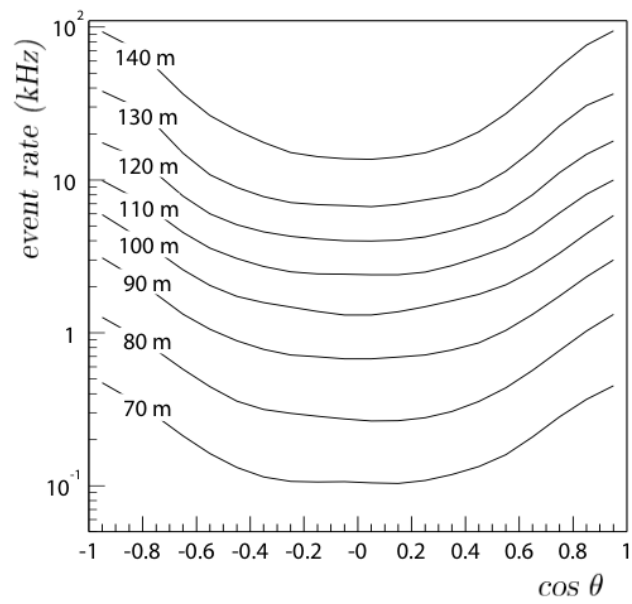


Figure 3.8: Event rate as a function of the maximum transverse distance and the direction angle θ . The rate is averaged over ϕ .

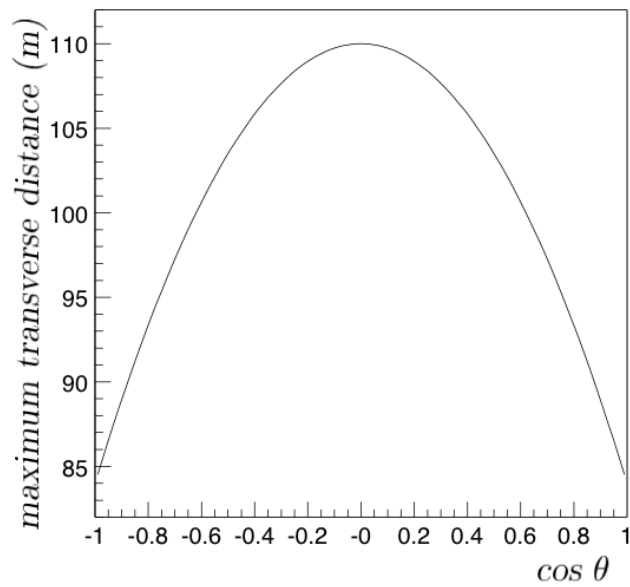


Figure 3.9: Maximum transverse distance as a function of the direction.

triggering an L1 file with standard triggers. We must remind that only hits correlated with the GRB direction are considered, so we obtain a great reduction on the number of hits considered in the analysis without losing any signal in the interesting region around the burst. In other words I obtain a great reduction of the dimension of the data file (untriggered L0 data of a GRB alert are around 100 Gb), I reject many events not correlated with the GRB direction and finally I will have more hits in the interesting region that would be lost if L1 data were used.

The minimum requirement for a physics event is that the cluster contains at least 6 correlated L0 hits. This is a good compromise between the number of events selected (the requirement of a lower number of correlated hits will make the number of events diverge) and the purity of my sample (tracks reconstructed with less than 6 hits are very likely due to background).

The output rate is much higher than in usual data acquisition because a larger number of hits is involved. At a background level of 70 kHz per OM the rate of L0 hits is around 63 MHz in the whole detector, when in the same conditions the L1 rate is about 0.2 MHz. On the other hand the random background rate is 2.3 kHz.

In order to check the effectiveness of the MX trigger I have produced a small Monte Carlo simulation of two different data samples originated by the same primary neutrinos: standard ANTARES data (L1 hits triggered with all online triggers, see Sec. for more details) and L0 hits triggered with both standard online triggers and MX trigger. An increase of the number of triggered events is expected especially at low energies using L0 data with MX trigger with respect to the standard ANTARES analysis. The results are shown in Fig. 3.10 where the data produced by the same Monte Carlo simulation are triggered using standard L1 trigger and L0 with MX.

The increase of the number of triggered events is evident, it reaches a factor 10 at energy around 100 GeV. Triggered events from L0 data contains more hits with respect to L1 data, this characteristic being crucial for low energetic events that lead to very few hits in the detector. On the other hand thanks to MX trigger the number of events selected at trigger level does not diverge because the MX trigger is designed in order to select events only in the direction set by the user (in my case the direction of the GRB).

Finally I can conclude that the use of L0 data with the direction trigger MX lead to an increase of the ANTARES sensitivity in the low energetic range between 50 GeV and 10^4 GeV where most of the neutrinos will be emitted according to GRB photospheric model (see Sec.1.4).

In the next chapter the ANTARES detector Monte Carlo simulation and the reconstruction algorithms are described. In particular a special reconstruction algorithm is presented,

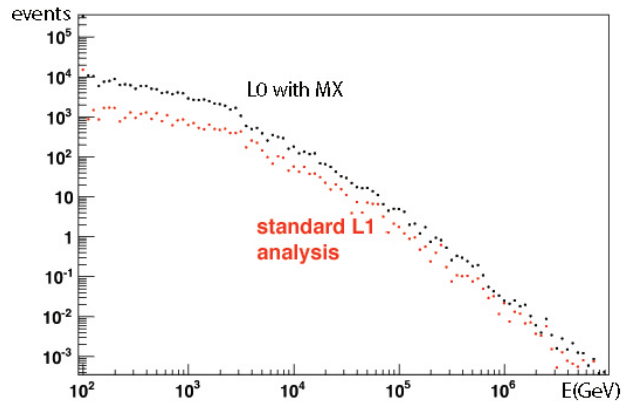


Figure 3.10: Number of triggered events using L1 hits triggered with all online triggers (red) and L0 hits trigger with standard online triggers and also MX trigger (black).

known as GridFit (see Sec. 4.6.2), which is optimized for energies between 50 GeV and 10^4 GeV. In my thesis this special reconstruction algorithm is used in order to obtain a further improvement of the ANTARES sensitivity at low energies.

Chapter 4

The detector Monte Carlo simulation and the reconstruction algorithms

4.1 Introduction

The prediction of the detector performance can be achieved with a Monte Carlo simulation. The ANTARES simulation tools take into account the physics processes occurring in the atmosphere, Earth and underground that can lead to the production of some detectable light in the detector, including the probability of each process to occur. Finally the detector response to the incoming light is simulated. The ANTARES collaboration uses the "Run by Run" approach in order to reproduce in realistic conditions the data taking. The input information (run setup, mean rates, position and orientation of OMs, time and charge calibrations, ARS threshold and run duration) are taken from the slow control data and plugged into the simulation.

4.2 The neutrino simulation

The neutrino flux is simulated with GENHEN [47], a Monte Carlo event generator that simulates high-energy neutrino interactions in the media surrounding the instrumented volume of the ANTARES neutrino telescope. The first step of the simulation is the generation of the neutrino position, direction and energy. Two different programs are used for deep inelastic scattering (DIS) and for resonant and quasi-elastic scattering (QES) in the medium surrounding the detector, respectively LEPTO [48] and RSQ [49]. The Cherenkov light is generated only inside a cylindrical volume, the so-called *can*, of which a schematic view is shown in Fig 4.1.

The simulated neutrino flux is derived from the formula

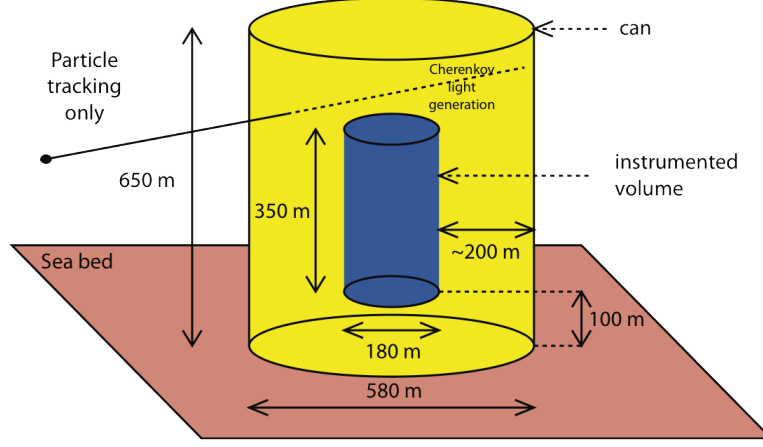


Figure 4.1: Schematic view of the can, surrounding the instrumented volume.

$$\frac{d\phi_\nu}{dE_\nu d\Omega dS dt} = \frac{N_{total}}{t_{gen} V_{gen} I_\theta I_E I_\Gamma} \frac{1}{\sigma(E_\nu) \rho N_A} \frac{1}{P_{Earth}(E_\nu, \theta_\nu)} \quad (4.1)$$

where

- N_{total} is the number of generated events
- Γ is the generation spectral index (typically $\Gamma=2$ for astrophysical neutrino and $\Gamma=3.5$ for atmospheric neutrino)
- t_{gen} (s) is the time duration of the simulation
- $V_{gen}(m^3)$ is the volume of the can (in water equivalent units)
- I_E is the energy phase space factor, defined as

$$I_E = \int_{E_{min}}^{E_{max}} E^{-\Gamma} dE$$

$$I_E = \begin{cases} \frac{E_{max}}{E_{min}} & \text{if } \Gamma = 1 \\ \frac{E_{max}^{1-\Gamma} - E_{min}^{1-\Gamma}}{1-\Gamma} & \text{otherwise} \end{cases}$$

- $I_\theta(\text{sr})=2\pi(\cos\theta_{max} - \cos\theta_{min})$ is the angular phase space factor corresponding to the specified range of $\cos\theta_\nu$ ($\cos\theta_{max}$ and $\cos\theta_{min}$ are the limits of the zenith bin of each event)

- $\sigma(E_\nu)(m^2)$ is the charged current neutrino interaction cross-section
- $\rho N_A(m^{-3})$ is the number of target nucleons per unit volume
- $P_{Earth}(E_\nu, \theta_\nu)$ is the probability of transmission through the Earth for a neutrino of given E_ν and θ_ν .

The flux can be renormalized according to the model that we want to simulate, this allows to simulate different neutrino spectra without generating every time all the processes. The event weight is defined as

$$w_{event} = \frac{d\Phi_\nu^{model}}{dE_\nu d\Omega dS dt} \left(\frac{d\Phi_\nu^{sim}}{dE_\nu d\Omega dS dt} \right)^{-1} \quad (4.2)$$

Thanks to w_{event} , a given simulation can be easily reweighted using any different spectrum simply rescaling the event weight according to the new spectrum. Three different weights are provided by default by the ANTARES simulation chain. First, the weight w_1 contains the projected area of the can onto the plane perpendicular to the neutrino direction. The weight w_2 is defined as

$$w_2 = \frac{N_{total}}{t_{gen}} \frac{d\Phi_\nu^{sim}}{dE_\nu d\Omega dS dt} \quad (4.3)$$

Finally w_3 is the global weight with units $years^{-1}$, in other world it corresponds to a “rate” per year

$$w_3 = w_2 \frac{d\Phi_\nu^{model}}{dE_\nu d\Omega dS dt} \quad (4.4)$$

All these weights can be used in the different Monte Carlo simulations in order to produce a neutrino flux with the desired neutrino spectrum.

4.3 The atmospheric muon simulation

Muons are the sole particle, obviously except neutrinos, that can reach the instrumented volume at a depth of 2475m below the sea level. They are part of the hadronic showers produced in the atmosphere by the interaction of cosmic rays. The ANTARES collaboration uses two different programs to simulate the atmospheric muon background.

CORSIKA [50] is used to simulate high energetic primary cosmic radiation (protons, α particles and heavier nuclei) interactions in the atmosphere and the propagation of the secondary particles to sea level (typically muons, pions and kaons). A valuable characteristic of CORSIKA is the possibility to compare at each step the results of the simulation with data from other experiments, this process provides an efficient way to control systematic errors. The MUSIC package [51] is used to propagate the muons from the sea level to the instrumented volume. This package simulates the interaction processes of muons with matter, i.e. bremsstrahlung, multiple scattering, ionization and pair production.

The alternative muon simulation chain used by the ANTARES collaboration is based on MUPAGE [52]. This simulation is faster because it is based on a predefined parameterization of muon flux measured by several experiments. MUPAGE generates events for a user specified data acquisition time, in such a way that no further weighting is needed. This simulation provides the best data/MC agreement.

4.4 Cherenkov light simulation

The emission of Cherenkov light by muon and electron propagation is simulated with KM3 and GEASIM programs [47]. KM3 simulates the propagation of muons using the MUSIC program and also the light and secondary particles emitted by these muons. GEASIM generates the hits at the OMs by means of a full GEANT simulation of photon production. However GEASIM considers the photon direction as a straight line, while KM3 considers also the photon scattering.

The KM3 program performs three different steps to simulate the Cherenkov light from muons and electromagnetic showers. First it uses a GEANT simulation of the Cherenkov light, generating the photons produced in the propagation of short muon track and electromagnetic showers. All photons (direct and scattered) are traced individually through water until absorption takes place and their position and time are recorded at each simulation step. When a photon reaches an optical module the detection probability is calculated taking into account absorption, scattering and the refractive index of the sea water. Positions and times of arrival of photons at each OM are stored and used to convert the hit probability into photo-electron numbers using Poisson statistics. The simulation includes also the present status of each optical module, the orientation of the PMT with respect to the track direction and the position of the line.

At this stage the number of photo-electrons produced in each PMT and their arrival time are calculated. These tables are then stored on disk for subsequent use by the reconstruction algorithms to derive the track direction of the simulated event.

4.5 Optical background simulation

The ANTARES neutrino telescope is located in an environment of high optical background produced by ^{40}K and bioluminescence at rates of about 100kHz per OM. The triggerEfficiency program [53] generates the background hits at the OMs according to the rates found in real raw data files. Then, it applies the same trigger criteria as for data to select candidate events in the Monte Carlo samples.

4.6 ANTARES reconstruction algorithm

The results of the previously described simulations, but also the data recorded by the detector, are analysed by different reconstruction algorithms in order to derive the parameters (time, direction, energy) of the events. In the next sections two different algorithms will be described. First, AaFit [54] is a program used widely inside the ANTARES collaboration, which is based on a maximisation likelihood method. The latter is a special reconstruction algorithm (known as GridFit [55]) that is optimized for low energy (below 10^3 GeV).

4.6.1 AaFit reconstruction algorithm

The first step of AaFit algorithm is a pre-selection of the hits, simulated or real detected hits. The pre-selection requires the satisfaction of a causality condition and the selected hits are merged within a time window of 300ns. A pre-Fit is applied on the selected hits assuming that the hits occur on points that are located on the muon track, which allows to derive analytically a starting point from the minimization of a χ^2 , although with a poor precision. This fit is used as starting point by the successive refined fitting procedure.

The next step is the M-estimator fit which improves the track parameter estimation of the previous fit and reduces the influence of hits detected by outlier optical modules. The M-estimator fit takes into account all the hits within 100 m around the track estimated by the prefit and within a time window ± 150 ns of the photon arrival times or a charge larger than 2.5 photo-electrons [54]. The optimal track parameters are derived maximizing the function

$$M = \sum_i \lambda \left(-2 \sqrt{1 + A_i \frac{(t_i - t_i^{th})^2}{2}} \right) - (1 - \lambda) f_{ang}(\alpha_i) \quad (4.5)$$

where A_i is the hit amplitude, f_{ang} is the PMT angular acceptance as a function of the incident photon angle α_i and λ is a parameter fixed to 0.05 according to the result of

a Monte Carlo based optimization. The final step of the reconstruction is a Maximum Likelihood (ML) calculation. The time residual $\delta t_i = t_i - t_i^{th}$ between the measured detection time of a photon and its expected time is calculated and the probability that the photon comes from a track is computed.

The best track is selected looking for the event direction for which the likelihood L takes maximum value. The likelihood is defined as

$$L = \prod_i P(t_i | t_i^{th}) \quad (4.6)$$

where $P(t_i | t_i^{th})$ is the statistical probability of measuring t_i with the expectation of t_i^{th} .

This probability is described as a Probability Density Function (PDF), which is a combination of a signal PDF and a background PDF. First the maximum likelihood fit includes only the signal PDF, but it takes into account the smearing on the hit times introduced by the transit time spread of the PMTs and the scattering of light in water. The signal PDF is shown in Fig 4.2

In this first likelihood computation only hits with residual $\delta t_i \in [-0.5R, R]$, where R is the root mean square of the residuals used in the M-estimator, are taken into account. Hits that are part of a coincidence or that have amplitude larger than 2.5 p.e. are also selected.

Four starting points for the M-estimator and ML fit are obtained by rotating the pre-fit track by 25° (the rotation is done around the track point which is the closest to the centre of gravity of the selected hits). Other four starting points are obtained changing the starting point of the track by ± 50 m in the $\vec{d} \times \vec{z}$ direction, where \vec{d} is the track direction. Obviously the track with the best likelihood is stored.

Finally a PDF with time residual of ± 250 ns (in order to add background hits), local coincidences and hits with amplitude larger than 2.5 photo-electrons is used for the final fit (Fig 4.3).

The final track has two different quality parameters. The first is

$$\Lambda = \frac{\log L}{N_{dof}} + 0.1(N_{comp} - 1) \quad (4.7)$$

where $N_{dof} = N_{hits} - N_{parameters}$ is the number of degrees of freedom and N_{comp} is the number of trials.

The second quality parameter is the angular error on the reconstructed track β , defined as

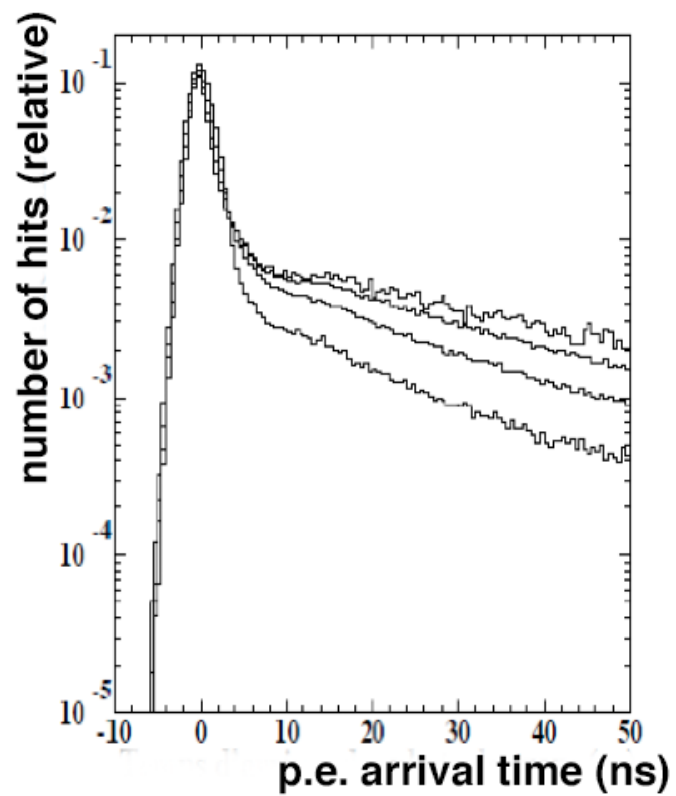


Figure 4.2: Distributions of the time residuals corresponding to four different muon energies, from the top to the bottom: 250, 50, 10 and 2 TeV.

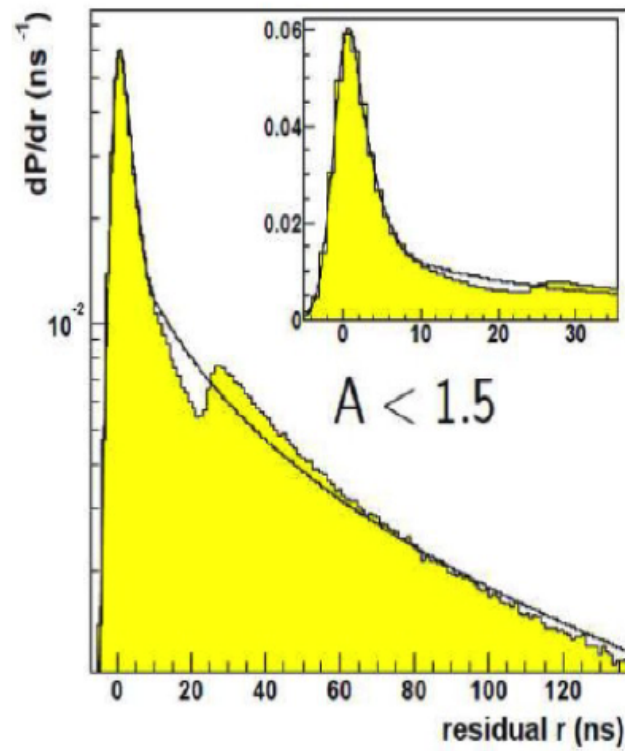


Figure 4.3: Full PDF used in the final ML fit step for hit amplitudes < 1.5 p.e. In yellow is the histogram obtained by the Monte Carlo simulation, the solid line is the parameterization used by the likelihood fit. The second bump in the histogram is due to the ARS chip integration of the analogue signal from the PMT over a time window of 25 ns.

$$\beta = \sqrt{\sigma_\theta^2 + \sin^2\theta\sigma_\phi^2} \quad (4.8)$$

where σ_θ and σ_ϕ are respectively the error estimates of the track's zenith and azimuth angles.

4.6.2 GridFit reconstruction algorithm

GridFit is a reconstruction algorithm optimised for an efficient reconstruction of low energetic neutrinos [55]. In the hit selection all L0-hits are taken into account and clusters of hits or high-amplitude hits are selected if they fulfill a space-time correlation condition. Three different hits selections are performed for both the clusters and the high-amplitude hits.

For each hit, all other hits within a given time (δt_{max}) and distance ($dist_{max}$) window are selected. If the number of these hits is larger than a chosen size, the directions of the connecting lines in the time-height plane are calculated for all other hits, as well as the root mean square (RMS) of their distribution. If the RMS is larger than a given maximum (RMS_{max}), the hit with the largest deviation from the mean value is removed. This is iterated until the RMS falls below the prescribed maximum, or the number of hits is lower than the prescribed cluster size ($nhit_{min}$). In the first case, all hits belonging to the cluster are selected, in the second case, all hits of the cluster are discarded. Anyway they may still be included in the selection when they themselves or another hit is examined. The parameter requirements chosen for the three different selections are listed in Tab 4.1.

	$nhit_{min}$	RMS_{max}	$dist_{max}$	δt_{max}	amp_{min}
Selection 1	3	4°	45m	150 ns	1.0 p.e.
Selection 2	2	-	5 m	50 ns	2.0 p.e.
Selection 3	4	4°	75 m	200 ns	1.5 p.e.

Table 4.1: The parameter requirements of the three different hit selections.

A hit is selected if it is in at least two out of three cluster hit selections or in a cluster hit selection and in the corresponding high-amplitude hit selection. In any case all the hits with a charge larger than 2.5 photo-electrons are selected, even if they don't fulfill the previous conditions. These selections will include many more hits with respect to AaFit, so a track precut has been developed in order to reduce the number of hits considered by the

final reconstruction procedure. This pre-cut essentially discriminates between atmospheric muon-like events from upgoing neutrinos topology with the algorithm described below. The whole phase space is scanned by generating 500 track hypotheses, which are isotropically distributed over the sky.

Fig 4.4 shows a Hammer projection of the full 4π sky for a single event where for each direction the number of hits clustered in that direction is represented in color scale for an atmospheric muon.

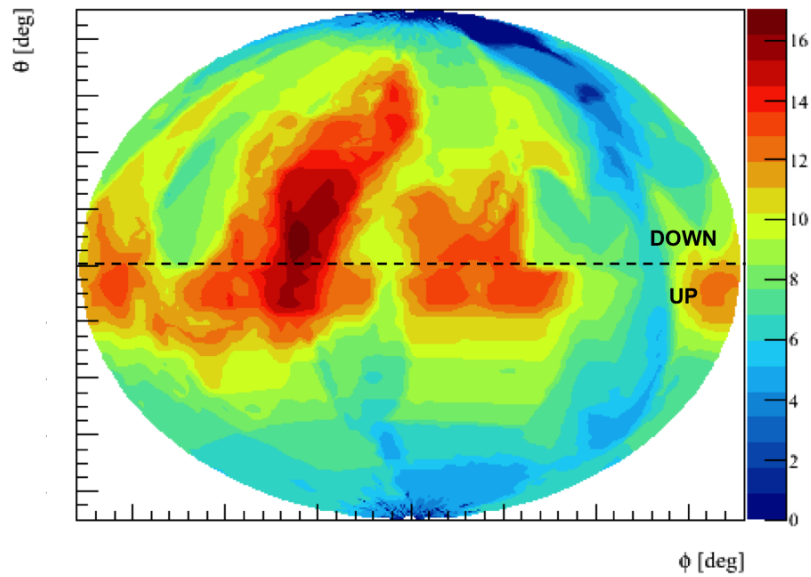


Figure 4.4: Hammer projection of the full 4π sky for an atmospheric muon (zenith angle $=80^\circ$), with for each direction the number of hits clustered in that direction.

The top half of the plot is the down-going part: since atmospheric muons are down-going they should be reconstructed here. The bottom half is called the up-going part: since neutrinos are up-going and they should be reconstructed there (Fig 4.5).

This information can be used by defining the Ratio parameter as the total number of hits in the up-going part N_{up} divided by the total number of hits in the down-going part N_{down}

$$Ratio = \frac{\sum N_{up}}{\sum N_{down}} \quad (4.9)$$

The Ratio distributions of atmospheric muons and neutrinos are shown respectively in Fig. 4.6 and Fig. 4.7.

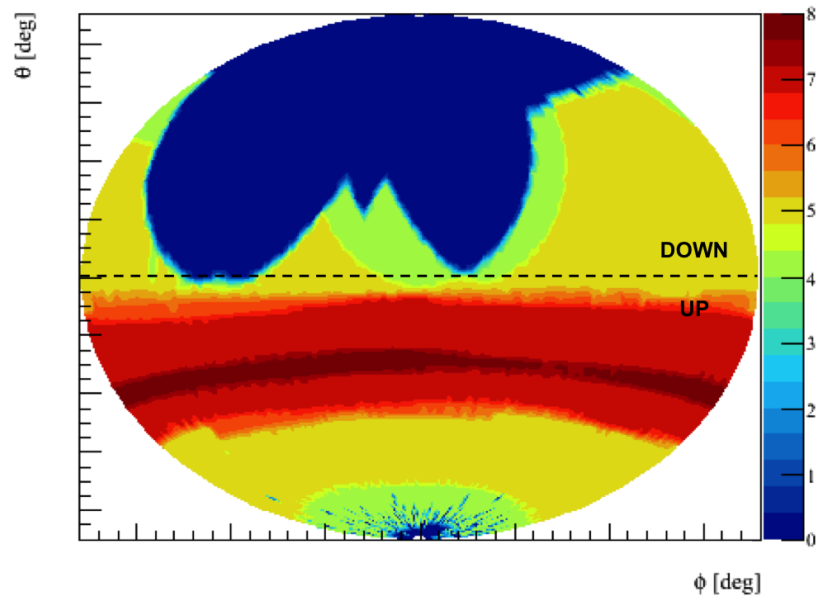


Figure 4.5: Hammer projection of the full 4π sky for a low energetic neutrino (zenith angle = 130°), with for each direction the number of hits clustered in that direction.

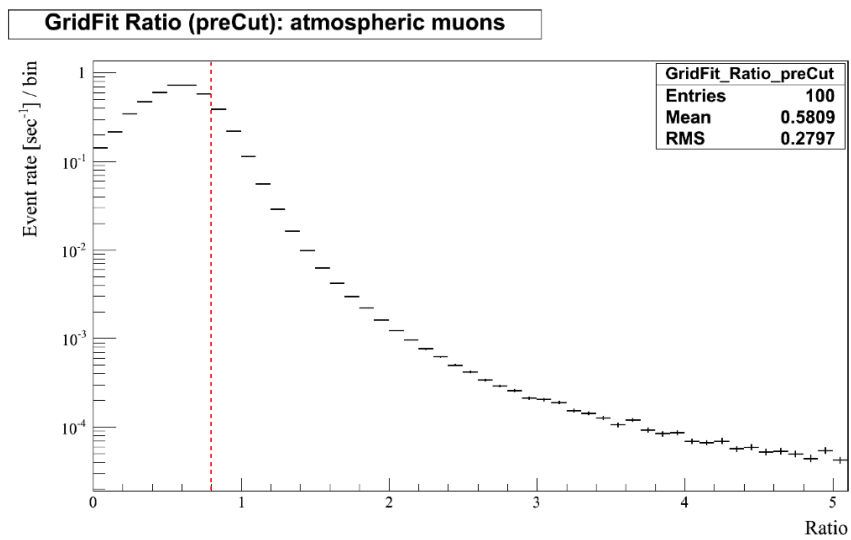


Figure 4.6: Distribution of the Ratio parameter for atmospheric muons, the red line indicates the cut value (60 kHz background) .

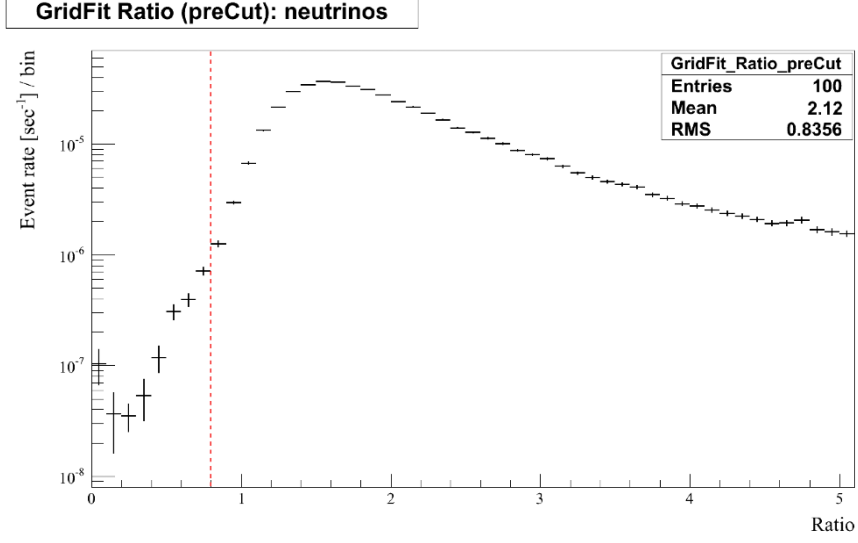


Figure 4.7: Distribution of the Ratio parameter for neutrinos, the red line indicates the cut value (60 kHz background).

The peak of the distribution is at about 0.6 for atmospheric muons and at about 1.6 for neutrinos, so the Ratio parameter can be used to discriminate efficiently between down-going muons and up-going neutrinos. In order to reduce the number of hits due to atmospheric muons, only events with a Ratio parameter of at least 0.8 are kept. In this way 81.3% of the atmospheric muons are filtered out and only 0.32% of the neutrinos.

After the cut on the Ratio parameter, the whole phase space is scanned again by generating this time 5000 track hypotheses. A quality parameter of the track is defined as

$$Q = n_{hits} - w \frac{\chi^2}{N_{dof}} \quad (4.10)$$

where $\chi^2 = \frac{t_{residual}^2}{\sigma^2}$ with time resolution $\sigma = 2$ ns, $N_{dof} = n_{hits} - 3$ and w is a weighting factor which can be set by the user. The parameter w is optimized through Monte Carlo simulations in order to maximize the algorithm capability to distinguish between tracks with different reconstruction quality. The 9 directions with the highest value of Q are selected. In any case are taken into account only directions that have at least 80% of the total number of hits compatible with the selected direction. It has been found that the number of hits compatible with the MC direction is typically more than the 95% of the total number of hits considered at this stage of the reconstruction. Finally an M-estimator

fit is performed to improve the angular resolution and in the final fit the same PDF of AaFit will be used.

The reconstructed track has a quality parameter defined as

$$X = n_{hitsfinalfit} - 1.1rLogL \quad (4.11)$$

where $n_{hitsfinalfit}$ is the number of hits that are considered in the final stage of the reconstruction (the PDF fit) and $rLogL$ is the reduced log-likelihood (i.e. the log-likelihood divided by the number of degrees of freedom). The factor 1.1 has been found through Monte Carlo optimization.

GridFit provides also an angular error estimation: the width of the minimum (WOM) in the zenith/azimuth landscape, in other words it determines the ellipse along which the difference of the log-likelihood with respect to the found minimum of the log-likelihood is 1/2.

4.6.3 AaFit and GridFit performance comparison

I compared the GridFit and AaFit performances using an opportune Monte Carlo simulation. For a fair comparison, the cuts of both strategies are tuned in such a way as to obtain the same purity.

A simulation of a run of a ANTARES L1 data run has been performed: muon and atmospheric neutrino background and neutrino signal with a GRB-like spectrum (E^{-2} spectrum). In order to maximize the signal sensibility for both algorithms an optimization of the quality cut parameters has been performed maximizing the model rejection factor (MRF) [56]. The quality cuts predicted by the MRF optimization are $X > 4.9$ (Eq. 4.6.2) in the case of GridFit and $\Lambda > -5.3$ (Eq. 4.6.1) for AaFit.

Selecting all the signal events that satisfy the quality cuts, I can compare the performance of the two reconstruction algorithms. In Fig 4.8 GridFit/AaFit ratio is shown as a function of the neutrino energy. All results are normalized to the standard ANTARES analysis (L1 data reconstructed with AaFit).

GridFit starts to perform significantly better than AaFit at 10^4 GeV and the ratio increase up to 1.3 at 100 GeV. At energies between 10^4 and 10^6 GeV GridFit performance is comparable with the AaFit one and GridFit is more efficient at very high energies (above 10^6 GeV). This is a known characteristic of GridFit, but it is not interesting in this analysis which is focused on the low energy range.

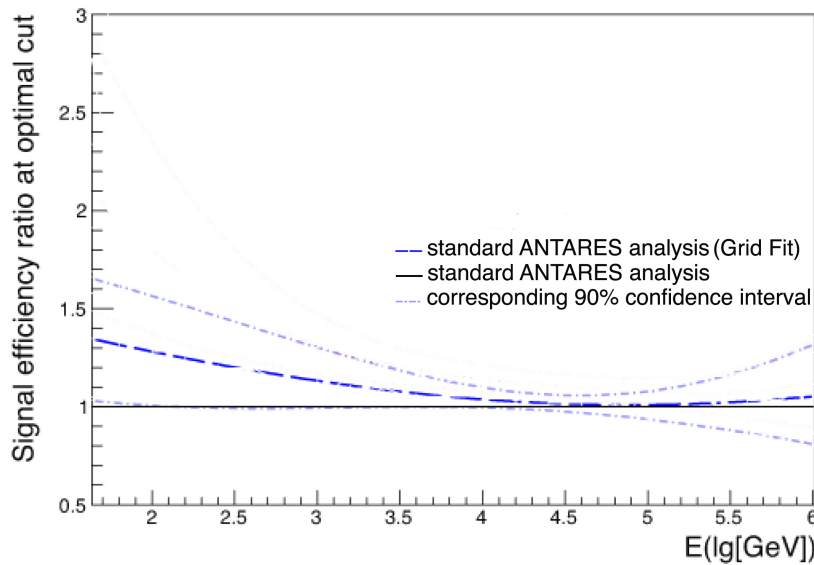


Figure 4.8: Signal efficiency ratio at optimal cut. Blue: standard data (L1) reconstructed with GridFit. Pale blue: corresponding 90% confidence interval. All results are normalized to the standard ANTARES analysis (L1 reconstructed with AaFit).

So far I compared L1 data reconstructed with GridFit and L1 data reconstructed with AaFit, however in my analysis I will use the special data sample of L0 data recorded in correspondence of a GRB (Sec. 3.7) and a special directional trigger (Sec. 3.8). In principle I expect a further improvement of the sensitivity at low energies using L0 data instead of L1 data.

I produced a simulation of a L0 data sample in order to verify this hypothesis. This data have been triggered offline using the special directional trigger MX and reconstructed with GridFit. In Fig 4.9 the sensitivity of L0 data reconstructed with GridFit is compared to L1 data reconstructed with GridFit and AaFit.

As expected the use of L0 data and the directional trigger yields to further improvements with respect to the standard ANTARES analysis. The improvement is quite small at high energies, but it is more consistent in the range of interest of this analysis (50 GeV-10 TeV). The ratio increases up to 2 at 50 GeV.

In conclusion GridFit is a reconstruction chain with high efficiency for low energetic neutrinos. Furthermore the use of L0 data and directional trigger MX leads to a greater improvement between 50 GeV and 10 TeV. The analysis proposed in this thesis almost doubles the sensitivity of ANTARES in the lower energetic range with respect to the stan-

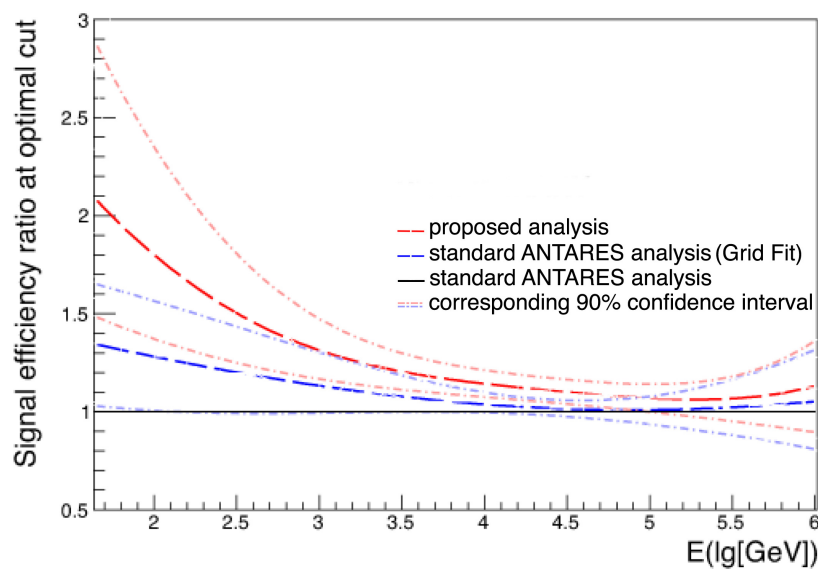


Figure 4.9: Signal efficiency ratio at optimal cut between the proposed analysis and the standard ANTARES analysis. Red: L0 data filtered with the directional trigger and reconstructed with GridFit. Blue: standard data (L1) reconstructed with GridFit. Pale blue and red: corresponding 90% confidence interval. All results are normalized to the standard ANTARES analysis (L1 reconstructed with AaFit)

standard analysis typically applied by the collaboration in the previous GRB analysis [57].

Chapter 5

The calibration of the detector

5.1 Introduction

The calibration of the detector is crucial for the physics research of the ANTARES detector. The precision of track and energy reconstruction is strongly dependent on the precision of time, position and charge measurements.

Concerning the time calibration of the optical modules we can distinguish between absolute and relative time calibrations. The first is important because it allows the link between detected signals and celestial transient sources, the latter is used to measure the offset between OMs. The timing accuracy reaches the nanosecond level, thus permitting unprecedented angular resolution accuracy. A further improvement of the time measure would not enhance the ANTARES performance, as the dimension of the optical modules is around 20 cm which corresponds roughly to the length travelled by the light in 1 ns.

The position calibration of each OM is obviously relevant to reach an adequate pointing accuracy.

Finally the accuracy on charge calibration permits a fair estimation of the neutrino energy, allowing discrimination between cosmic and atmospheric neutrinos.

In the next paragraphs the different calibrations are described in detail. In particular I focus on two calibration service works I have performed for the ANTARES collaboration: the study of the optical module performances using the ^{40}K measurement (Sec. 5.4) and the detection of the Moon shadow (Sec. 5.6).

5.2 The charge calibration

The charge calibration relies on the measurement of the corresponding photo-electron peak and the pedestal value of the Amplitude-to-Voltage Converter (AVC). The first step is

performed before line immersion. The discriminator threshold is estimated by computing efficiency curves at different test voltages in order to obtain the response function of the AVC in such a way that the suitable voltage can be chosen. After line immersion these thresholds are measured again by using the one photo-electron pulses produced by the ^{40}K decays in the sea water.

The charge measurements in the Analogue Ring Sampler (ARS) are affected by a ‘‘cross-talk’’ effect due to the influence of the Time-to-Voltage Converter (TVC) ramp values on the analogue memory of the AVC during the ARS signal digitization.

Another issue to be considered during the charge calibration is the Differential Non-Linearities (DNL) that are seen as unevenly filled channels in the TVC/AVC distributions. In fact ARS imperfections can lead to non-linearities when the analogue signal is converted into a output binary signal. Anyway this phenomenon is a second order correction in the charge calibration.

After the calibration, all hits that satisfy the threshold condition are parameterized in charge distribution as

$$\frac{dN}{dx} = Ae^{\alpha(x-x_{th})} + Be^{-\frac{(x-x_{pe})^2}{2\sigma^2}} \quad (5.1)$$

where x is the charge, x_{th} is the charge threshold and x_{pe} is the one photo-electron peak charge. The first term corresponds to the PMT dark current, the second corresponds to the one photo-electron peak distribution. The parameters α and σ are derived fitting the calibration charge distribution as shown in Fig 5.2, in particular σ is the standard deviation of the on photo-electron distribution.

According to the optical activity signals the charge distribution is expected to be peaked at 1 photo-electron. This expectation is confirmed by the measures presented in Fig 5.1 and Fig 5.2.

The linear response integrator-ADC (Fig 5.1 shows clearly the linear behaviour of the ADC) allows the conversion of ADC counts into photo-electron units:

$$CE_{pe} = \frac{AVC - AVC_0}{AVC_1 - AVC_0} = \quad (5.2)$$

where AVC_0 and AVC_1 are the values corresponding to the pedestal and the p.e. peaks respectively.

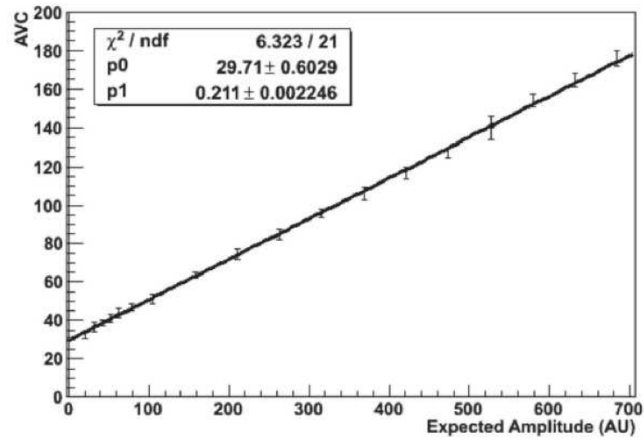


Figure 5.1: Measurement of the AVC linearity by estimations of the input (expected) amplitude, p0 and p1 are the coefficients of the linear fit.

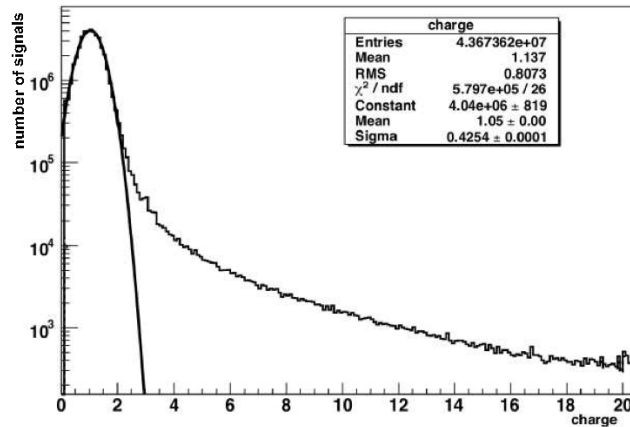


Figure 5.2: Calibrated charge distribution for all PMTs in the detector (charge expressed in p.e.). The fit parameters in the box refer to the gaussian fit of the one photo-electron peak (second term of Eq. 5.2)

5.3 The time calibration

Two different time calibrations are performed by ANTARES collaboration.

The first is performed before the installation of the lines in the sea. These tests are performed in a dark-room using a laser and a clock system. The laser is used to flash a group of OMs to measure the time offset between the modules. The time delay from the SCM to each LCM is measured with the clock system calibration, so the contribution of the cable linking the LCM to the OM, the transit time of the PMTs and the front-end electronics time delay are measured. An example of the measured time offset is shown in Fig 5.3.

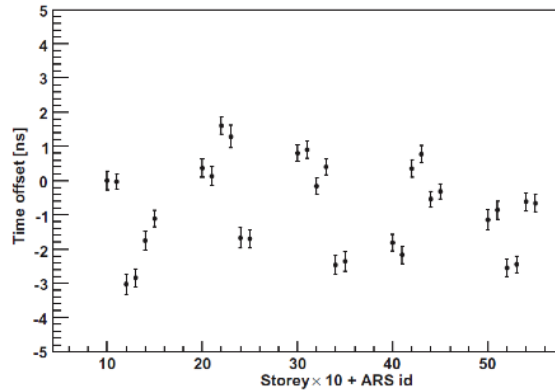


Figure 5.3: Time offsets measured for the 30 ARS of a given sector.

Fig 5.3 presents a small spread (lower than 3 ns). It is due to the different internal cablings of the OMs to the storey electronics and also to the spread in the transit time of the different PMTs. The values of these measurements were used as initial values for the time offset after the line deployment.

The other time calibration is performed regularly to measure the absolute time of the signals. The absolute time calibration allows assigning a universal time to each event. This is performed by interfacing the shore station master clock to a card receiving the Global Positioning System (GPS) time with an accuracy of about 100 ms with respect to the Universal Time Coordinated (UTC).

The time of PMT hits is measured by a self-calibrated 20 MHz master clock system generated on-shore. The independent time offsets of each specific detection unit are measured in situ using the optical beacons (OBs). The difference between the signal time recorded in the OM and the emission time of the corresponding LED flash is considered taking into

account also the time offsets measured on-shore. Then the nominal travel of the light from the OB to the OM is subtracted, the time distribution of the “time residuals” should be centred at zero (Fig 5.4).

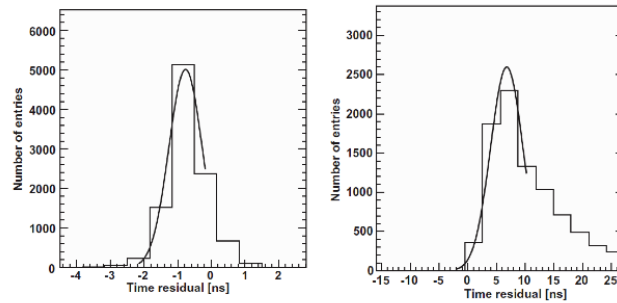


Figure 5.4: Signal time residuals of two OMs. Left: two storeys 30 m above the OB. Right: two storeys 105 m above the OB. The gaussian fit provides an estimation of the time residual for these two couples of OMs.

The tail seen in Fig 5.4-right corresponds to the effect of light scattering in water.

The laser OB is also used to compute relative time offsets between lines since its light can reach all the detector lines.

The time calibration as well as an estimation of the PMT efficiency could be performed exploiting the ^{40}K present in the sea water by using the Cherenkov light induced by the electron released in the β -decay and e-capture process [58]. If the ^{40}K decays some few meters from the storey, a coincidence signal is expected to be seen in a couple of OMs in the same storey. Incorrect time calibration would be seen as an offset in the time coincidence distribution, there would be a displacement from the zero position of the peak due to single ^{40}K decays detected in coincidence by two OMs.

The measure of ^{40}K coincidences can also be used for an estimation of the optical module efficiency as described in the next section (Sec. 5.4).

5.4 Study of the optical module performances with ^{40}K data

I have performed a study in order to derive the efficiency loss of the optical modules from the evolution of the measured ^{40}K coincidence rate.

At the beginning of ANTARES life a gain reduction has been observed, this impacts the collection efficiency but it can be partially recovered by adapting the detector thresholds. However during 2013 a more consistent efficiency loss has been observed.

It is expected that the performance of the optical modules should degrade due to the ageing or to the deposit of biofouling on the glass window of the modules. If this phenomenon occurs a reduction of the coincidence rate of ^{40}K is expected. An example of the time dependence of the coincidence rate as a function of the time is shown in Fig 5.5.

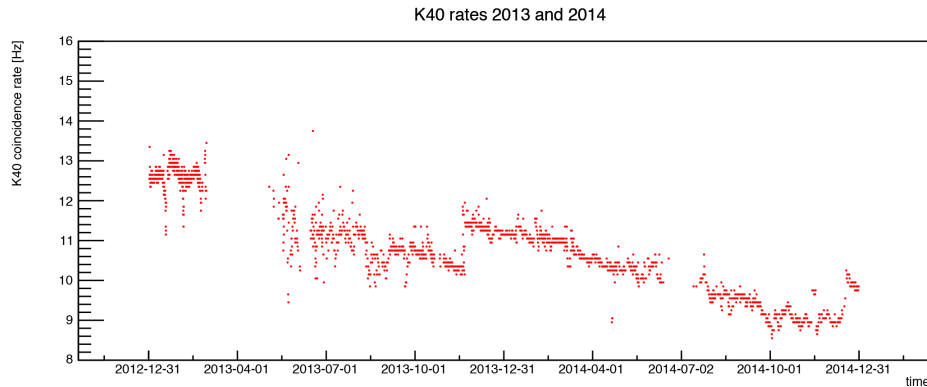


Figure 5.5: Evolution of the average rate of ^{40}K coincidences with time (2013-2014).

The reduction of the ^{40}K coincidence rate is noticeable, whereas the steps in the distribution are due to the changing of the detector thresholds.

It can be shown by Monte Carlo simulations that the coincidence rate is proportional to the sensitivity of the optical modules [59]:

$$R^{40K} \propto s_1 \cdot s_2 \quad (5.3)$$

where R^{40K} is the ^{40}K coincidence rate and s_1 and s_2 are the sensitivities of the two OMs in coincidence (arbitrary units). The optical modules sensitivity is proportional to its collection efficiency (CE), so Eq. 5.3 can be rewritten as

$$R^{40K} \propto CE_1 \cdot CE_2 \quad (5.4)$$

where CE_1/CE_2 are the collection efficiencies of the two OMs.

I assumed that the phenomenon of degradation of the optical modules is similar in the whole detector, so approximated $CE_1 = CE_2 = CE$. Finally Eq.5.4 is simplified as

$$R^{40K} \propto (CE)^2 \quad (5.5)$$

Eq.5.5 provided a way to estimate the reduction of the optical module collection efficiency according to the diminution of the ^{40}K coincidence rate.

I verified the assumption of Eq.5.5 with a dedicated Monte Carlo simulation. I have produced several simulations where I assumed different reductions of the collection efficiency. I did not make any assumption about the process that leads to the reduction of the optical module sensitivity (ageing, biofouling, etc.), thus the probability that a photon is detected by an optical module is simply reduced by a certain factor.

The number of reconstructed atmospheric muons for different collection efficiency reductions is estimated through Monte Carlo simulations (Fig 5.6). The events are reconstructed with AaFit (Sec. 4.6.1) with $\Lambda > -5.7$ as selection criterion (this quality cut is typically used in atmospheric muon analysis [60]).

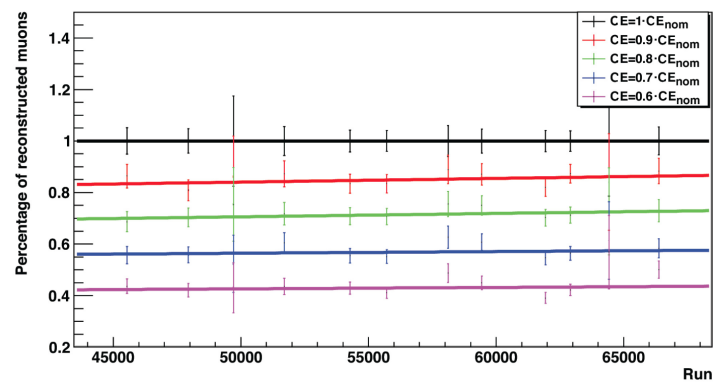


Figure 5.6: Number of reconstructed muons for different collection efficiency reductions. Results are normalized to the simulation with nominal collection efficiency ($CE = CE_{nom}$). The presented runs correspond to the period between January 2010 and May 2012. The different linear fit show angular coefficients compatible with zero (typically $10^{-6} \pm 10^{-5}$).

The reduction of the number of reconstructed events is constant in time and does not depend on the environmental condition, so I can derive a relationship between the reduction of collection efficiency and the diminution of reconstructed muons (Fig. 5.7). The relationship is clearly linear: the slope is 1.42 ± 0.03 and the intercept is -0.42 ± 0.03 .

This relationship is very useful to estimate the number of reconstructed muons in a run without reprocessing the full Monte Carlo chain each time I want to simulate a different collection efficiency reduction.

In particular I focused on the data sample of 2013 and I simulated all the corresponding runs assuming a decrease of collection efficiency as predicted by the reduction of the ^{40}K

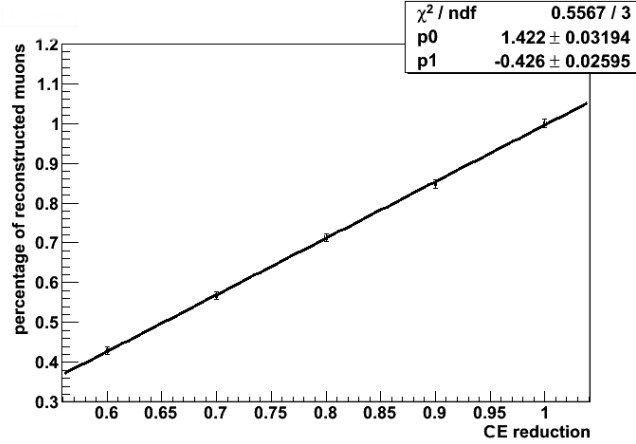


Figure 5.7: Relationship between the reduction of collection efficiency and the diminution of reconstructed muons. Results are normalized to the simulation with nominal collection efficiency ($CE = CE_{nom}$).

coincidence rate (Fig 5.5). For the previous estimation of the relationship between the reduction of collection efficiency and the diminution of reconstructed muons the period between January 2010 and May 2012 in order to have a long statistic sample and do not have any bias on the study of the year 2013.

First I fit the linear decrease of the ^{40}K rate in 2013 (Fig. 5.8)

The collection efficiency reduction can be evaluated thanks to Eq. 5.5 and the previous fit:

$$CE_{40K} = k \cdot \sqrt{R_{40K}} = k \cdot \sqrt{p_0 \cdot Run + p_1} \quad (5.6)$$

where R_{40K} is the ^{40}K coincidence rate, p_0 and p_1 are the parameters of the ^{40}K rate fit and k is a normalization constant. I choose k in order to normalize at 1 the collection efficiency CE at the beginning of 2013.

The reduction predicted by my Monte Carlo simulation is shown in Fig. 5.9

I compare the results of my simulation, where the collection efficiency is reduced according to Eq. 5.6, with the data sample of 2013. My simulation predicts a reduction of atmospheric muon sensitivity during 2013 of 19%, whereas data analysis showed a decrease around 20% (assuming the same selection criterion: $\Lambda > -5.7$); this agreement seems to validate my estimation of the collection efficiency reduction. Obviously this rate reduction is not present in the standard Run by Run Monte Carlo simulation where the nominal collection efficiency is assumed.

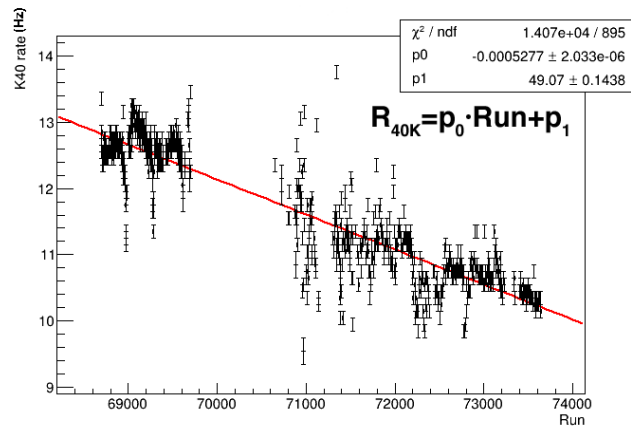


Figure 5.8: Fit of the evolution of the average rate of ^{40}K coincidences during 2013. The period with no data corresponds to the spring season when the detector was turned off because of bioluminescence, after this period the detector is operative again but presents some fluctuation due to bioluminescence.

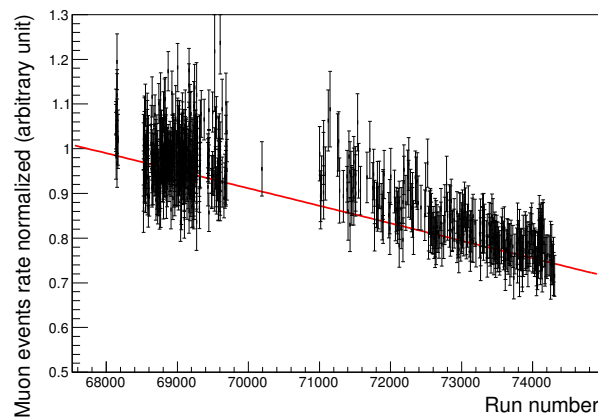


Figure 5.9: Reconstructed atmospheric muon events rate according to my simulation with collection efficiency reduced (2013). The rate at the beginning of 2013 is normalized to 1. Results of the linear fit: slope $-3.91 \cdot 10^{-5} \pm 8 \cdot 10^{-7}$, intercept 3.65 ± 0.06

It is important to underline that this sensitivity reduction is evaluated using atmospheric muons: they are really numerous and they have been a very good probe to test my collection efficiency reduction hypothesis. However in physics analyses we are interested in upgoing muons produced by neutrinos and much more strict selection criterion is applied: $\Lambda > -5.2$ [31]. In fact if I apply my collection efficiency correction on a simulated sample of cosmic neutrino events, the predicted sensitivity reduction during 2013 is really small (below 2%) if $\Lambda > -5.2$ cut is applied (Fig. 5.10).

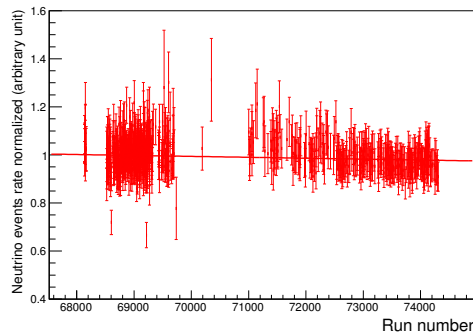


Figure 5.10: Reconstructed neutrino events rate according to my simulation with reduced collection efficiency (the reduction is derived from Eq. 5.6). The rate at the beginning of 2013 is normalized to 1. The presented runs correspond to the 2013 data set.

The really small reduction is due to the strict cut: tracks reconstructed with a very good quality parameter would be reconstructed even if the telescope detects a few less hits due to the reduction of collection efficiency. In other words the reduction of the collection efficiency does not strongly affect the physics analyses of ANTARES.

This analysis shows how the detector is deeply under control of the ANTARES collaboration, which has the necessary tools to understand the telescope behaviour and to correct it correspondingly to the Monte Carlo simulations. The ANTARES collaboration is investigating this issue and it is considering to apply my correction on the OM collection efficiency in the next update of the official Run by Run Monte Carlo simulation.

5.5 The position calibration

Due to the flexible nature of the detector, water currents can change the position of the optical modules, especially on top storeys. The knowledge of the detector components position is crucial for an accurate event reconstruction.

The High Frequency Long Baseline (HFLBL) acoustic system is used to monitor the

positions of five hydrophones (placed on storey 1, 8, 14, 20 and 25) along each line. A transmitter-receiver, installed at the bottom of each line, sends a high frequency acoustic signals (40-60 kHz). The distances are calculated measuring the times of the acoustic waves detection. This information is used to triangulate the position of each receiver with respect to the emitters at the anchor of each line.

The orientation and the inclination of each storey is evaluated using a system of compasses and tiltmeters. Combining the measures of hydrophones, compasses and tiltmeters, the shape of each line is reconstructed by performing a global fit. The water current flow and the sound velocity in sea water are measured using acoustic Doppler current profilers (ADCP) for the water current flow, conductivity-temperature-depth (CTD) sensors to monitor the temperature and salinity of the water and sound velocimeters to monitor the sound velocity in sea water. This information is taken into account in the global fit of the detector shape. The detector reconstruction performance is quite good, the relative position of each optical module is monitored with an accuracy better than 20 cm [61].

The horizontal movement of a line with respect to the reference position is illustrated in Fig 5.11.

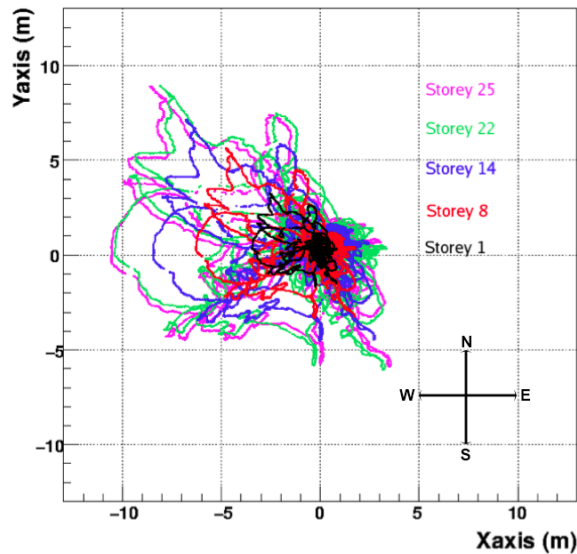


Figure 5.11: Horizontal movements of the hydrophones on Line 11 with respect to the reference position (0,0) in six months. The East-West tendency of the Line heading is due to the Ligurian current at the detector site. The top storeys of the line experience larger amounts of displacement due to the water current [62].

The absolute position of each anchored detector component is calculated with an accuracy

of about 1 m and an accuracy of 1° and 0.1° degrees in horizontal and vertical pointing by acoustic triangulation from a surface ship equipped with differential GPS. In addition to using the acoustic system to calibrate the pointing of ANTARES, an independent measurement has been implemented to verify these results: the Moon shadow effect.

5.6 The Moon shadow measurement

The Moon shadow measurement is one important topic that I have addressed for the ANTARES collaboration. In this measurement the Moon absorption of the cosmic rays is exploited to evidence a deficit in the event density of the atmospheric muon flux corresponding to the direction of the Moon disk in the ANTARES detector. The detection of this deficit - the so-called Moon shadow - and its position in the sky provides the measurements of the detector angular resolution for atmospheric down-going muons and of the detector absolute pointing capability.

This effect has been already exploited in many detectors like CYGNUS [64], TIBET [65], CASA [66], MACRO [67], SOUDAN [68], ARGO [69] and IceCube [70] to test their pointing performance. In the point-like source search good angular resolution and absolute pointing capability are required for efficient rejection of the background and source identification. These detector figures of merit depend on the relative delays among the optical sensors, but also on the instantaneous shape and absolute orientation of the detector lines.

5.6.1 Monte Carlo simulation of the Moon shadow

The simulation of the atmospheric muon events was performed with the MUPAGE code [52]. The code simulates both single and bundle muon events.

The geo-magnetic deflection is not taken into account in MUPAGE. Anyway, a detailed study of this effect has been previously conducted by the collaboration through a detailed simulation with the Corsika code [50]. This study showed that the geo-magnetic effect of the muons is negligible at detector level because only low energy muons that are absorbed before reaching the detector are strongly deflected [71]. For this reason I neglected the geo-magnetic effect in this analysis [71].

Muon events coming from an angular distance greater than 10° from the Moon centre do not affect the simulation result of the shadow and therefore they are not simulated. This choice reduces the CPU time consumption by a factor ~ 100 , allowing the simulation of long periods of data-taking required for this study.

The simulation includes the generation of Cherenkov light emitted by the muon tracks, its propagation up to the PMTs, the optical background caused by bioluminescence and the radioactive isotopes and the detector response.

Finally the hits detected by the PMTs are used to reconstruct the atmospheric muon tracks with the standard ANTARES algorithm used for data. The used reconstruction algorithm is AaFit (Sec. 4.6.1), a robust track fitting procedure based on a maximisation likelihood method [54].

The Moon shadow effect is simulated rejecting the muons generated within the Moon disk, having an angular radius $R_{Moon} = 0.259^\circ$. In this analysis two different Monte Carlo simulation sets were performed: one considering the shadowing effect of the Moon and the other without this effect. Each simulation corresponds to the live time of 2080 days considered in this data analysis (years 2007-2012). The detector simulations were performed on the basis of a run-by-run simulation [72], to take into account the experimental conditions of each data run, such as the status of each PMT, the detector configuration, the actual environmental conditions and optical background.

Previous data analysis conducted by the ANTARES Collaboration [73] put in evidence that the Monte Carlo simulation event rate is about 6% lower than the data rate. The same discrepancy has been observed also in this analysis in the region of the sky where the shadowing effect is expected to be negligible. This effect can be due to the systematic uncertainties of the primary muon flux and of the detector. The Monte Carlo simulations were therefore renormalized in order to reproduce the muon data rate.

The expected reduction of the OMs efficiency shown in Sec. 5.4 is not taken into account because the phenomenon is negligible in the period considered in the Moon shadow measurement.

The reconstructed events were analysed in order to optimise the selection and the data analysis itself as described in the next section.

5.6.2 Detection of the Moon shadow

In order to measure the shadowing effect the region around the Moon centre is divided in concentric rings with increasing radius. The event density of each ring is computed as the number of events detected in that sector over the surface of the ring. Event tracks reconstructed as down-going and detected when the Moon is above the Horizon are selected. The size of each bin is 0.2° . This size allows an appropriate investigation of the Moon shadow with sufficient statistics in each bin.

A test statistic function t is defined to evaluate the statistical significance of the Moon

shadow effect:

$$t = \sum_{rings} \frac{(n_m - n_{exp, NO\ Moon})^2}{n_{exp, NO\ Moon}} - \frac{(n_m - n_{exp, Moon})^2}{n_{exp, Moon}}, \quad (5.7)$$

where the sum is over all the rings around the Moon centre; n_m is the number of events detected in a ring, $n_{exp, Moon}$ is the expected number of events in ‘‘Moon shadow’’ hypothesis and $n_{exp, NO\ Moon}$ is the expected number of events in ‘‘no Moon shadow’’ hypothesis.

Using the two Monte Carlo simulations mentioned above, 10^6 toy experiments were generated in order to obtain the distribution of the variable t in the case of Moon shadow effect or vice versa.

Exploiting the statistical method previously described, the significance of the Moon shadow observation was estimated optimising the event selection. The track selection criterion used in my analysis, consists of the application of quality cuts on the log-likelihood per degree of freedom $\Lambda < \Lambda_{cut}$ and on the angular error of the direction $\beta < \beta_{cut}$ (see Eq. 4.6.1 and Eq. 4.6.1). I found the maximisation of the significance for $\Lambda_{cut} = -5.9$ and $\beta_{cut} = 0.8$ as shown in Fig. 5.12.

The corresponding test function distributions are plotted in Fig. 5.13. The shaded area gives the fraction of the toy experiments where the Moon shadow hypothesis will be correctly identified as evidence of the shadowing effect; this fraction is fixed to 50%. The value of $t = 6.15$ corresponding to this fraction of the ‘‘Moon shadow’’ toy experiments is the decision boundary of the test statistic. The orange area corresponds to the fraction of ‘‘No Moon shadow’’ toy experiments that will be wrongly identified as evidence of shadowing effect. In other words, this area quantifies the median significance of the Moon shadow discovery for experiments with $t = 6.15$. The median significance is here 2.9σ .

The same quality cuts $\Lambda_{cut} = -5.9$ and $\beta_{cut} = 0.8$ were applied to the data set. The value of test statistic function defined in Eq. 5.7 was then computed for data resulting in $t = 7.12$. The ‘‘No Moon shadow’’ hypothesis can be therefore rejected with a significance of 3.1σ .

5.6.3 Angular resolution and absolute pointing

The angular resolution of a neutrino telescope is usually estimated through the Monte Carlo simulations. In particular it can be defined as the median of the distribution of the angular spreads between the reconstructed and the generated tracks. In the case of atmospheric muons, the median refers to the reconstruction errors with respect to the bundle direction.

The analysis of the Moon shadow profile represents an unique way to measure the angular

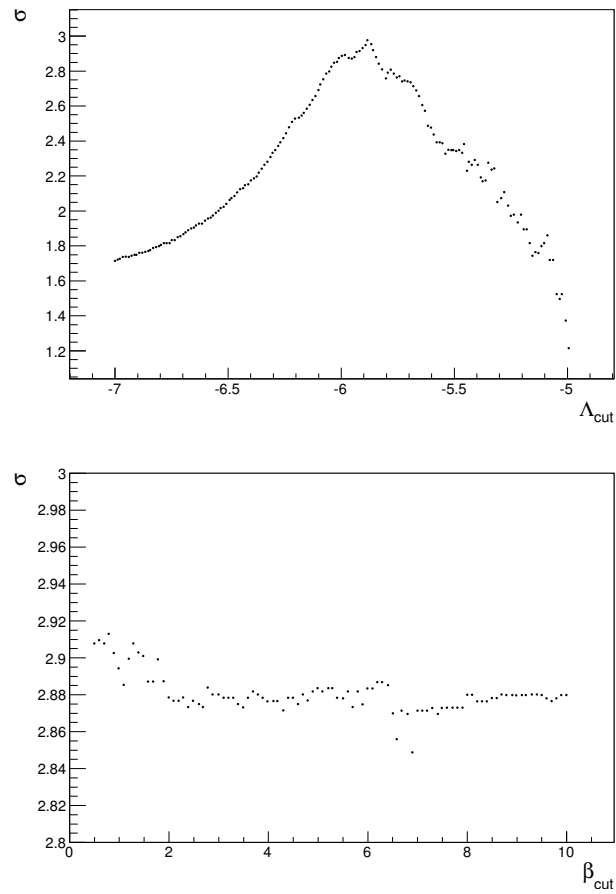


Figure 5.12: Top panel: expected significance (expressed as number of σ) as a function of Λ_{cut} . Bottom panel: expected significance (expressed as number of σ) as a function of β_{cut} (only events with $\Lambda > -5.9$).

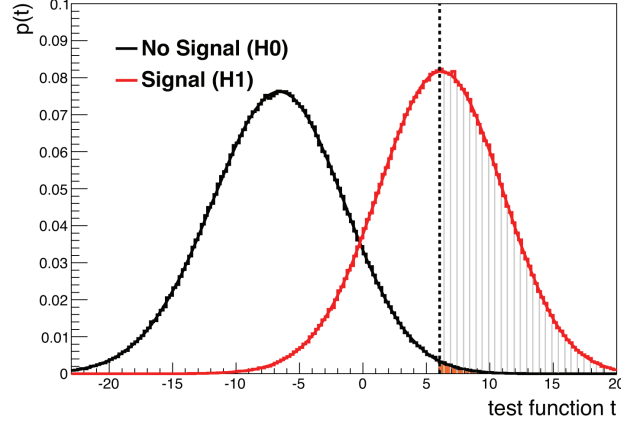


Figure 5.13: The test function t distribution for “Moon shadow” hypothesis (red curve) and “no Moon shadow” hypothesis (black curve). The shaded area is the fraction of the toy experiments where the Moon shadow hypothesis will be correctly identified as evidence of the shadowing effect. The orange area quantifies the median significance (2.9σ) to observe the Moon shadow.

resolution and the absolute pointing from data. The event density for selected muons is plotted in Fig. 5.14 as a function of the angular distance from the Moon centre.

Assuming a Gaussian shape for the detector point spread function [74], it is possible to evaluate the detector angular resolution fitting the event density with the formula:

$$\frac{dn}{d\delta^2} = k \left(1 - \frac{R_{Moon}^2}{2\sigma^2} e^{-\frac{\delta^2}{2\sigma^2}} \right), \quad (5.8)$$

where $R_{Moon} = 0.259^\circ$ is the Moon radius and δ is the angular distance from the Moon centre. The fit free parameters k and σ are respectively the off-source density level and the detector angular resolution.

The measure of the angular resolution from the fit is $\sigma = 0.7^\circ \pm 0.2^\circ$. This value is compatible with the expected angular resolution: $\sigma = 0.49^\circ \pm 0.14^\circ$, anyway this topic will be more deeply investigated during the absolute pointing estimation.

Finally the ANTARES absolute pointing performance was evaluated. It is possible that if the detector orientation is affected by a systematic error, the Moon shadow will appear shifted with respect to the expected position. In order to investigate this possibility, I have shifted the concentric rings around the Moon centre (see Sec. 5.6.2). In this way the detector will “point” in a wrong direction where a fainter shadowing effect is expected.

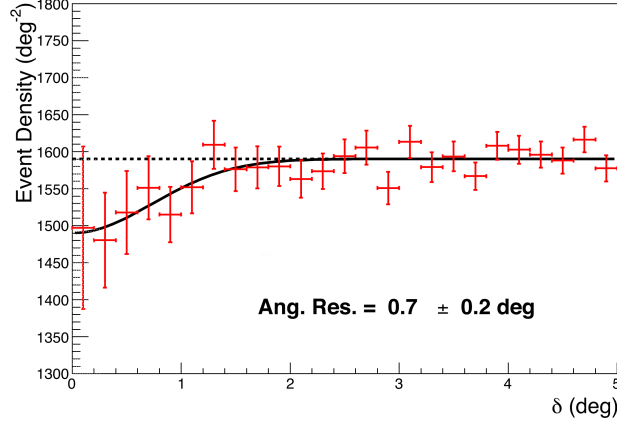


Figure 5.14: Event density of muons surviving the selection plotted versus the angular distance from the Moon centre. The shadow is fitted assuming a Gaussian shape for the detector point spread function resulting in an angular resolution of $\sigma = 0.7^\circ \pm 0.2^\circ$ for atmospheric muons. The shaded area represents the Moon angular radius $R_{Moon} = 0.259^\circ$.

The significance is around 3σ for small shifts ($\leq 0.1^\circ$) and decreases significantly while increasing the shifts. (Fig. 5.15). The

The histogram in Fig. 5.15 has been fitted with the two-dimensional Gaussian function:

$$\zeta(x, y) = N \cdot e^{-\frac{(x - x_0)^2}{2\sigma_x^2} - \frac{(y - y_0)^2}{2\sigma_y^2}}, \quad (5.9)$$

where $x = \Delta\phi \cos(\theta)$ and $y = \Delta\theta$, (x_0, y_0) are the centre coordinates, σ_x and σ_y are the standard deviations and N is the normalisation constant.

The centre of the Gaussian function is $x_0 = 0.51^\circ \pm 0.4^\circ$ and $y_0 = 0.05^\circ \pm 0.4^\circ$. The centre in the azimuthal direction is clearly compatible with a null shift, but in zenithal direction the shift is more consistent even if it is still compatible with a null deviation. According to the Monte Carlo ANTARES angular resolution (0.49°), this shift is less than a 1σ deviation from the expected position.

To take into account this possible mismatch, I have rigidly shifted the data according to the results of the fit of Fig. 5.15 and I have obtained a value of $0.55^\circ \pm 0.2^\circ$ for the angular resolution. This value is in better agreement with the expected value according to Monte Carlo simulation (0.49°), so $0.55^\circ \pm 0.2^\circ$ can be assumed as the measure of the ANTARES angular resolution for downgoing muons. The shift in Fig. 5.15 is under investigation and the ANTARES collaboration is putting a strong effort to understand the nature of this phenomenon. In any case recent Monte Carlo simulations showed that a rigid shift of the

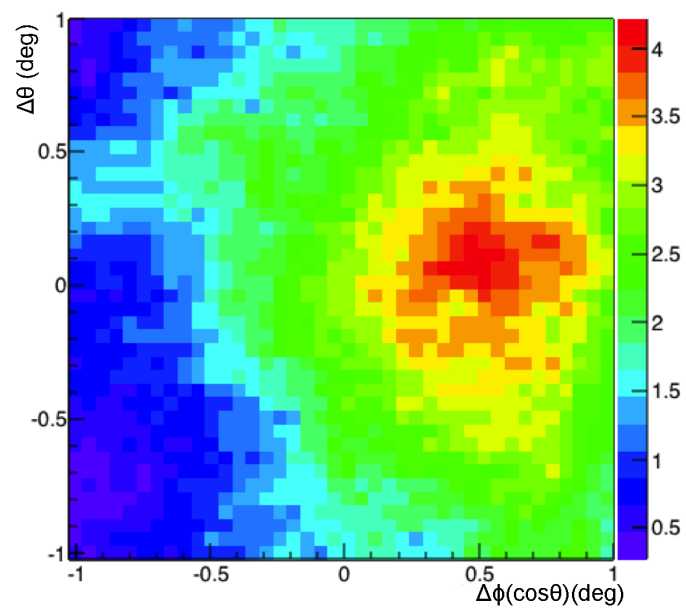


Figure 5.15: Significance (number of sigmas) of Moon shadow effect as function of the rings angular shift. $\Delta\theta$ indicate a shift in the zenith direction, $\Delta\phi$ indicate a shift in the azimuth direction.

ANTARES absolute pointing will not affect the ANTARES sensitivity in point-sources researches (Fig. 5.16). We expect a maximum efficiency loss of 6% .

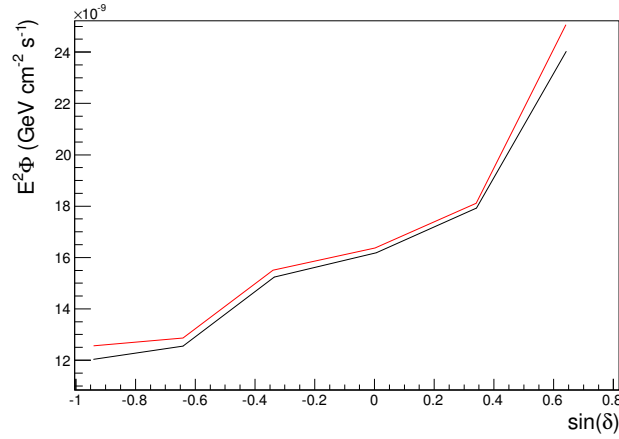


Figure 5.16: ANTARES point source sensitivity as a function of the declination angle. Black: null shift. Red: rigid shift of 0.5° in azimuthal direction.

Thanks to this analysis I performed the first Monte Carlo independent measure of the angular resolution and the absolute pointing accuracy of the ANTARES detector exploiting a celestial calibration source.

Chapter 6

GRB 130427A analysis

6.1 Introduction

In this chapter I present a search for a neutrino flux in correspondence of GRB 130427A, which was detected in 2013. It was a record-setting GRB, since it was the brightest ever detected. In fact GRB 130427A was the strongest burst since 1983 (GRB 830801) and it was also exceptionally close to the Earth (redshift=0.33), indeed one of the five closest GRBs ever detected [75]. This GRB has been associated to SN 2013cq, which was detected two weeks later on May 13, 2013 [76].

In my approach I assume a photospheric emission of gamma rays according to the model I have presented in Sec. 1.4. In this analysis I use the special sample of L0 data (Sec. 3.7) recorded by ANTARES in correspondence of the gamma ray burst. The data sample was triggered using a special directional trigger, known as MX (Sec. 3.8) and reconstructed with GridFit, the algorithm optimized at low energies (Sec. 4.6.2). The use of L0 data triggered with MX and reconstructed with GridFit leads to a substantial increase of the ANTARES sensitivity in the energy range where most of the neutrino emission is expected according to photospheric model (Sec. 4.6.3).

In order to optimize the selection on the quality parameters of the reconstructed tracks, the model discovery potential (MPD) is calculated as in the previous ANTARES GRB analysis where the standard analysis tools have been used [57].

The first steps of the MDP optimization (defined in Sec. 6.4) are the estimation of the signal and of the backgrounds of the analysis (Sec. 6.2 and Sec. 6.3 respectively).

6.2 The signal estimation

The expected neutrino flux according to the photospheric model in correspondence of GRB130427A has been estimated following the prescription from Zhang&Kumar [27]. The two authors provided through private communication the tools to estimate a neutrino flux as a function of the GRB parameters (Tab 6.1).

redshift	0.33
isotropic energy	$1.4 \cdot 10^{54}$ erg
10 keV -100 GeV fluence	$5 \cdot 10^{-3} \text{erg} \cdot \text{cm}^{-2}$
100 MeV-100 GeV fluence	$7 \cdot 10^{-4} \text{erg} \cdot \text{cm}^{-2}$
bulk Lorentz factor	550
time containing 90% of the fluence	276 s

Table 6.1: GRB130427A parameters derived by SWIFT observation [77].

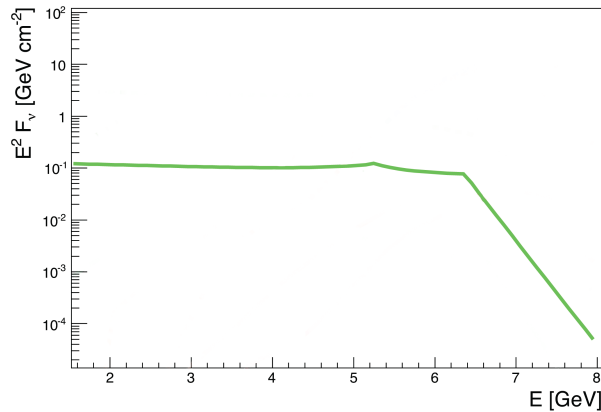


Figure 6.1: Expected neutrino flux according to photospheric model [27] from GRB130427A.

The expected neutrino flux shows approximately an E^{-2} spectrum between 50 GeV and 50 PeV and two strict cutoffs at lower and higher energies. The expectation of Fig. 6.1 can be compared with the neutrino flux from the same GRB according to NeuCosmA [78], a model based on internal shocks (Fig. 6.2).

The expected flux according to photospheric model is higher with respect to internal shock model, especially at energies between 10^2 and 10^5 GeV. This interval corresponds to the energetic range where the analysis proposed in this thesis is more efficient than the

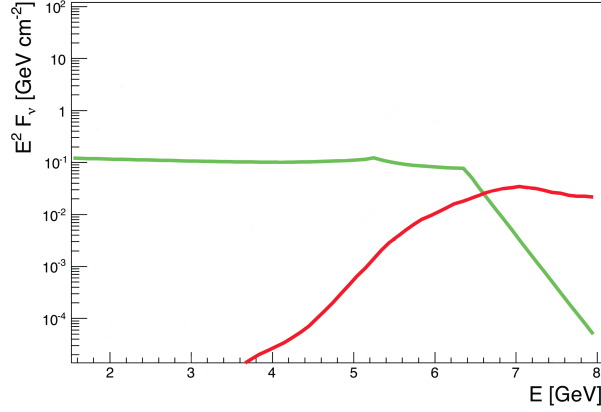


Figure 6.2: GRB130427A expected neutrino flux according to photospheric model [27] and internal shock model [78]

standard ANTARES analysis (Sec. 4.6.3).

I produced a simulation of the GRB130427A neutrino flux according to the photospheric model using GENHEN (Sec. 4.2). I simulated a sample of L0 data (500 millions neutrino events properly weighed) (Sec. 3.7) and I triggered it with *TriggerEfficiency* [53], a code that allows the triggering of the simulated hits similarly to the process that is performed online on real data. The simulation takes into account the experimental conditions during the recording of the GRB, such as the status of each PMT, the detector configuration, the actual environmental conditions and optical background.

In my simulation I triggered the simulated hits with all ANTARES online triggers (Sec. 4.2) and also with the special directional trigger MX (Sec. 3.8). The simulated data have been finally reconstructed with GridFit, an algorithm that is optimized for the energetic range where the photospheric neutrino flux is expected (Sec. 4.6.2).

The point spread function of the simulated neutrinos, defined as the response of the detector to a point source, is shown in Fig. 6.3.

The fitted function is

$$s(\alpha) = \log \frac{dN}{d\Omega} = \begin{cases} A & \text{if } \alpha \leq \alpha_0 \\ A - B(1 - e^{-\frac{(\alpha - \alpha_0)^2}{2\sigma^2}}) & \text{if } \alpha > \alpha_0 \end{cases} \quad (6.1)$$

where A and B are normalization constants, α is the angle between the reconstructed track direction and the true MC neutrino direction in degree and α_0 is the angular distance where the event density starts to decrease.

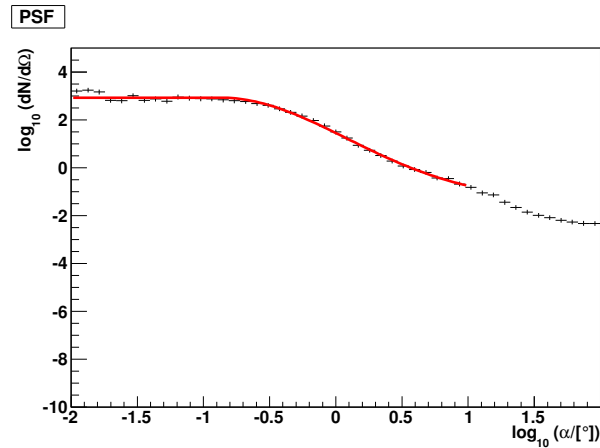


Figure 6.3: Point spread function of expected neutrino signal from GRB130427A. Using L0 data simulation reconstructed with GridFit and triggered with the directional trigger MX.

This function is used for building the signal probability density function (PDF) and referred to as $S(\alpha)$ (Sec. 6.4).

6.3 The background estimation

In the previous ANTARES GRB analysis [57], the background has been estimated from the average behaviour of the measured data during at least one run period of time (few hours). The small duration of GRB L0 files in my case (a couple of minutes) and the dependence on bioluminescence conditions make the direct application of this strategy impossible. The small statistics prevents a robust direct estimate for a single data sample.

In order to find alternative solutions I have performed a background study which allowed to estimate the contribution of random coincidences and of atmospheric muons.

6.3.1 The random background

First I produced a random background data sample thanks to the *RandomTimeSliceWriter* code [79]. This program allows the generation of random background L0 data with a pre-determined rate of single photo-electron hits and local coincidences. In my case I selected the present environmental condition during GRB130427A. This simulated data sample has been triggered with the directional trigger MX and reconstructed with GridFit with the same procedure as applied previously on the simulated sample of neutrino events (Sec. 6.2).

The distribution of random background and neutrino signal events is shown in Fig. 6.4

as a function of the quality parameter of the reconstructed tracks. For the signal events two different distribution are reported: L0 data reconstructed with GridFit using online triggers and MX and L1 data reconstructed with AaFit using online trigger (standard ANTARES reconstruction chain).

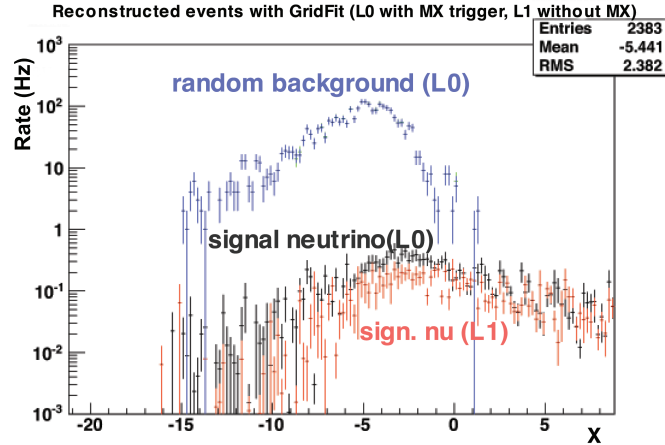


Figure 6.4: Distribution of random background rate (blue) and signal neutrino rate as a function of the quality parameter X . Neutrino signal: L0 data reconstructed with GridFit using online triggers and MX (black), L1 data reconstructed with AaFit using online trigger (red).

The random background dominates for low quality cut on X ($X < 2$), the quality parameter X defined in Sec. 4.6.2. If I choose value of the quality parameter X above 3, the random background seems to be negligible. This hypothesis will be tested in the next section (Sec. 6.3.2) on a sample of L0 data.

6.3.2 The atmospheric muon background

An estimation of the muon background driven directly by data is not possible because of the lack of statistic in the GRB L0 files (duration of a couple of minutes). It will be also desirable to avoid the simulation of all L0 data samples because it is very CPU time demanding. A good approach could be the simulation of a small sample of L0 data in order to find a relationship between them and the corresponding sample of the official ANTARES Run by Run (RbR) L1 Monte Carlo simulation. Similarly to my L0 data simulation, also the RbR Monte Carlo takes into account the experimental conditions of each data run, such as the status of each PMT, the detector configuration, the actual environmental conditions and optical background [72].

Following this approach I can estimate the muon background misreconstructed as upgoing relying only on the official Run by Run Monte Carlo provided by the collaboration. However the relationship between my simulation of L0 data and the L1 simulation must be true for all the ANTARES data sample and it must not depend on environmental condition. A good relationship that can be used to evaluate the muon background is defined in Eq. 6.2:

$$C = \frac{\frac{\mu_{\uparrow}(L0)}{\mu_{\downarrow}(L0)}}{\frac{\mu_{\uparrow}(L1)}{\mu_{\downarrow}(L1)}} \quad (6.2)$$

where $\mu_{\uparrow/\downarrow}(L0)$ is the number of upgoing/downgoing muons in my L0 data simulation and $\mu_{\uparrow/\downarrow}(L1)$ is the number of upgoing/downgoing muons in the corresponding Run by Run Monte Carlo simulation (L1 data).

I have studied the parameter C to check if it is constant in time and if it depends on the environmental condition of the detector. Fig. 6.5 shows the value of the parameter C for different runs (chosen randomly in order to get runs with different conditions: baseline rate 50-120 kHz, burst fraction 0-0.7, number of active OMs 520-720) as a function of the quality cut. Fig. 6.5-bottom shows the value of C assuming a cut that could be likely selected by the MDP optimization ($X=5$).

The ratio parameter C is quite constant in time and weakly depends on the detector condition or bioluminescence background if the quality cut X is between 0 and 6 (where the quality cut will likely be according to the optimization of Sec. 4.6.3)). As shown in Fig. 6.5-bottom the small fluctuation around $X = 5$ are simply statistical and the parameter C can be assumed constant.

For poor cut on X ($X < 0$) the different run conditions leads to large fluctuations on the parameter C . In any case I can neglect these fluctuations because it is very unlikely that the MDP optimization will select a so loose quality selections ($X < 0$), as shown in Sec. 4.6.3.

The fluctuations in Fig. 6.5 for quality cut above 6 are due to lack of statistics. A misreconstructed downgoing muon has a very low probability to produce a so good reconstructed ‘‘upgoing’’ track, so very few events of this kind are simulated in my data sample. However also a so extremely good cut on the quality parameter is very unlikely to be selected by the MDP optimization.

In conclusion thanks to Eq.6.2, the parameter C can be used to evaluate the number of expected upgoing muons in a L0 data sample $\mu_{\uparrow}(L0data)$ as

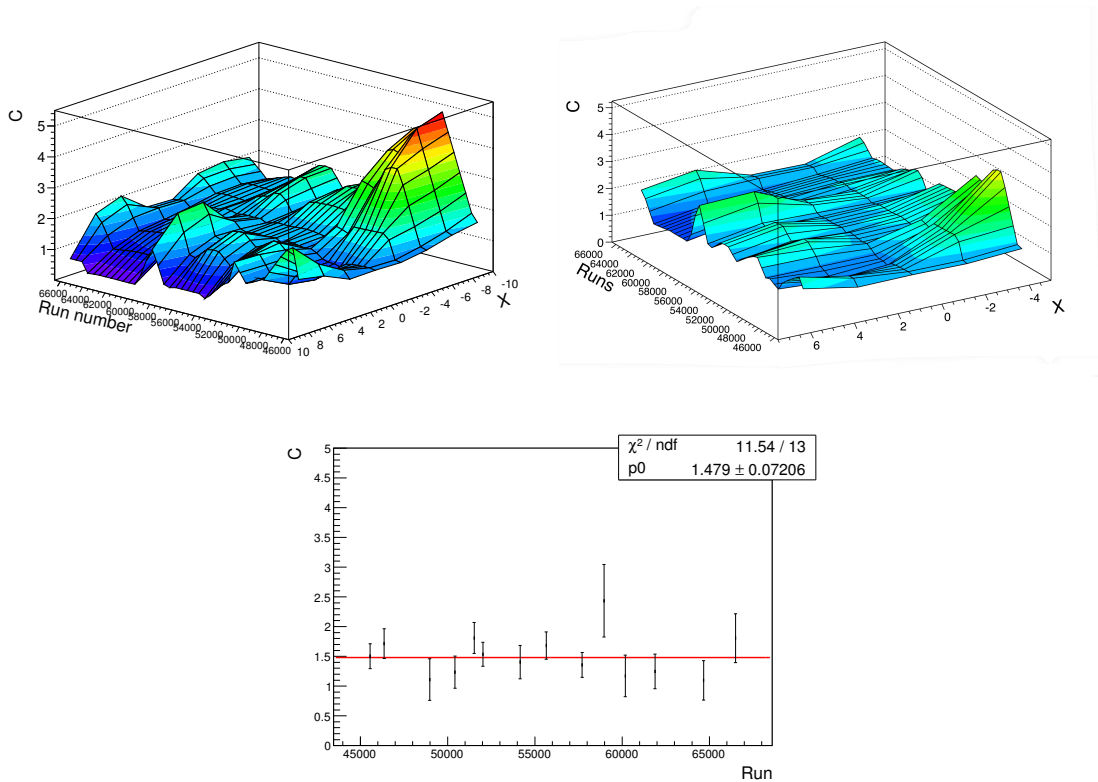


Figure 6.5: Value of the ratio C for different runs as a function of the cut on the quality parameter X (top left). Value of the ratio C for different runs focusing on the region between $X = -5$ and $X = 7$ (top right). Value of the ratio C for different runs with quality cut $X = 5$ (bottom), in this case the average value of C is 1.48 ± 0.08

$$\mu_{\uparrow}(L0data) = C \cdot \mu_{\downarrow}(L0data) \frac{\mu_{\uparrow}(L1MC)}{\mu_{\downarrow}(L1MC)}, \quad (6.3)$$

where $\mu_{\downarrow}(L0data)$ is the number of downgoing muons in my L0 data sample and $\mu_{\uparrow/\downarrow}(L1MC)$ is the number of upgoing/downgoing muons in the corresponding Run by Run Monte Carlo simulation (L1 data).

In order to take into account the zenith dependence of the muon background, I have studied the ratio L0 data / L1 data for different zenith angle values (Fig. 6.6).

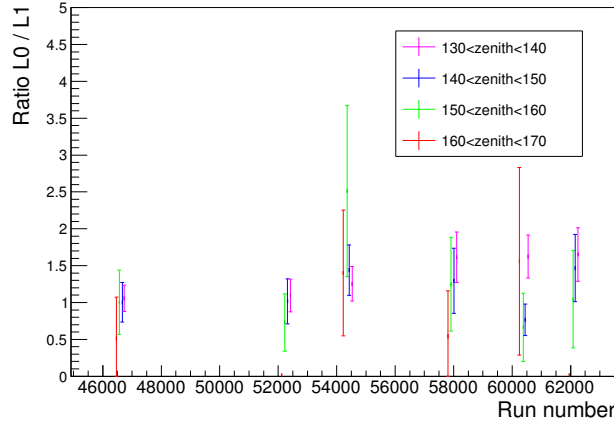


Figure 6.6: Value of the ratio L0/L1 for different zenith angles as a function of run number.

The ratio L0/L1 does not change significantly for different zenith angle within my search window. In any case I want my estimation of the background to be conservative, so I will consider as upgoing muon background of my analysis the quantity provided by Eq. 6.3 multiplied by a factor 2 in order to take into account the fluctuation of Fig. 6.6.

The estimation provided by Eq. 6.3 has been tested on a data sample. I have compared the number of upgoing events recorded in the L0 file of GRB130427A (all upgoing sky except the cone of 10 degrees radius around the GRB) with my estimation according to Eq. 6.3. The results are shown in Fig. 6.7. For reference also the random background contribution is reported, it has been simulated thanks to *RandomTimeSliceWriter* code as described in Sec. 6.3.1.

The agreement is good for $X \geq 3$. For lower values of this quality parameter there is an under-estimation of the background due to the fact that the random background (bioluminescence and ^{40}K decay) dominates, as shown in Fig. 6.4. Above $X=4.5$ a direct

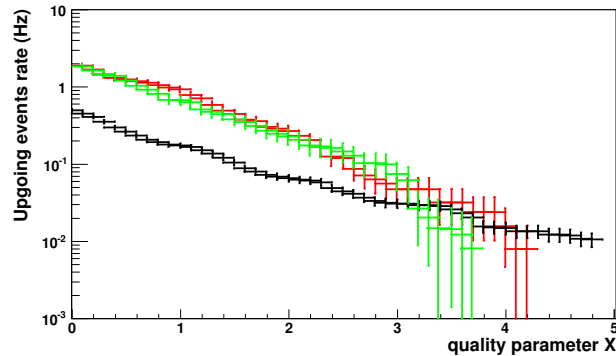


Figure 6.7: A posteriori comparison between the rate of upgoing muons recorded in the L0 file of GRB130427A (all upgoing sky except the cone of 10 degrees radius around the GRB) (red), the expected muon rate (black) thanks to Eq. 6.3 and the random background rate simulation (green)

comparison of the estimated number of upgoing muons with the reconstructed events in the L0 data file is not possible due to the lack of statistic in the data. In conclusion my background estimation can neglect the contribution of random background given that the optimized quality cut predicted by the MDP optimization is above 3 (as it is likely be according to the optimization of Sec. 4.6.3). If this is not the case, I will reconsider my estimation of the background in order to include also random background.

This background estimation could be very useful in future if the ANTARES collaboration decides to perform a stacking analysis with all the GRB L0 files recorded by the detector. Thanks to this estimation it is not necessary to simulate all the L0 data samples. In fact the estimation relies only on the official RbR Monte Carlo simulation and the number of downgoing events in the L0 data file. The simulation of a huge quantity of L0 data files would lead to severe issues of CPU time consumption and disk storage.

The background probability density function (PDF) $B(\alpha)$ used in my MDP optimization is assumed uniform in the 10 degrees search window (the variation due to the zenith angle affects the background estimation at the level of a few percents) and calculated according Eq. 6.3. The model discovery potential optimization will be presented in the next section.

6.4 Optimization of the quality parameter cut

In this section I will describe how the model discovery potential optimization is performed in order to derive the best selection criterion on the quality parameter X of the recon-

structured tracks. This will lead to the determination of the best flux limits that the ANTARES detector can provide with this analysis.

According to the signal and background probability density functions (PDFs), as defined in Sec. 6.2 (Eq. 6.1) and Sec. 6.3.2 (Eq. 6.3), pseudo-experiments are produced to derive the distribution of the extended maximum likelihood Q [80]. The extended maximum likelihood Q is defined as [80]

$$Q = \max_{\mu_{sig} \in [0, n_{tot}]} \sum_{event}^{n_{tot}} \log \frac{\mu_{sig} \cdot S(\alpha_i) + \mu_{bg} \cdot B(\alpha_i)}{\mu_{bg} \cdot B(\alpha_i)} - (\mu_{sig} + \mu_{bg}), \quad (6.4)$$

where S (Eq. 6.1) and B (Eq. 6.3) represent the signal and background PDF (as explained in Sec. 6.2 and Sec. 6.3.2), i is the index of the event with space angle α_i with respect to the GRB direction, μ_{bg} is the expected number of background events and μ_{sig} is the signal contribution. In this computation the number of expected background events is assumed to be known a priori [80]. Eq. 6.4 can be interpreted as follows. The extended maximum likelihood is obtained by maximizing the log-likelihood function for the signal and comparing it with the background only value (the denominator in Eq. 6.4). Values of the extended maximum likelihood Q around 0 are compatible with the background-only hypothesis, while higher values of Q are more compatible with signal hypothesis.

In the pseudo experiments the space angle α_i of signal or background events is generated according to the signal or background PDFs ($S(\alpha)$ or $B(\alpha)$ respectively). The probability density functions have different values depending on to the chosen cut on the track quality parameter X .

The value of μ_{sig} that maximizes the extended maximum likelihood is the number of estimated signal events ($\mu_{est\ sig}$). In other words it is the number of signal events that have ‘‘likely’’ originated a specific pseudo-experiment.

This computation of the extended maximum likelihood has an important advantage with respect to more simple counting approaches. In this analysis the spatial distribution of the signal is taken into account (thanks to the $S(\alpha)$ and $B(\alpha)$ PDFs), while the angular distribution information is completely neglected in a counting analysis. This leads to a more accurate estimation of the measured significance.

Defining

$$h_{n_s}(Q) = \left(\frac{\delta N}{\delta Q} \right)_{n_s}, \quad (6.5)$$

$h_{n_s}(Q)$ is the distribution of Q-values if n_s signal events are simulated in the pseudo-experiment. The background is generated according to a Poisson distribution with expectation value μ_{bg} , the value known “a priori”.

In Fig. 6.8 the distribution of the log-likelihood ratio $h_{n_s}(Q)$ is produced generating 10^9 background-only pseudo-experiments (black distribution) and 10^5 background+(1,2,...,9) signal pseudo-experiments (coloured distributions).

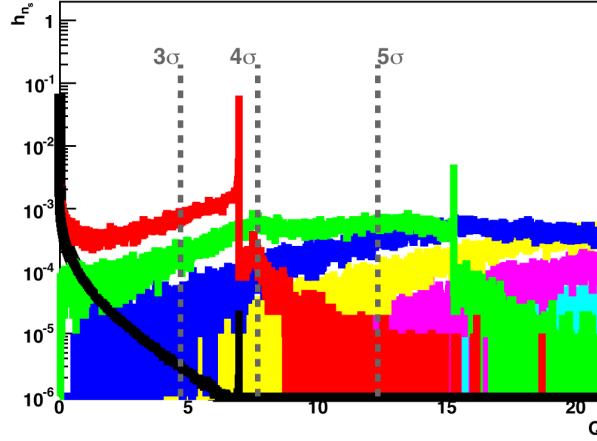


Figure 6.8: $h_{n_s}(Q)$ distributions. Black: background-only. Red (green, blue, yellow, pink, light blue): background+1,2,3,4,5,6 signals. The threshold values of Q for 3σ , 4σ and 5σ discovery are indicated with grey lines (see text for more details).

The threshold values of Q for 3σ , 4σ and 5σ discovery are indicated with grey lines in Fig. 6.8. In other words a 5σ discovery can be claimed if the measured value of the extended maximum likelihood Q is above 12.3. The peaks in the Q value distribution (around $Q=7$ and $Q=15$) correspond to pseudo-experiments with events very close to the search direction. At the limit of small space angles, the ratio of signal and background PDFs tends to a constant (the Q value of the peak). In fact having $\alpha \sim \alpha_0$ the signal probability density function $S(\alpha)$ becomes

$$\lim_{\alpha \rightarrow \alpha_0} \log \frac{dN}{d\Omega} = \lim_{\alpha \rightarrow \alpha_0} A - B(1 - e^{-\frac{(\alpha - \alpha_0)^2}{2\sigma^2}}) = A \quad (6.6)$$

and the background probability density function $B(\alpha)$ is assumed constant (Sec. 6.3.2). The second peak of the background-only distribution (black curve) at $Q=7$ represents pseudo-experiments where a background event has been reconstructed close to the direction

of the GRB and will be wrongly recognized as a signal event. The peaks in the red and green histograms (background + 1 signal and background + 2 signals) correspond respectively to pseudo-experiments where one or two events are reconstructed with a small space angle. In other words for the likely cuts on the quality parameter X (around $X=5$) the expected number of signal events is around 0.2 and the expected number of background events is around 0.001, so if an event is reconstructed with a space angle below 3° the algorithm will conclude that it is very likely a signal event and its value of the maximum likelihood will be around 7. It can be noted that the red peak (background + 1 signal event) at $Q=7$ is several orders of magnitude higher with respect to the corresponding black peak (background-only). This means that if an event is detected close to the GRB position, it is very unlikely that it is a background event. The peaks at $Q=0$ of the background-only and background + 1 signal event distributions correspond to pseudo-experiments where no events are reconstructed in the search window.

The p-value p provides the significance of the measure. It is defined as the probability to measure Q -values at least as high as the observed one if the background-only hypothesis were true. In other words the lowest value of the extended maximum likelihood Q_{thres} that leads to a claim of discovery with a certain p-value is derived through

$$p = P(Q \geq Q_{thres}) = \int_{Q_{thres}}^{\infty} h_0(Q) dQ, \quad (6.7)$$

where $h_0(Q)$ is the Q -value distribution in the background-only hypothesis (black histogram in Fig. 6.8). The corresponding values of Q_{thres} for 3σ , 4σ and 5σ significance are reported in Fig. 6.8.

The probability to measure a certain value of Q if the expected number of signal events is $\mu_{est sig}$ is given by

$$P(Q|\mu_{est sig}) = \sum_{n_s=0}^{+\infty} P(n_s|\mu_{est sig}) h_{n_s}(Q), \quad (6.8)$$

where $P(n_s|\mu_{est sig})$ is the Poissonian probability of observing n_s events if the mean number of expected events is $\mu_{est sig}$.

Finally the value of the model discovery potential (MDP) is given by the integral of $P(Q|\mu_{est sig})$ [80] :

$$MDP = P(Q \geq Q_{thres} | \mu_{est\ sig}) = \int_{Q_{thres}}^{\infty} P(Q | \mu_{est\ sig}) dQ = \sum_{n_s=0}^{+\infty} P(n_s | \mu_{est\ sig}) \int_{Q_{thres}}^{\infty} h_{n_s}(Q) dQ \quad (6.9)$$

The MDP is calculated for different cuts on the quality parameter X in order to find the selection criteria that maximize the analysis sensitivity as reported in Fig. 6.9.

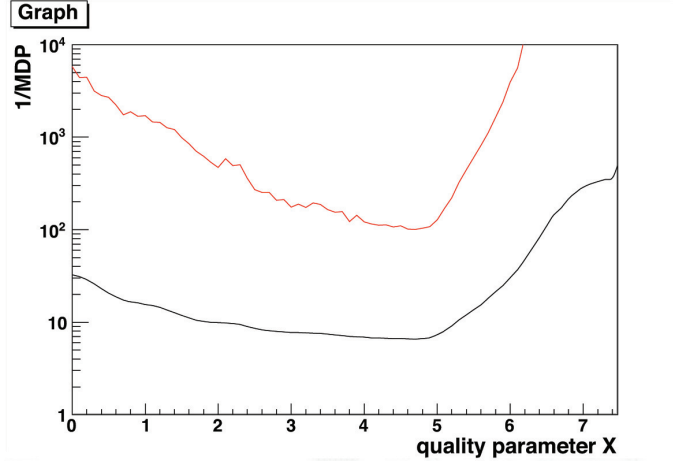


Figure 6.9: Model discovery potential ($1/MDP$) as a function of the quality parameter X for different significance levels: 3σ (black), 5σ (red).

The optimization predicts the same quality cuts for both significance levels of 3σ and 5σ : $X > 4.7$ (respectively black and red curve). This selection is then applied on the GRB data sample and the corresponding value of Q is calculated and finally converted into an upper limit on the flux or into a significance if a discovery can be claimed.

Before the research of a signal evidence in the data, the method provided by my analysis to compute the expected limit is explained in the next section.

6.5 The average upper limit

Although I could not set an upper limit on the neutrino flux before analysing the GRB data sample, it was possible to use the tools previously described (Sec. 6.4) to calculate an “average upper limit”. This limit is computed after hypothetical repetition of the experiment with expected background μ_{bg} and no true signal.

The 90% C.L. average upper limit on the flux is defined as

$$\overline{F}(E)_{90\%} = F(E) \frac{\overline{\mu}_{90\%}}{n_s} \quad (6.10)$$

where $F(E)$ is the expected signal fluence, n_s is the expected number of signal events and $\overline{\mu}_{90\%}$ is the 90% C.L. average upper limit on the number of signal events.

The computation of $\overline{\mu}_{90\%}$ will be now described. After the analysis of the GRB data sample, I obtain a value of the extended maximum likelihood Q . This Q -value is converted into a 90% C.L. upper limit. In other word I can reject all the fluxes that lead to Q -values greater than the measured one for more than 90% of the pseudo-experiments.

Before the research of a signal evidence in the data I do not have the measured Q -value, so I can only derive the average upper limit thanks to Fig. 6.10 where the probability of a certain value of Q is shown as a function of the number of estimated signal events ($\mu_{est\ sig}$).

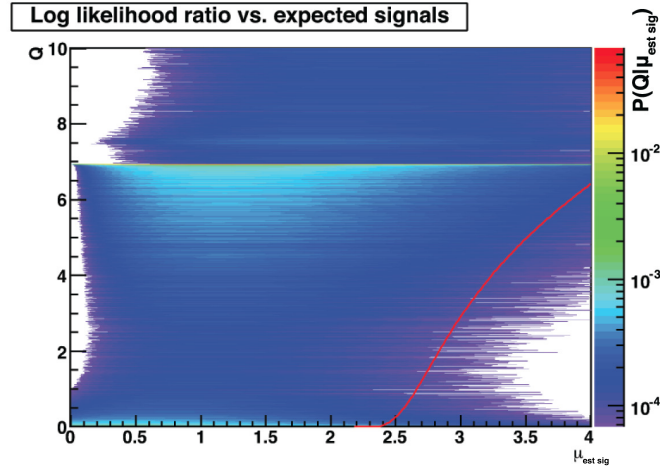


Figure 6.10: Probability of a given value of Q as a function of the estimated number of signal. For each value of signals, the red curve indicates the limit between the lower 10% of the distribution and the upper 90%.

I have calculated the probability $P(Q|\mu_{est\ sig})$ according to Eq. 6.8. The lighter regions in Fig. 6.10 correspond to the peaks around $Q = 0$ and $Q = 7$ of Fig. 6.8 that have been discussed above.

The value of $\overline{\mu}_{90}$ is determined by the median value of Q in the background-only hypothesis ($\overline{Q}_{bg} \simeq 0$ as can be seen in Fig. 6.8). This Q -value can be converted into $\overline{\mu}_{90}$ looking which estimated number of signal value $\mu_{est\ sig}$ corresponds to \overline{Q}_{bg} on the red curve of Fig. 6.10 (the red curve indicates the limit between the lower 10% of the distribution and the upper 90% for each value of signals). In this case $\overline{\mu}_{90}=2.37$. In other word I have rejected all the

values of the estimated number of signal that lead to Q -values greater than $\overline{Q_{bg}}$ for more than 90% of the pseudo-experiments.

Using Eq. 6.10 I can finally derive the average upper limit on the flux, as shown in Fig. 6.11.

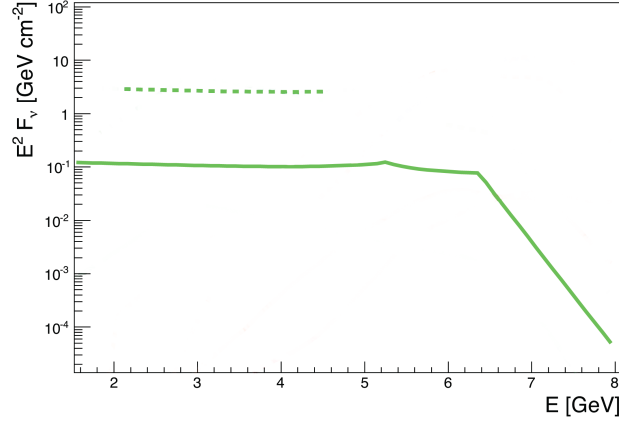


Figure 6.11: Average upper limit (dashed line) and expected neutrino flux (solid line) of GRB130427A according to photospheric model.

The analysis has been performed also assuming the NeuCosmA model with the latest measure of the GRB parameters and the limit has been derived. In Fig. 6.12 these average upper limits are compared with the result of the previous ANTARES research of a neutrino flux from GRB 130427A [57].

The upper limit of this analysis is set in an energetic range that is still unexplored by the ANTARES detector. This achievement was obtained thanks to the expected neutrino flux according to GRB photospheric model, but also thanks to the special analysis tools used in this analysis. The L0 data sample (Sec. 3.7), the directional trigger MX (Sec. 3.8) and the GridFit reconstruction algorithm (Sec. 4.6.2) all contribute together to enhance the ANTARES sensibility in the energetic range between 50 GeV and $3 \cdot 10^4$ GeV. The enhancement at higher energy is less significant, in fact the limit on the NeuCosmA model is compatible with the previous analysis. The different shape of the upper limit is due to the spectrum assumed in the previous ANTARES analysis, slightly different GRB parameter estimations have been used.

The enhancement is clear in Fig. 6.13 where the ratio between the effective area of my analysis and the standard ANTARES analysis is shown.

As expected the increase of the effective area is clear at low energies (below 10^4 GeV), whereas the analysis effectiveness is compatible with the standard analysis at higher ener-

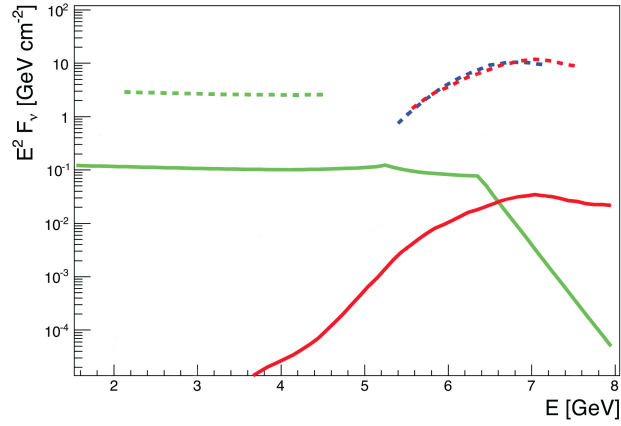


Figure 6.12: Upper limit (dashed line) and expected flux (solid line) of GRB130427A for different models. This thesis analysis (average upper limit): photospheric model [27] (green), NuCosmA model [78] (red). Previous ANTARES analysis [57]: NuCosmA model [78] (blue).

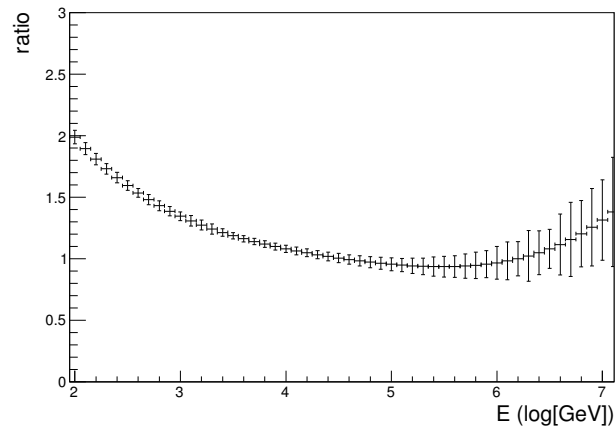


Figure 6.13: Ratio between my analysis (L0 data) and standard ANTARES analysis (L1 data) effective area.

gies.

In the next section the result after the analysis of the data sample corresponding to GRB 130427A is presented.

6.6 Results of the analysis

In astroparticle physics the blinded analyses are commonly used in order to avoid bias driven by the scientist expectations. In this thesis a sky region well outside the GRB direction has been considered. Blind analysis ensures that all analytical decisions have been completed and all programmes and procedures debugged, before the real data have been revealed to the experimenter.

Once all the collaboration agrees that the analysis is sufficiently accurate to publish whatever the result turns out to be, without further rounds of debugging or rethinking, the data are unblinded and the final results of the analysis are derived.

The analysis proposed in this thesis has been deeply investigated by the ANTARES collaboration and the authorization of data unblinding has been granted on the 15th february 2016. The analyzed data sample corresponds to the L0 data recorded during the alert of GRB130427A (Sec. 3.7).

This exceptionally bright gamma ray burst has been detected by the Fermi Large Area Telescope at 07:47:06.42 UTC of the 27 April 2013. The alert from the GRB satellite network was received at 07:47:14, 8 seconds after the detection by the satellite.

The data sample recorded by ANTARES in correspondence of the GRB includes also some signals detected before the gamma ray burst alert because data were still in the memory of the DAQ programs PC before filtering procedure being applied. In the case of GRB130427A, 50 seconds of data were still unfiltered at the moment of the alert, so they have been included to the analysis data sample. In conclusion the GRB130427A data sample corresponds to 270 seconds, starting at 07:46:24 and ending at 07:50:54. It includes all the duration of the GRB, according to Fermi LAT GRB130427A emitted 90% of its flux in 173 seconds, lasting at 07:49:49.

The optimized selection criterion derived maximizing the model discovery potential (Sec. 6.4) is applied on the GRB13027A data sample and the number of events that satisfy the quality cut are counted.

No events have been found in the search window of 10° around the GRB position (right ascension = 173.15° , declination = 27.70°); thus the corresponding value of the extended maximum likelihood Q_{meas} (Eq. 6.4) is 0.

The value of Q_{meas} can be used to derive the 90% C.L. upper limit as shown in Sec. 6.5.

The upper limit is defined as

$$F(E)_{90\%} = F(E) \frac{\mu_{90\%}}{n_s} \quad (6.11)$$

where $F(E)$ is the expected signal fluence, n_s is the expected number of signal events and $\mu_{90\%}$ is the 90% C.L. upper limit on the number of signal events.

The value of $\mu_{90\%}$ is derived thanks to Fig. 6.14 that is reproduced below.

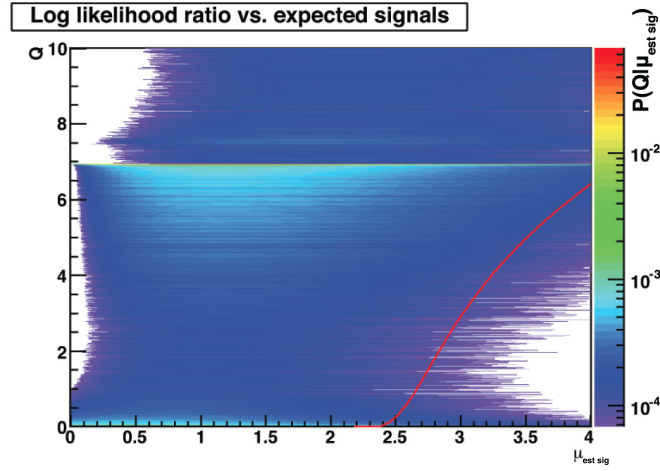


Figure 6.14: Probability of a given value of Q as a function of the estimated number of signal. For each value of signals, the red curve indicates the limit between the lower 10% of the distribution and the upper 90%.

I will reject all the fluxes that lead to Q -values greater than the measured one for more than 90% of the pseudo-experiments, the generation of pseudo-experiments is presented in Sec. 6.4. Q_{meas} can be converted into $\mu_{90\%}$ looking which estimated number of signal value $\mu_{est sig}$ corresponds to Q_{meas} on the red curve of Fig. 6.14 (the red curve indicates the limit between the lower 10% of the distribution and the upper 90% for each value of signals). In other word I have rejected all the values of the estimated number of signal that lead to Q -values greater than the measured one for more than 90% of the pseudo-experiments.

In conclusion the value of $\mu_{90\%}$ is 2.37 and the expected number of signal events n_s is 0.22. The value of n_s has been derived thanks to the Monte Carlo simulation described in Sec. 6.2.

Finally the 90% C.L. upper limit on the neutrino fluence from GRB130427A obtained by this analysis is calculated thanks to Eq. 6.11 and is presented in Fig. 6.15):

$$F(E)_{90\%} = 3.1 \cdot E^{-2} \text{GeV} \cdot \text{cm}^{-2} \quad (6.12)$$

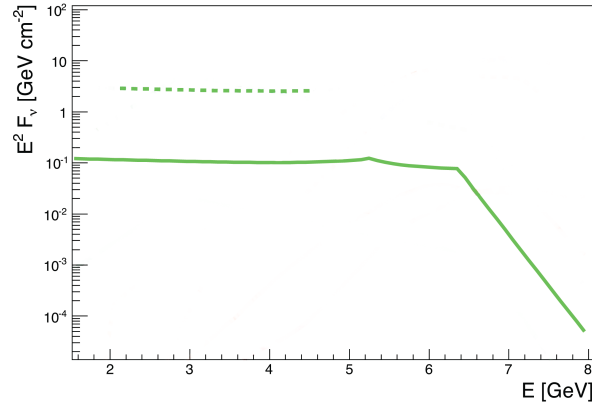


Figure 6.15: 90% C.L. upper limit (dashed line) and expected neutrino flux (solid line) of GRB130427A according to photospheric model.

In Fig. 6.16 the limit derived by this analysis assuming a photospheric GRB emission is compared with the results from previous ANTARES analysis [57], where different models were assumed.

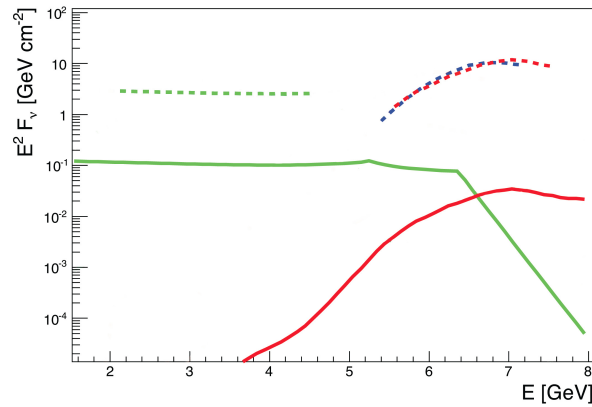


Figure 6.16: Upper limit (dashed line) and expected flux (solid line) of GRB130427A for different models. This thesis analysis: photospheric model [27] (green), NeuCosmA model [78] (red). Previous ANTARES analysis [57]: NeuCosmA model [78] (blue).

The limit set by this analysis sits in a energetic range completely unprecedented for the

ANTARES detector. This result has been obtained in accordance to the photospheric model expectations of a lower energetic flux, but also thanks to the special analysis tools used in this analysis to enhance the ANTARES sensitivity at lower energies: the un-triggered data sample (Sec. 3.7), the directional trigger (Sec. 3.8) and the reconstruction algorithm optimized for low energies (Sec. 4.6.2). In this analysis the ANTARES sensitivity has been enhanced between 50 GeV and 300 TeV, up to a factor 2 at 50 GeV (Fig. 6.13).

In the next section (Sec. 6.7) the analysis has been performed also on another promising gamma ray burst and the upper limits on the neutrino flux have been derived.

6.7 GRB130505A analysis

On the 5th May 2013, a few days after GRB130427A, another promising gamma ray burst has been detected. The main characteristics of GRB130505A are summarized in Tab 6.2.

redshift	0.33
isotropic energy	$5.63 \cdot 10^{54}$ erg
20 keV -10000 KeV fluence	$3.13 \cdot 10^{-4} \text{ erg} \cdot \text{cm}^{-2}$
time containing 90% of the fluence	88 s
L0 data file length	168 s

Table 6.2: GRB130505A parameters derived by SWIFT observation [77].

GRB130505A is the gamma ray burst with the largest isotropic energy ever measured, but the expected neutrino flux is much lower with respect to GRB130427A. The analysis described in the previous sections has been performed also on the L0 data sample corresponding to GRB130505A and no major differences have been found during the optimization of the selection criterion on the track quality parameter. The average upper limits for GRB130505 are compared with the limits derived in the previous section in Fig. 6.17.

As expected the limits set on GRB130505A are compatible with the limits of GRB130427A, but this time they are less constraining with respect to the expected flux because it is considerably lower.

In the next chapter the analysis most important features are summarized and the prospect for future improvements are presented.

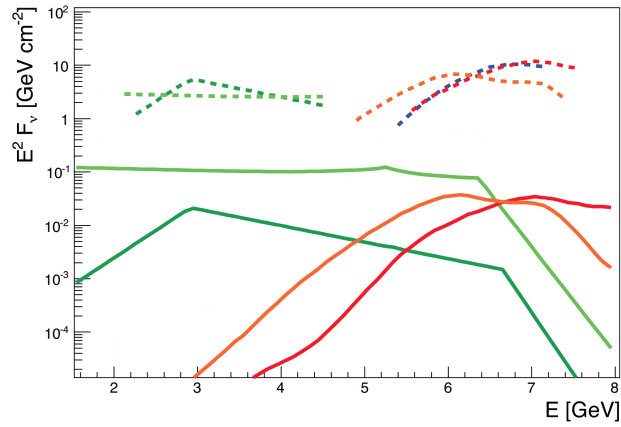


Figure 6.17: Upper limit (dashed line) and expected flux (solid line) of GRB130505A for different models: photospheric model [27] (dark green), NeuCosmA model [78] (orange). Upper limit (dashed line) and expected flux (solid line) of GRB130427A for different models. This thesis analysis: photospheric model [27] (bright green), NeuCosmA model [78] (red). Previous ANTARES analysis [57]: NeuCosmA model [78] (blue).

Conclusions

The exceptionally bright gamma ray burst of 27th April 2013 raised an outstanding interest by the scientific community. The possible evidence of neutrino emission in correspondence of this GRB will give important constrains on the emission mechanisms of gamma ray bursts and it will give an indication of which emission model is most promising.

A very recent and widely discussed GRB emission mechanism is the so-called photospheric model. It is very promising because it provides an explanation of some measured features of the gamma ray bursts that are not expected according to previous models. The photospheric model predicts a sensible neutrino emission in an energetic range a couple of order of magnitude lower with respect to the classical models.

GRB130427A is in the sky view of the ANTARES experiment. The collaboration has expressed therefore a major effort to search for a possible neutrino emission. To this extent in this thesis a completely innovative method of research has been proposed and dedicated tools have been developed to enhance the ANTARES sensitivity in the energetic range predicted by the photospheric model (50 GeV and 10^4 GeV). For the first time the data sample of unfiltered data registered in correspondence of a gamma ray burst has been used in an ANTARES physics analysis; this data sample contains more information with respect to the standard filtered data used in the other analyses. The sensitivity of the detector is improved using a dedicated directional trigger and a special reconstruction algorithm optimized at lower energies. As a result, my analysis has enhanced the sensitivity up to a factor 2 for energies between 100 GeV and 1 TeV.

This analysis did not yield to a measure of a neutrino flux in correspondence of GRB130427A and GRB130505A, but it allowed to set an upper limit on the neutrino flux from the gamma ray burst in an energetic range which fits the predictions of the most recent GRBs emission models.

The analysis proposed in this thesis could be in future adapted for a stacking analysis with all the GRBs detected by the ANTARES detector. In fact the background estimation method developed in this thesis do not require dedicated simulations of the unfiltered data

sample of each burst, but it relies only on the official Run by Run Monte Carlo of filtered data provided by the collaboration.

The future KM3NeT-ARCA telescope will be the ideal instrument to constrain the neutrino flux from GRBs. It will be a kilometre scale detector composed by a two building blocks of 115 detection strings each. The KM3NeT collaboration has already decided to register unfiltered data in correspondence of gamma ray bursts in order to perform an adapted version of this analysis with the future telescope. KM3NeT is expected to improve the ANTARES limits by approximately one order of magnitude, so it will set much better constraints on the neutrino flux in correspondence of gamma ray bursts.

The detection of neutrino from gamma ray bursts will provide important informations of the process of emission of GRB, in particular it will give strong indications of the hadronic interactions occurring in the jets of the gamma ray bursts and it will help to distinguish between the different GRB model scenarios.

Acknowledgments

First I want to express my sincere thanks to my supervisors Marco Anghinolfi and Antoine Kouchner for the unconditional support to my work and for the fruitful discussions we had during these years. Their advices on every field of the “research life” have been really important for me.

Many members of the ANTARES collaboration contributed to the success of this thesis, I am grateful in particular to Bruny Baret, Damien Dornic, Dorothea Samtleben, Silvia Celli and Damien Turpin for the support on the GRBs analysis and Jürgen Brunner, Tommaso Chiarusi, Heide Costantini, Carla Distefano, Aart Heijboer, Piera Sapienza and Maurizio Spurio for the interest in the Moon shadow analysis. An important thanks to Mieke Bouwhuis, Julia Schmid and Erwin Visser, their work has been an important base for this thesis. I reserve a special thanks to Christophe Hugon for his help when I faced new challenges during my PhD, he contribute to improve my skills in many different fields of the research.

I really appreciated the comments and the advises of my rapporteur Corinne Augier, they have been really important to improve the clearness of the thesis manuscript.

During my PhD I had a chance to work in different labs. I would like to thanks the Lab 102 group at Genova, the APC group at Paris and the CPPM group at Marseille. I have good memories of the time spent in these groups and they really contribute to my formation.

My PhD was done in co-doctorate with APC thanks to IDAPP. I would like to thank the IDAPP members, in particular Alessandra Tonazzo and Isabella Masina.

Finally I would like to thank my parents and Valentina for always being there, supporting my choices.

Bibliography

- [1] Cowan C.L. Jr. et al., *Detection of the Free Neutrino: a Confirmation*. Science 124 (3212), 103–104 (1956).
- [2] Bosetti P. C., *DUMAND status report*. Nucl. Phys. Proc. Suppl. 48, 466-468 (1996)
- [3] Barwick S. et al., *AMANDA: South pole neutrino detector*. AIP Conf. Proc. 272, 1250-1253 (1993)
- [4] Resconi E. et al., *High Energy Neutrino Astronomy: IceCube 22 and 40 strings*. Nucl.Phys.Proc.Suppl. 229-232, 267-273 (2012)
- [5] Klebesadel R. W. et al., *Observations of Gamma-Ray Bursts of Cosmic Origin*. Ap.J.Lett.182, L85 (1973).
- [6] Mazets E.P. et al., *Flare of cosmic gamma radiation as observed with satellite*. JETP Lett. 19, 77 (1974).
- [7] Meegan C. A. et al. , *Spatial distribution of gamma-ray bursts observed by BATSE* . Nature 355, 143 (1992).
- [8] Hurley K. et al. , *Detection of a gamma-ray burst of very long duration and very high-energy*. Nature 372, 652 (1994).
- [9] Kouveliotou C. et al. , *Identification of two classes of gamma-ray bursts*. Astrophys. J., Lett., 413, L101 (1993).
- [10] Fishman G., Meegan, C. , *Gamma-Ray Bursts*. Annu. Rev. Astron. Ap. 33, 415 (1995).
- [11] Costa et al., *Discovery of an X-ray afterglow associated with the gamma-ray burst of 28 February 1997* . Nature 387:783 (1997).
- [12] Kulkarni et al., *The afterglows of gamma-ray bursts*. Gamma Ray Bursts, AIP Conf.Proc 526 (1999).

- [13] Nomoto K. et al., *Hypernovae and other black hole forming supernovae*. astro-ph/0308136 (2003).
- [14] Paczynski B., *Super-Eddington winds from neutron stars*. Ap.J.363:218 (1990).
- [15] Hardling A.K., M. G. Baring, *Escape of High-Energy Photons from Relativistically Expanding Gamma-Ray Burst Sources*. Gamma-ray Bursts, AIP Conf Proc 307, ed. G. Fishman, et al. , (AIP:NY) p.520 (1994).
- [16] Olive K. A. et al., *Review of Particle Physics* Chin. Phys. C38 p.508 (2014).
- [17] Shemi A., Piran T., *The appearance of cosmic fireballs* . Ap.J.Lett.365:L55 (1990).
- [18] Paczynski B., *Gamma-ray bursters at cosmological distances* . ApJ, 308:L43 (1986).
- [19] Rees M.J., Mészáros P., *Relativistic fireballs-energy conversion and time-scales* . M.N.R.A.S.258:P41 (1992).
- [20] Rees M.J., Mészáros P., *Unsteady outflow models for cosmological gamma-ray bursts* . Ap.J.Lett.430:L93 (1994).
- [21] Sari R. and Piran, T. *Variability in GRBs: A Clue* . ApJ 485:270 (1997).
- [22] Rees M.J., Mészáros P., *Optical and Long-Wavelength Afterglow from Gamma-Ray Bursts*. Ap.J.476:232 (1997).
- [23] Mészáros P., Rees M.J., *GeV Emission from Collisional Magnetized Gamma Ray Bursts*. Astrophys.J.Lett. 733, L40+ (2011).
- [24] Thompson C., *A Model of gamma-ray bursts*. M.N.R.A.S 270, 480 (1994).
- [25] Band D. et al., *BATSE observations of gamma-ray burst spectra. 1. Spectral diversity*. Astrophys.J. 413, 281 (1993).
- [26] Gao S. et al., *High Energy Neutrinos from Dissipative Photospheric Models of Gamma Ray Bursts* . JCAP 1211 058 (2012).
- [27] Zhang B., Kumar P., *Model-dependent high-energy neutrino flux from Gamma-Ray Bursts*. Phys. Rev. Lett. 110, 121101 (2013).
- [28] Lazzati D. et al., *Photospheric emission as the dominant radiation mechanism in long-duration gamma-ray bursts*. Astrophys.J. 765, 103 (2013).
- [29] Ageron M. et al., *Performance of the first antares detector line*. Astropart. Phys. 31 277-283 (2009).

- [30] Markov M.A., *On high energy neutrino physics* Proceedings Int. Conf. on High Energy Physics, Univ. of Rochester, 183 (1960).
- [31] Adrian-Martinez S. et al., *Search for Cosmic Neutrino Point Sources with Four Year Data of the ANTARES Telescope*. *Astrophys. J.* 760, 53 (2012)
- [32] Capone A. et al., *Measurements of light transmission in deep sea with the AC9 trasmisometer*. *NIM A* 487(3), 423–434, ISSN 01689002 (2002).
- [33] Schuster W. H., *Measurement of the optical properties of the deep Mediterranean - the ANTARES detector medium*. PhD thesis (2002).
- [34] Jonasz M. and Fournier G. R., *Light scattering by particles in water: theoretical and experimental foundations*. Isevier academic press: ISBN-13:978-0-12-388751-1, ISBN-10: 0-12-388751-8 (2007).
- [35] Smoluchowski M., *Molekular-kinetische Theorie der Opaleszenz von Gasen im kritischen Zustande, sowie einiger verwandter Erscheinungen*. *Ann. d. Phys.* 330(2), 205–226 (1908).
- [36] Mobley C., *Light and Water: Radiative Transfer in Natural Waters* Academic Press, cd edition ed. (1994).
- [37] Kopelevich O., *Small-parameter model of optical properties of sea water* *Ocean Optics* 19 (1983).
- [38] Petzold T., *Volume Scattering Functions for Selected Ocean Waters* Scripps Inst. Oceanogr. , SIO Ref. 72–78 (1972).
- [39] Smith R. C. and Baker K. S., *Optical properties of the clearest natural waters (200-800 nm)*. *APPLIED OPTICS*, Vol. 20, No. 2 (1981).
- [40] Khanaev S. and Kuleshov A., *Measurements of water transparency South- West of Greece*. in L. Resvanis, ed., *Proceedings of the Second NESTOR International Workshop*, 253–269, University of Athens, Greece (1992).
- [41] Aguilar J. et al., *Transmission of light in deep sea water at the site of the Antares neutrino telescope*. *PLoS ONE* 8(7): e67523 (2013).
- [42] Tamburini C. et al., *Deep-Sea Bioluminescence Blooms after Dense Water Formation at the Ocean Surface*. *Astropart. Phys* 23(2005b)(1), 131–155, ISSN 09276505 (2005).

- [43] Brunner J. et al., *A Fast Algorithm for Muon Track Reconstruction and its Application to the ANTARES Neutrino Telescope*. *Astropart.Phys.*34:652-662 (2011)
- [44] Bazzotti M., *Studies of the atmospheric muon flux with the ANTARES detector*. PhD thesis Bologna U. (2009).
- [45] Aguilar J.A. et al., *Performance of the front-end electronics of the ANTARES neutrino telescope*. *Nucl. Instrum. and Methods. A* 622, 59-73 (2010)
- [46] Aguilar J.A. et al., *The data acquisition system for the ANTARES neutrino telescope*. *Nuclear Instr. and Methods in Phys. Res. A* 570, 107-116 (2007)
- [47] Bailey D., *Genhen v5r1 : Software Documentation* . ANTARES internal note, ANTARES-SOFT-2002-004 (2002).
- [48] Ingelman G. et al, *LEPTO 6.5 — A Monte Carlo generator for deep inelastic lepton-nucleon scattering*. *Computer Phy. Communications* 101, 108-134 (1997).
- [49] Barr G. D. , *The separation of signals and background in a nucleon decay experiment* . PhD thesis, University of Oxford (1987).
- [50] Heck D. et al , *CORSIKA: a Monte Carlo code to simulate extensive air showers* TIB Hannover (1998).
- [51] Antonioli P. et al, *A three-dimensional code for muon propagation through the rock: MUSIC*. *Astropart. Phys.*, 7, 357368 (1997).
- [52] Carminati G. et al, *Atmospheric MUons from PArametric formulas: a fast GEnerator for neutrino telescopes (MUPAGE)*. *Comput. Phys. Commun.*, 179: 915923 (2008).
- [53] de Jong M. , *The TriggerEfficiency program*. ANTARES internal note, ANTARES-SOFT-2009-001 (2009).
- [54] Heijboer A., *Track reconstruction and point source searches with ANTARES*. PhD thesis Amsterdam U. (2004).
- [55] Visser E., *Neutrinos from the Milky Way*. Doctoral Thesis, Leiden University, (2015).
- [56] Hill C. and Rawlins K., *Unbiased cut selection for optimal upper limits in neutrino detectors: The Model rejection potential technique*. *Astropart. Phys.* 19, 393-402 (2003).
- [57] Adrian-Martinez S. et al., *Search for muon neutrinos from gamma-ray bursts with the ANTARES neutrino telescope using 2008 to 2011 data*. *A&A*, Volume 559, A9 (2013).

- [58] Zaborov D., *The k-40 calibration method*. ANTARES internal notes, ANTARES-CALI/2011-001 (2011).
- [59] Zaborov D., *Coincidence analysis in ANTARES: Potassium-40 and muons*. Physics of Atomic Nuclei, Volume 72, Issue 9, pp 1537-1542 (2009).
- [60] Geyer K., *CMeasurements of the atmospheric muon rate with the ANTARES neutrino telescope*. PhD Thesis, U. Erlangen-Nuremberg.
- [61] Ardid M., *Positioning system of the ANTARES neutrino telescope*. Nuclear Instruments and Methods in Physics Research Section A: Accelerators, Spectrometers, Detectors and Associated Equipment, Vol. 602, No. 1, pp. 174 (2009).
- [62] Brown A. M., *Positioning system of the ANTARES Neutrino Telescope*. Proceedings of 31st ICRC conference (2009).
- [63] Sanguineti M., *Moon shadow observation with the ANTARES neutrino telescope*. Proceedings of 34th ICRC conference (2015).
- [64] Alexandreas D. E. et al., *Observation of shadowing of ultrahigh-energy cosmic rays by the Moon and the Sun*. Phys. Rev., D43:1735-1738 (1991).
- [65] Amenomori M. et al., *Cosmic-ray deficit from the directions of the Moon and the Sun detected with the Tibet air-shower array*. Phys. Rev., D47:2675-2681 (1993).
- [66] Borione A. et al. , *Observation of the shadows of the Moon and Sun using 100 TeV cosmic rays*. Phys. Rev., D49:1171-1177 (1994).
- [67] Ambrosio M. et al., *Observation of the shadowing of cosmic rays by the Moon using a deep underground detector*. Phys. Rev., D59:012003 (1999).
- [68] Cobbs H. et al. , *Observation of a shadow of the Moon in the underground muon flux in the Soudan 2 detector*. Phys. Rev., D61:092002 (2000).
- [69] ARGO-YBJ Collaboration, *Observation of the Cosmic Ray Moon shadowing effect with ARGO-YBJ*. Phys. Rev., D.84:022003 (2011).
- [70] ICECUBE collaboration, *Observation of the cosmic-ray shadow of the Moon with Ice-Cube*. Phys. Rev. D 89, 102004 (2014).
- [71] Distefano C., *On the detection of the Moon shadow with the ANTARES neutrino telescope*. Nuclear Instruments and Methods in Physics Research A 626-627 S223-S225 (2011).

- [72] Margiotta A. for the ANTARES collaboration, *Common simulation tools for large volume neutrino detectors*. Nucl.Instrum.Meth., A725, 98-101 (2013).
- [73] ANTARES collaboration, *Search for a diffuse flux of high-energy ν_μ with the ANTARES neutrino telescope*. Phys.Lett. B696 16-22 (2010).
- [74] Heck D. et al., *Observation of a shadow of the Moon in the underground muon flux in the Soudan 2 detector*. Phys. Rev. D 61 (2000).
- [75] Ackermann M., *Fermi-LAT Observations of the Gamma-Ray Burst GRB 130427A*. Science, Vol. 343 no. 6166 pp. 42-47, (2014)
- [76] Melandri A., *Diversity of gamma-ray burst energetics vs. supernova homogeneity: SN 2013cq associated with GRB 130427A*. Astron. Astrophys. 567 A29, (2014).
- [77] Maselli A., *GRB Coordinates Network*. GCNCircular Service, 14448, 1 (2013).
- [78] Hummer S., Baerwald P., Winter W., *Neutrino Emission from Gamma-Ray Burst Fireballs, Revised*. Phys. Rev. Lett., 108, 231101 (2012).
- [79] de Jong M., *The ANTARES trigger software*. ANTARES internal note, ANTARES-SOFT-2005-005 (2005).
- [80] Barlow R., *Extended maximum likelihood*. Nucl. Instr. Meth. A 297, 496, (1990).
- [81] Guetta D. et al., *Neutrinos from individual gamma-ray bursts in the BATSE catalog*. Astropart.Phys. 20, 429-455 (2004).